

**REGULAR AND CHAOTIC MOTION OF
UNIFORM ELLIPTICAL VORTICES
IN EXTERNAL LINEAR
TIME DEPENDENT VELOCITY FIELDS**

Thesis by
Kayo Ide

In Partial Fulfillment of the Requirements
for the Degree of
Doctor of Philosophy

California Institute of Technology
Pasadena, California

1990

(Submitted September 29, 1989)

ACKNOWLEDGEMENTS

My study at CALTECH could not have been completed without support and understanding from all the people I have been fortunate enough to develop friendships with.

I would like to thank my adviser, Professor Stephen R. Wiggins, for his thoughtful guidance throughout my study since spring, 1987. Needless to say his advice in mathematics and physics, his understanding and encouragement have kept me going at CALTECH.

I would also like to thank my thesis and candidacy committees for their support, understanding and patience, in addition to advice and suggestions: Professor Anthony Leonard, Professor Donald Coles, Professor Hans G. Hornung, Professor Danniell Meiron, Professor Anatol Roshko and Dr. James E. Broadwell. I am grateful to Professor James K. Knowles for his help in making the dissertation process smooth. I would like to thank Professor Paul Dimotakis for his advice, support and understanding as my adviser for first two years of my Ph.D. program and as a faculty member at the GALCIT thereafter. A heartfelt thanks is offered to all staff members in GALCIT and Thomas building. I owe special thanks to Jacquelyn Beard and Karen Cheetham for their warm support. I am grateful to my friends in the GALCIT, 'Supper club' and SOPS: Ruth Erlanson, Tom Fric, Rick Gilbrich, Sy Shimabukuro, Regina Dugan, Albert Moser, Kris and Laurie Wood and Andrew Lewis.

Finally, I would like to express my sincere appreciation to Professor Hans Wolfgang Liepmann. I have been always impressed by his deep understanding of matters ever since I came to know him. It was because of his understanding and support that I could get through difficult times.

Abstract

The motion of a uniform vorticity of an elliptical shape (UEV) induced by an external linear flow field and a self induced effect in a two dimensional incompressible inviscid flow is investigated. The fluid particle motion around the UEV is also investigated. The techniques from dynamical systems are intensively used. In particular, we develop some modified versions of the Melnikov techniques which show how the perturbations influence the dynamics and allow us to predict the perturbed dynamics by knowing the unperturbed dynamics.

The UEV motions in steady external linear flow fields are regular, however there are quite a few possibilities for types of motion depending on the UEV initial configuration and the external linear flow field parameters. When time periodic perturbation is imposed, the UEV motion drastically changes and various new types of motion become possible. This includes transition dynamics (i.e., the UEV changes its type of motion), chaotic motion, irregular oscillation and rotation, and quasiperiodic motion. The Melnikov techniques tell that the excess kinetic energy play significant roles in determining the UEV dynamics.

A periodic motion of the UEV in a steady external linear flow field results in the generation of chaotic fluid particle mixing regions around the UEV where the fluid particles from distinct flow regions are chaotically transported. Our study emphasizes on the finite core size effect of the UEV in comparison to flow fields induced by a point vortex in unsteady external linear flow fields. We show that the size of the UEV core and the UEV initial configuration are important factors in determining the size of the mixing region.

TABLE OF CONTENTS

	Page
Acknowledgements	iii
Abstract	iv
Table of contents	v
List of figures	viii
List of tables	xii
Chapter 1 Introduction	
1.1 Motivation	1
1.2 Historical background	2
1.3 Simple examples	3
1.4 Fluid particle motion	6
1.5 Organization of thesis	7
Chapter 2 Equations of motion for UEV	
2.1 Coordinates systems of UEV and its self-induced velocity field	8
2.2 External linear velocity field	11
2.3 Conserved quantities	12
2.4 O.D.E.'s for UEV motion	15
2.5 Change of variables	17
2.6 Figures for Chapter 2	21
Chapter 3 UEV dynamics in steady external linear velocity field	
3.1 Dynamics and bifurcation of Eqn. (2.10)	25
3.2 UEV motion	30
3.3 Decomposition of kinetic energy	33
3.4 Figures for Chapter 3	39

Chapter 4 UEV dynamics in unsteady external linear velocity field

4.1	The Poincaré map technique	56
4.2	Some typical orbits of the perturbed system in the Poincaré map ...	58
4.2.1	Homoclinic tangle	59
4.2.2	Breaking-up of the invariant circles in the unperturbed system	65
4.2.2.1	Resonance band of order $\frac{m}{n}$	65
4.2.2.2	KAM torus and cantorus	69
4.2.2.3	The global structure	70
4.2.2.4	Transition dynamics through RB $\frac{m}{1}$	73
4.3	Summary for qualitative UEV motion in time periodic external linear flow field	74
4.4	The Melnikov technique and its physical implication	74
4.4.1	Three types of perturbation and excess kinetic energy	74
4.4.2	Perturbation in $\sigma(\tau)$	77
4.4.3	Perturbation in $\kappa(\tau)$	79
4.4.4	Perturbation in $\alpha(\tau)$	82
4.4.5	Relation among perturbations in $\sigma(\tau)$, $\alpha(\tau)$ and $\kappa(\tau)$	84
4.4.6	Perturbation in all parameters	86
4.5	Figures for Chapter 4	90

Chapter 5 Fluid particle motion in the induced flow fields

5.1	The equation of motion governing the flow field	108
5.2	Steady flow field	111
5.3	Unsteady flow field	112
5.3.1	Qualitative flow dynamics	113
5.3.2	The Melnikov technique on heteroclinic orbits	114
5.4	Figures for Chapter 5	121

Appendix	124
A1 Velocity fields induced by elliptical vortices.....	124
A1.1 Definition of a EV and induced velocity field around its centroid.....	124
A1.2 Local straining effect in an irrotational flow.....	126
A1.3 Application to a UEV and GEV.....	127
A1.4 Figures for Appendix 1.....	129
A2 Bifurcations.....	131
A2.1 Bifurcations on $\varphi = \frac{\pi}{2}$	131
A2.2 Bifurcations on $\varphi = \frac{3\pi}{2}$	132
A2.3 Bifurcations to periodic motion as $I \rightarrow \infty$	133
A2.4 Global bifurcation.....	133
A2.5 Bifurcations on $\sigma_0 = 0$	137
A2.6 Bifurcation curves.....	135
A2.7 Figures for Appendix 2.....	136
A3 The Melnikov functions with symmetry.....	134
A4 Perturbation frequency range for transition between oscillation and rotation.....	142
A5 Proof for Remark 3, 4 and 5 for case 2.....	145
A6 The Melnikov functions with Hamiltonian perturbations.....	147
A7 The modified Melnikov function.....	150
A7.1 Equations of motion.....	150
A7.2 Modified Melnikov function $M_\epsilon(\tau_0)$ on homoclinic orbit.....	151
A7.3 Modified Melnikov function $M_\epsilon^{\frac{m}{n}}(\tau_0)$ on resonance band of order $\frac{m}{n}$	152
References	154

LIST OF FIGURES

Chapter 2

Figure 2.1 Lagrangean coordinate system and the UEV coordinate system

Figure 2.2 UEV configuration and vorticity distribution

Figure 2.3 Stream lines induced by the UEV

Figure 2.4 Stream lines induced by external linear flow fields
(a) external straining field (b) external rotational field.

Figure 2.5 Relation between I and η

Figure 2.6 Relation between $\delta - \zeta$ phase space and $(\sqrt{2I}, \varphi)$ coordinate

Chapter 3

Figure 3.1 A hyperbolic fixed point q_h , a stable manifold $W^s(q_h)$ and a unstable manifold $W^u(q_h)$

Figure 3.2 An elliptic fixed point q_e

Figure 3.3 One parameter family periodic orbits around an elliptic fixed point q_e

Figure 3.4 A homoclinic orbit and associated one parameter family of periodic orbits

Figure 3.5 Bifurcation diagram in κ_0, σ_0 space

Figure 3.6 Saddle-node bifurcation across S^+ above I_2^+

Figure 3.7 Global bifurcation across G^+

Figure 3.8 Bifurcation at the origin regarding q_e^+ across U^+

Figure 3.9 Bifurcation at $I = \infty$ on $\varphi = 3\pi/2$ across I_2^+ below S^+

Figure 3.10 Saddle-node bifurcation on S^+ below I_2^+

Figure 3.11 Bifurcation at the origin regarding q_e^+ across U^-

Figure 3.12 Ring bifurcation across R

Figure 3.13 Possible UEV motion

Figure 3.14 UEV periodic motion
(a) counterclockwise motion (b) clockwise motion

Figure 3.15 Unbounded orbits

Figure 3.16 Irreversible elongation

Figure 3.17 Possible UEV motion

Figure 3.18 Level curves of excess kinetic energies
(a) H_E (b) H_S (c) H_R

Figure 3.19 Geometrical relation between I_0 and orbits

Figure 3.20 Excess kinetic energies on some typical unperturbed orbits
(a) (c-c) oscillation (b) (c-c) rotation
(c) inner homoclinic orbit (d) (c) oscillation

Chapter 4

Figure 4.1 Geometrical structure of a homoclinic tangle

Figure 4.2 Primary intersection point

Figure 4.3 Ordering of the lobes

Figure 4.4 Horseshoe map

Figure 4.5 Two homoclinic tangles

Figure 4.6 Resonance band of order $\frac{m}{n}$ for $m = 3, n = 1$ and $\ell = 1$

- Figure 4.7** Bifurcation on resonance band of order $\frac{m}{n}$ for $m = 3, n = 1$ and $\ell = 1$
- Figure 4.8** Bifurcation of a resonance band on nontwisting band for $m = 3, n = 1$ and $\ell = 1$
- Figure 4.9** Geometrical symmetry in the unperturbed phase space
(a) symmetry around ζ -axis
(b) symmetry around δ -axis and ζ -axis
- Figure 4.10** One parameter family of periodic orbits bounded by a homoclinic orbit and its geometrical relation to the resonance band of order $\frac{m}{n}$
- Figure 4.11** Global resulting structure for one parameter family of periodic orbits bounded by a homoclinic orbit
- Figure 4.12** One parameter family of periodic orbits not bounded by a homoclinic orbit and its geometrical relation to the resonance band of order $\frac{m}{n}$
- Figure 4.13** Global resulting structure for one parameter family of periodic orbits not bounded by a homoclinic orbit
- Figure 4.14** Graph of $F(\sigma_0, \kappa_0; \Omega)$ with respect to Ω
- Figure 4.15** Width of RB $\frac{m}{1}$ and its position

Chapter 5

- Figure 5.1** Stream line structures for a steady PV system
(a) $\beta_0 > 1/2$ (b) $|\beta_0| < 1/2$
(c) $\beta_0 < -1/2$
- Figure 5.2** Heteroclinic tangles
(a) $|\beta_0| < 1/2$ (b) $\beta_0 < -1/2$
- Figure 5.3** Graphs of F_γ and F_β with respect to Ω for unsteady PV systems

Figure 5.4 Graphs of area of a lobe corresponding to Fig. 5.3

Figure 5.5 Graphs of area of a lobe for unsteady UEV system in comparison to unsteady PV systems

Appendix 1

Figure A1.1 Vorticity distribution of a EV

Figure A1.2 Coordinate system for a EV

Appendix 2

Figure A2.1 Graph of $I = K_+^{-1}(I; \sigma_0)$

Figure A2.2 Graph of $I = K_-^{-1}(I; \sigma_0)$

LIST OF TABLES

Chapter 3

Table 3.1 Regular UEV motions and corresponding orbits

Chapter 4

Table 4.1 Possible UEV motion in unsteady external linear flow field

Chapter 1

INTRODUCTION

1.1 Motivation

In two dimensional incompressible inviscid flow, the vortex distribution completely determines the flow field as described by the Biot-Savort law (Bachelor [1968], Saffman and Baker[1979]). Hence, understanding the vortex dynamics (or equivalently vortex interaction process) is one way of understanding the flow dynamics. There are many flows which can be modeled by single or multiple number of discrete vortices (Roshko [1976], Jimenez [1987], McWilliams [1984], Moore and Saffman[1975], Saffman and Schatzman[1982]). If the discrete vortices are close together, merger may take place. (Melender et.al. [1985][1987a][1987b][1988]). If a discrete vortex is far from other vortices, it is useful to study the vortex's dynamics (i.e., how it deforms around its centroid through the influences of itself and the other vortices).

In a Lagrangian frame which is translated with and rotated around a vortex blob centroid, the vortex blob configuration is changed by the influence of self-induced velocity field and the external flow field, i.e., the local fluid particle velocity relative to the centroid. The first order approximation to the external flow field is a linear flow field around the centroid which is composed of straining and rotational effects. The straining flow field is described by two variables (γ, α) where γ is the strength of the straining effect and α is the inclination axis of the straining axis in the Lagrangian coordinate frame. The straining flow field, which is irrotational, is caused by vortex interaction with other vortices and boundaries. The rotational flow, or background vorticity effect, is described by a variable ω_R . It is strictly due to the rotation of the Lagrangian frame around the centroid, because of assumptions

on the discrete vortex. In this research, we are concerned with vortex motion in an arbitrary external linear flow field. We use an elliptical region of uniform vorticity distribution (uniform elliptical vortex, UEV henceforth) as a model vortex. The UEV, as a model, has a significant advantage for the analysis, i.e., the UEV changes its configuration in time in steady or unsteady external linear flow fields, while the elliptical shape of the vortex is preserved. This is because the total velocity field around the UEV centroid is linear. Note that the two variables (η, θ) , where $\eta = a/b$ is an aspect ratio of the ellipse with a and b as the semi-major and semi-minor axes, and θ is an inclination angle of semi-major axis of the ellipse from the Lagrangian frame, can completely describe the vortex configuration because the area and the circulation of the vortex are invariant in the flow field. Furthermore, the dynamics of the UEV are given by solving two dimensional O.D.E.'s for (η, θ) .

When some perturbation is imposed on the boundary shape of the vortex, non-linear effect may become important factor for the vortex's dynamics (Constantin and Titi [1988], Dritschel [1988a],[1988b], Moore and Saffman [1975], Wan and Pulvirenti[1985]). This thesis does not include either instability analysis (i.e., how the perturbation on the vortex boundary may or may not develop, Szeto and Saffman [1980], Kamm [1987]) or vortex dynamics in external nonlinear flow fields. However, the modified moment model, which is a generalized version of Melander et.al. [1986], seems to give some insights to those problems.

1.2 Historical background

The dynamics of a UEV in no external flow field were first formulated by Kirchoff [1877]. A UEV of any aspect ratio rotates around its centroid with a constant angular velocity while preserving its aspect ratio (see also Lamb [1945]). Moore and Saffman [1971] showed that in a steady, pure straining field or in a steady simple shear flow, there exist steady UEV configurations. For a UEV in a steady, pure straining field, the steady UEV configuration exists with its semi-major axis aligned $\frac{\pi}{4}$ to the straining axis as long as the straining and the UEV vorticity rate $\frac{\gamma}{\omega_E}$ is less than 0.15. For a UEV in a steady simple shear flow, the steady UEV

configuration exists as long as the shear and the UEV vorticity rate $\frac{\gamma'}{\omega_E}$ is less than 0.21.

The equations of the UEV motion in steady external linear flow fields were first obtained by Kida [1981] as two dimensional O.D.E.'s for (η, θ) as exact solutions of the Euler equations corresponding to uniform vorticity regions of elliptical shape. The bifurcation diagram in $(\frac{\omega_R}{\omega_E}, \frac{\gamma}{\omega_E})$ was given so as to show all possible UEV motions caused by variation of two steady external linear flow parameters. Note that $(\frac{\omega_R}{\omega_E}, \frac{\gamma}{\omega_E})$ describe the steady external linear flow field when the Lagrangian frame is chosen axis to be aligned with the straining axis. Neu [1984] showed a systematic way of deriving the O.D.E.'s for the UEV motion in a steady pure straining field (i.e., no background vorticity effect). Neu also reformulated the equations of the UEV motion as a Hamiltonian system and presented the solution in $X - Y$ phase space with polar coordinates (η, θ) . However, the transformation to the Hamiltonian system that Neu adopted involves scaling of the time variable by $\frac{\eta^2 - 1}{\eta}$, which means that the solutions given in the Hamiltonian system do not correspond to the UEV motion in a time-wise sense. This becomes a significant obstacle when we consider the UEV motion in time dependent external linear flow fields.

In this thesis, we first show that the equations of the UEV motion hold in any time dependent external linear flow field described by three variables $(\gamma(t), \alpha(t), \omega_R(t))$. It can also be shown that the elliptical shape of the vortex can not be preserved in higher order external velocity field, i.e., the equations of the UEV motion are based on an assumption that the total induced velocity inside the UEV is linear. In order to facilitate techniques from dynamical systems, we transform the equations of the UEV motion to two sets of the Hamiltonian systems (see Melander et al. [1987]). We show that these Hamiltonian systems, together with the new canonical variables of the equations, display the physical background of the UEV motion. We recover the bifurcation diagram given by Kida, and show all possible solutions in steady external linear flow field as the level sets of the Hamiltonian function in the phase space of the corresponding canonical variables.

In Chapter 4, we seek all possible motions of the UEV in a unsteady external linear flow field, see how the external flow parameters influence the unsteady UEV dynamics, and try to understand the mechanisms of the UEV dynamics. We use techniques from dynamical systems theory and add modifications which give some physical interpretations of the perturbation effects.

1.3 Simple examples

In the vortex interaction process, it is clear that the influences of other vortices are time dependent. We now show three simple examples which demonstrate time dependence on straining effects and background vorticity effects through vortex interaction and boundary conditions on the UEV.

1) A pair of co-rotating equal UEV's

Consider a pair of co-rotating equal UEV's whose centroids' positions are denoted by $z = \pm Re^{i\chi}$. We assume that the distance $2R$ between two vortices are much larger than the vortex core radius $\sqrt{a^2\pi/\eta} = \text{constant}$ (i.e., $R/\sqrt{a^2\pi/\eta} \gg 1$) so that the leading order term in the local external flow field on the UEV induced by another UEV is linear term (i.e., the straining effect). The Lagrangian frame is translated with and rotated around the centroid so that the straining axis and the Lagrangian frame axis are aligned. The rotation of the Lagrangian frame results in the back ground vorticity effect ω_R . The straining effect (γ, α) and background vorticity effect ω_R which each UEV receives from another UEV are as follows:

$$\begin{aligned}\gamma &= \frac{\Gamma}{8\pi R^3} + \text{higher order terms in } \frac{1}{R} \\ \alpha &= 0 \\ \omega_R &= \frac{\Gamma}{4\pi R^3} + \text{higher order terms in } \frac{1}{R},\end{aligned}$$

with

$$\begin{aligned}\frac{dR^2}{dt} &= \left(\frac{\Gamma}{32\pi}\right) \left(\frac{a^2\pi}{\eta R^2}\right) \left(\frac{\eta^2 - 1}{\eta}\right) \sin 2(\theta - \chi) \\ &\quad + \text{higher order terms in } \left(\frac{a^2\pi}{\eta R^2}\right).\end{aligned}$$

Time dependence on the external linear flow field is due to the change in the distance $2R$ between two vortices.

2) A pair of translating UEV's of opposite sign

Consider a pair of translating UEV's of opposite sign which float in a uniform flow field. The distance between centroids is R , and we again assume that the distance $2R$ between two vortices are much larger than the vortex core radius $\sqrt{a^2\pi/\eta} = \text{constant}$ (i.e., $R/\sqrt{a^2\pi/\eta} \gg 1$) so that the leading order term in the local external flow field on the UEV induced by another UEV is linear term (i.e., the straining effect). The Lagrangian frame is translated with the centroid. The straining effect (γ, α) that each UEV receives from another UEV is as follows:

$$\begin{aligned} \gamma &= \frac{\Gamma}{8\pi R^3} + \text{higher order terms in } \frac{1}{R} \\ \alpha &= 0, \end{aligned}$$

with

$$\begin{aligned} \frac{dR^2}{dt} &= \left(\frac{\Gamma}{32\pi} \right) \left(\frac{a^2\pi}{\eta R^2} \right) \left(\frac{\eta^2 - 1}{\eta} \right) \sin 2\theta \\ &+ \text{higher order terms in } \left(\frac{a^2\pi}{\eta R^2} \right). \end{aligned}$$

Time dependence on the external linear flow field is due to the change in the distance $2R$ between two vortices.

3) A UEV floating with a uniform flow (U) over a wavy wall.

In this case, it can be shown by solving the resulting stream line structure in the flow field that the UEV receives a time periodic straining effect from the wall up to the leading order. (Liepmann and Roshko [1956]). The wall must be far enough from the vortex as compared to the vortex mean core size

$$\begin{aligned} \gamma &= \frac{\Gamma}{4\pi R_0^3} (1 + \epsilon_\gamma \gamma_1(t)) + \text{higher order terms in } \frac{1}{R} \\ \alpha &= -\frac{\pi}{4} (1 + \epsilon_\alpha \alpha_1(t)) + \text{higher order terms in } \frac{1}{R}. \end{aligned}$$

where R is the distance between the wall and the UEV, R_0 is the mean distance between the wall and the UEV, moreover, ϵ_γ , ϵ_α , $\gamma_1(t)$ and $\alpha_1(t)$ are defined by

the wavy wall configuration, and $\gamma_1(t)$ and $\alpha_1(t)$ are periodic functions. Time dependence on the external flow field is due to the wall configuration.

1.4 Fluid particle motion

In two dimensional incompressible flow, the velocity field for the fluid particle motion can be formulated as a Hamiltonian system with the stream function acting as the Hamiltonian function. This gives a significant understanding of the flow dynamics.

Consider a flow field induced by a point vortex in a steady external flow field. It is clear that the total induced flow field is steady and hence, all fluid particle motion whose paths are described by the stream lines are regular. However, if the point vortex is replaced by a finite core size vortex blob, then the blob may be deformed around its centroid by the external flow field and by a self-induced effect. This results in a unsteady flow field around the vortex blob. In order to examine the finite core effect of the vortex on the flow dynamics, we study the fluid particle motion around a UEV in a steady external linear flow field. This is a simple, leading order approximation to the flow dynamics. Moreover, the UEV dynamics are completely understood from the analysis in Chapter 3, which is a significant advantage in the analysis from a technical point of view.

When a UEV is at its steady configuration, the total induced flow field is steady, and the flow dynamics can be described by the stream line structure. When a UEV undergoes periodic motion, the total induced flow field is unsteady (time periodic), and the stream line structure may break up resulting in new types of motion which can not occur in the steady flow field. The techniques from dynamical systems theory are again used to study the flow dynamics. In particular, the breaking-up of the dividing stream lines results in a chaotic transport region whose mechanism is well formulated by lobe dynamics (see Rom-Kedar, Leonard and Wiggins [1988]). We examine the flow dynamics induced by the UEV as compared to the flow dynamics due to the point vortex in steady and unsteady external linear flow fields by introducing modified Melnikov functions additionally.

1.5 Organization of the thesis

This thesis is organized as follows. In Chapter 2, we derive the equations of motion for the UEV and discuss their physical implications. In Chapter 3, we describe the various UEV motion in steady linear external flow field. In Chapter 4, we describe how the UEV motion changes under time periodic perturbation in the external linear flow field. And, in chapter 5, we examine how a finite core size vortex influences fluid particle motion.

Chapter 2

EQUATIONS OF MOTION OF A UEV

In two-dimensional incompressible inviscid flow, each vortex element moves with the local fluid velocity induced by either vortex interactions or boundary conditions. When the flow field is represented by discrete vortex blobs and some boundary conditions, the flow dynamics can be decomposed into the centroid motion of the vortex blobs and the deformation of the vortex blobs around their centroids.

In a Lagrangian frame which is translated with and rotates around a vortex blob centroid, the vortex blob changes its configuration due to the self-induced velocity field and the external flow field, i.e., the local fluid velocity field relative to the centroid. The first order approximation to the external flow field is a linear flow field around the centroid which is composed of a straining effect and a rotational effect. The straining flow field is irrotational and caused by the vortex interaction with other vortices and boundary conditions, while the rotational flow field, or equivalently the background vorticity flow field, is strictly due to the rotation of the Lagrangian frame around the centroid. In this thesis, we are concerned with vortex dynamics in an arbitrary external linear flow field using a uniform elliptical vortex (UEV) as a model. We will also briefly discuss fluid particle motion around the vortex in terms of finite core size effects of the vortex.

2.1 Coordinate Systems for Uniform Elliptical Vortices (UEV) and the Self-induced Flow Field

We consider a UEV whose centroid is located at the origin of the Lagrangian frame denoted by (x, y) with $z = x + iy$ (Fig. 2.1). The semi-major axis, a , and semi-minor axis, b , of the ellipse define a UEV fixed coordinate system denoted by (X, Y) with $Z = X + iY$ (Fig. 2.2). The angle θ in Fig. 2.1 is called the inclination

(or tilting) angle of the UEV and provides the relation between two coordinate systems (x, y) and (X, Y) as follows

$$\begin{aligned}\underline{x} &= R(\theta)\underline{X} \\ z &= e^{i\theta}Z,\end{aligned}$$

where

$$\underline{x} = \begin{pmatrix} x \\ y \end{pmatrix}, \underline{X} = \begin{pmatrix} X \\ Y \end{pmatrix}, R(\theta) = \begin{pmatrix} \cos \theta, -\sin \theta \\ \sin \theta, \cos \theta \end{pmatrix}.$$

The aspect ratio $\eta = a/b$ of a UEV is, by definition, greater than unity and $\eta = 1, \infty$ correspond to a uniform circular vortex and a vortex sheet, respectively. The area of the UEV $A_E = \pi ab$ and the total circulation $\Gamma = \omega_E A_E$ are invariants in the flow. We define the mean core radius, Λ , of a UEV to be the radius of a circle with center at the center of the UEV that encloses a region of area A_E . Since A_E is an invariant, Λ is also an invariant.

The velocity field induced by a vorticity distribution $\omega(x, y)$ is computed by the Biot-Savart law (see Batchelor [1967]). For an elliptical vortex (EV) of arbitrary vorticity distribution (i.e., a vortex blob whose vorticity contours are all aligned ellipses of the same aspect ratio η (see Appendix 1 for more details)), the self-induced velocity in the vortex fixed coordinate system is written in complex form as follows

$$\dot{Z}^*(Z; \Gamma, \Lambda, \eta) = \frac{\Gamma}{2\pi i \Lambda} \int_0^{\hat{R}} \left(\frac{\hat{R}}{\Lambda} \right) f \left(\frac{\hat{R}}{\Lambda} \right) H \left(\frac{Z}{\Lambda}, \frac{\hat{R}}{\Lambda}, \eta \right) d \left(\frac{\hat{R}}{\Lambda} \right), \quad (2.1)$$

where

$$R^2 = \frac{1}{\eta} (X^2 + \eta^2 Y^2)$$

$$\omega(X, Y) = \frac{\Gamma}{\pi} f \left(\frac{R}{\Lambda} \right)$$

$$H \left(\frac{Z}{\Lambda}, \frac{R}{\Lambda}, \eta \right) = \frac{1}{\pi} \frac{1}{\sqrt{\left(\frac{Z}{\Lambda} \right)^2 - \left(\frac{\eta^2 - 1}{\eta} \right) \left(\frac{R}{\Lambda} \right)^2}}$$

$$\int_0^{2\pi} \int_0^\infty f \left(\frac{R}{\Lambda} \right) \left(\frac{R}{\Lambda} \right) d \left(\frac{R}{\Lambda} \right) d\varphi = \pi.$$

and \dot{Z}^* is the velocity conjugate at Z , R is the mean core radius of the ellipse going through Z , Λ is the core radius of the vorticity distribution and $f(\frac{\hat{R}}{\Lambda})$ is a normalized vorticity distribution. Eqn. (2.1) implies that the contribution to the self-induced velocity at Z comes only from the vorticity in the interior of a smaller ellipse with aspect ratio η with boundary passing through Z . Applying Eqn. (2.1) to a UEV with

$$f\left(\frac{\hat{R}}{\Lambda}\right) = \begin{cases} 1 & \text{for } \frac{\hat{R}}{\Lambda} \leq 1 \\ 0 & \text{for } \frac{\hat{R}}{\Lambda} > 1, \end{cases}$$

We obtain the self-induced velocity field around the UEV in the (X, Y) coordinates as follows

Inside the vortex ($\frac{R}{\Lambda} \leq 1$)

$$\begin{aligned} \dot{Z}_{in}^* &= \frac{\partial}{\partial Y} \Psi_{in} + i \frac{\partial}{\partial X} \Psi_{in} \\ &= \frac{\Gamma}{i\pi\Lambda^2} \frac{1}{\eta + 1} (-X + i\eta Y) ; \end{aligned} \tag{2.2a}$$

Outside the vortex ($\frac{R}{\Lambda} > 1$)

$$\begin{aligned} \dot{Z}_{out}^* &= \frac{\partial}{\partial Z} F_{out} = \frac{\partial}{\partial Z} (\Phi_{out} + i\Psi_{out}) \\ &= \frac{\Gamma}{i\pi D} \left(Z - \sqrt{Z^2 - D} \right) , \end{aligned} \tag{2.2b}$$

where

$$D = \frac{\eta^2 - 1}{\eta} \Lambda^2.$$

\dot{Z}^* is a velocity conjugate at $Z = X + iY$, Φ, Ψ and F are potential, stream and complex potential functions in the UEV fixed coordinate respectively, and the subscripts “in” and “out” stand for “inside” and “outside”, respectively. Since the flow exterior to the UEV is irrotational, a complex potential function can be used to

describe the flow field. The associated stream function Ψ_{in} and complex potential function F_{out} may be written as follows

$$\Psi_{in} = -\frac{\Gamma}{2\pi} \left\{ \frac{1}{\Lambda^2(\eta+1)} (\eta Y^2 + X^2) + \log \left(\frac{\eta+1}{2\sqrt{\eta}} \Lambda \right) - \frac{1}{2} \right\}$$

$$\begin{aligned} F_{out} &= \Phi_{out} + i\Psi_{out} \\ &= \frac{\Gamma}{i2\pi} \log \left(\frac{Z + \sqrt{Z^2 - D}}{2} \right) + \frac{\Gamma}{i2\pi D} \left(Z^2 - Z\sqrt{Z^2 - D} - \frac{D}{2} \right). \end{aligned}$$

Fig. 2.3 shows typical stream lines around a UEV. The constants in Ψ_{in} and F_{out} are chosen so that 1) F_{out} asymptotically approaches the complex potential function for a point vortex, $F_{pt} = \frac{\Gamma}{i2\pi} \log Z$, as $|\frac{Z}{\Lambda}| \rightarrow \infty$, i.e., the stream functions are independent of vortex shape as $|\frac{Z}{\Lambda}| \rightarrow \infty$, and 2) the stream functions for outside and inside of the vortex agree on the UEV boundary,

$$1. \quad \lim_{|\frac{Z}{\Lambda}| \rightarrow \infty} (F_{out} - F_{pt}) = 0$$

$$\lim_{|\frac{Z}{\Lambda}| \rightarrow \infty} \frac{\partial}{\partial \eta} F_{out}, \frac{\partial}{\partial \theta} F_{out} = 0$$

$$2. \quad \Psi_{in} = \Psi_{out} \quad \text{on} \quad \frac{1}{\eta}(X^2 + \eta^2 Y) = R^2 = \Lambda^2.$$

The choice of the constants is very important in evaluating the excess kinetic energy of the UEV as we will see in Section 2.3.

2.2 The external linear flow field

The external linear flow field can be decomposed into a straining field which is irrotational, and a background vorticity field which is rotational, and expressed

as follows

$$\begin{aligned} \dot{z}_L^* &= \dot{z}_S^* + \dot{z}_R^* = \frac{\partial}{\partial y} \psi_L + i \frac{\partial}{\partial x} \psi_L \\ \dot{z}_S^* &= \frac{\partial}{\partial z} f_S = \frac{\partial}{\partial z} (\phi_S + i\psi_S) \\ &= \gamma e^{-2i\alpha} z \end{aligned} \tag{2.3}$$

$$\begin{aligned} \dot{z}_R^* &= \frac{\partial}{\partial y} \psi_R + i \frac{\partial}{\partial x} \psi_R \\ &= \frac{\omega_R}{2i} z^* , \end{aligned}$$

where \dot{z}^* 's are the velocity conjugates at $z = x + iy$ in the Lagrangian frame, and the subscripts "L," "S" and "R" stand for "external linear," "strain" and "rotation," respectively. ϕ , ψ and f are potential, stream and complex stream functions in the Lagrangian frame respectively; γ is the strength of the straining field, α is the angle between the Lagrangian coordinate and the strain axis as shown in Fig. 2.4, and ω_R is the background vorticity which is equivalent to the angular velocity of the rotation of the Lagrangian frame in the absolute coordinate system. The combination of three parameters (γ, α, ω_R) can describe any linear flow field in two-dimensional incompressible flow. The associated complex potential function for the straining field, f_S , and stream function for background vorticity field, Ψ_R , are as follows:

$$f_S = \phi_S + i\psi_S = \frac{\gamma}{2} e^{-2\alpha i} z^2$$

and

$$\psi_R = \frac{\omega_R}{4} (x^2 + y^2) .$$

Fig. 2.4 shows typical stream lines for both linear flow fields.

2.3 Conserved quantities

For two-dimensional incompressible inviscid flow in an infinite domain, the following four quantities are conserved in the absolute coordinate system (\hat{x}, \hat{y}) which is fixed in space.

Total circulation: Γ_{tot}

$$\Gamma_{tot} = \int \int \omega(\hat{x}, \hat{y}) d\hat{x} d\hat{y}$$

Total linear impulse: \underline{P}_{tot}

$$\underline{P}_{tot} = \int \int \omega(\hat{x}, \hat{y}) \underline{\hat{x}} d\hat{x} d\hat{y}$$

Total angular momentum: Q_{tot}

$$Q_{tot} = \int \int \omega(\hat{x}, \hat{y}) |\underline{\hat{x}}|^2 d\hat{x} d\hat{y}$$

Total excess kinetic energy: KE_{tot}

$$KE_{tot} = \frac{1}{2} \int \int \omega(\hat{x}, \hat{y}) \psi(\hat{x}, \hat{y}) d\hat{x} d\hat{y}$$

Those four quantities evaluated over a UEV in the Lagrangian frame are

Circulation: Γ

$$\Gamma = \int \int \omega_E dx dy = \int \int \omega_E dX dY$$

Linear impulse: \underline{P}

$$\underline{P} = \int \int \omega_E \underline{x} dx dy = 0$$

Angular momentum: Q

$$Q = \int \int \omega_E |\underline{x}|^2 dx dy = \int \int \omega_E |\underline{X}|^2 dX dY = \frac{\Lambda^2 \Gamma}{4} \frac{\eta^2 + 1}{\eta}$$

Excess kinetic energy: KE

$$KE = KE_E + KE_S + KE_R$$

where

$$\begin{aligned}
 KE_E &= \frac{1}{2} \int \int \omega_E \psi_{in} dx dy = \frac{1}{2} \int \int \omega_E \Psi_{in} dX dY \\
 &= -\frac{\omega_E \Lambda^2 \Gamma}{8} \left\{ \log \frac{(\eta + 1)^2}{\eta} + 2 \log \frac{\Lambda}{2} - \frac{1}{2} \right\} \\
 KE_S &= \frac{1}{2} \int \int \omega_E \psi_S dx dy \\
 &= \frac{\gamma \Lambda^2 \Gamma}{16} \sin 2(\theta - \alpha) \frac{\eta^2 - 1}{\eta} \\
 KE_R &= \frac{1}{2} \int \int \omega_E \psi_R dx dy = \frac{1}{2} \int \int \omega_E \Psi_R dX dY \\
 &= -\frac{\omega_R \Lambda^2 \Gamma}{32} \frac{\eta^2 + 1}{\eta}
 \end{aligned}$$

Since the total circulation is a coordinate free quantity, i.e., $\Gamma = \text{const}$, \underline{P} must be identically a zero vector by the definition of the centroid and the Lagrangian frame. The angular momentum, whose integrand is quadratic in (x, y) and a function of distance from the centroid, depends on only η (i.e., is independent of θ). The excess kinetic energy decomposes into three parts, the self-induced effect denoted by E , the external straining effect denoted by S , and the external rotation effect denoted by R . Among them, only KE_S depends on the coordinate in which it is evaluated and hence is a function of η and $\theta - \alpha$.

We define the normalized angular momentum \hat{Q} and excess kinetic energies \widehat{KE} 's as follows:

$$\begin{aligned}
 \hat{Q} &= \frac{\eta^2 + 1}{\eta} \\
 \widehat{KE} &= \widehat{KE}_E + \widehat{KE}_S + \widehat{KE}_R,
 \end{aligned} \tag{2.4}$$

where

$$\begin{aligned}
 \widehat{KE}_E &= \log(\hat{Q} + 2) \\
 \widehat{KE}_S &= -\frac{1}{2} \frac{\gamma}{\omega_E} \sqrt{\hat{Q}^2 - 4} \sin 2(\theta - \alpha) \\
 \widehat{KE}_R &= \frac{1}{4} \frac{\omega_R}{\omega_E} \hat{Q},
 \end{aligned}$$

and the relation between normalized variables and dimensional variables are

$$Q = \frac{\Lambda^2 \Gamma}{4} \hat{Q}$$

$$KE = -\frac{\Lambda^2 \Gamma}{8} \omega_E \widehat{KE},$$

where $\frac{\Lambda^2 \Gamma}{4}$ and $\frac{\Lambda^2 \Gamma \omega_E}{8}$ are invariant. In Section 2.4, we will see that the UEV dynamics (i.e., how the UEV changes its configuration) can be understood as the change of (normalized) angular momentum of the UEV and the UEV tilting angle through the vortex interaction, while total excess kinetic energy is conserved in an entire flow domain.

2.4 Ordinary differential equations (O.D.E.'s) describing UEV motion

The equations of motion of a UEV in an arbitrary steady external linear flow field were first obtained by Kida [1981] and can be used to construct exact solutions of Euler equations for prescribed flow field.

By following the time evolution of the boundary vorticity of a UEV in the flow field, Kida found that the UEV keeps its elliptically shaped boundary while the semi-major axis, the semi-minor axis and the inclination angle change in time. The possible motions of the UEV include steady states, oscillation, rotation, asymptotically approaching a steady state and irreversible elongation, depending on the initial configuration and external flow parameters, i.e., $(\gamma/\omega_E, \alpha, \omega_R/\omega_E)$. The existence of such solutions strictly depends on the facts that the total velocity field inside of the vortex is linear, and the vortex boundary shape is quadratic in (x, y) .

Neu [1984] showed a systematic way of deriving O.D.E.'s for the variables (a, b, θ) , although Neu only considered the time-independent (steady) straining effects and included neither time dependence of the flow field nor the background vorticity effects. Following Neu's outline, we obtain the equations of motion of the UEV in an arbitrary time-dependent external linear flow field. Note that, since the area of the UEV is an invariant in the flow, the UEV configuration is defined by two variables (η, θ) . Moreover, the O.D.E.'s for those two variables give the complete dynamics of the UEV.

The equation of the UEV boundary may be written as follows

$$\underline{x}^T E(\eta, \theta; \Lambda) \underline{x} = 1 ,$$

where the matrix $E(\eta, \theta; \Lambda)$ is defined as follows

$$E(\eta, \theta; \Lambda) = \frac{1}{\Lambda^2} R(\theta) \begin{pmatrix} \frac{1}{\eta}, 0 \\ 0, \eta \end{pmatrix} R(-\theta) .$$

Since vorticity moves with the local fluid velocity, we have

$$\frac{D}{Dt} \{ \underline{x}^T E(\eta, \theta; \Lambda) \underline{x} \} = \frac{D}{Dt} 1 = 0 . \quad (2.5)$$

The velocity vector $\frac{D}{Dt} \underline{x} = \dot{\underline{x}}$ on the UEV boundary for time-dependent external linear flow field $(\gamma(t), \alpha(t), \omega_R(t))$ is given by Eqns. (2.2) and (2.3).

$$\dot{\underline{x}} = \dot{\underline{x}}_E + \dot{\underline{x}}_S + \dot{\underline{x}}_R = U(\eta, \theta; \omega_E; \gamma, \alpha, \omega_R) \underline{x} . \quad (2.6)$$

where

$$U(\eta, \theta; \omega_E; \gamma, \alpha, \omega_R) = \frac{-\omega_E}{\eta + 1} R(\theta) \begin{pmatrix} 0, \eta \\ -1, 0 \end{pmatrix} \underline{R}(-\theta) \\ + \gamma R(\alpha) \begin{pmatrix} 1, 0 \\ 0, -1 \end{pmatrix} R(-\alpha) + \frac{\omega_R}{2} \begin{pmatrix} 0, 1 \\ -1, 0 \end{pmatrix} .$$

Substituting Eqn. (2.6) into Eqn. (2.5) yields

$$\frac{D}{Dt} E + U^T E + E U = 0 .$$

Consequently

$$\begin{pmatrix} \frac{d\eta}{dt} \\ \frac{d\theta}{dt} \end{pmatrix} = \begin{pmatrix} 2\gamma(t)\eta \cos 2(\theta - \alpha) \\ \frac{\omega_E \eta}{(\eta+1)^2} - \gamma(t) \frac{\eta^2+1}{\eta^2-1} \sin 2(\theta - \alpha(t)) + \frac{\omega_R(t)}{2} \end{pmatrix} . \quad (2.7)$$

At $\eta = 1$, the UEV becomes circular and the semi-major, -minor axes can not be defined over the UEV. This results in the singularity of the equation at $\eta = 1$.

2.5 Change of variables

As is mentioned in the previous section, two O.D.E.'s for (η, θ) in Eqn. (2.7) may describe the dynamics of the UEV. In this paper, however, we adopt two

sets of transformations of variables to convert Eqn. (2.7) into nondimensionalized Hamiltonian systems which facilitates the use of modern techniques from dynamical systems theory. The techniques, including Poincaré maps, Melnikov methods, and KAM theory, provide us with new results on the dynamics of UEV in a time dependent external flow field, as we will see in the next two chapters.

We define nondimensionalized external flow field parameters as

$$(\gamma, \alpha, \omega_R) \mapsto (\sigma, \alpha, \kappa) = \left(\frac{\gamma}{\omega_E}, \alpha, \frac{\omega_R}{\omega_E} \right) .$$

where σ is the strain - UEV vorticity rate and κ is background vorticity - UEV vorticity rate.

The first set of variables that we define has nice physical interpretations of angular momentum of the UEV and half the inclination angle. Furthermore, the Hamiltonian corresponds to the total excess kinetic energy in the entire flow field. Let us define a new set of variables.

$$(\bar{Q}, \varphi, \tau) = (\hat{Q} + q_c, 2\theta, 2\omega_E t) ,$$

where $\hat{Q} = \frac{\eta^2 + 1}{\eta}$ is the normalized angular momentum of the UEV as is defined in Eqn. (2.4), q_c is an arbitrary constant, φ is twice the UEV inclination angle and τ is a normalized time variable.

By this transformation, Eqn. (2.7) is converted into a Hamiltonian formulation for any q_c ,

$$\begin{pmatrix} \frac{d\bar{Q}}{d\tau} \\ \frac{d\varphi}{d\tau} \end{pmatrix} = \begin{pmatrix} \sigma \sqrt{(\bar{Q} - q_c)^2 - 4} \cos\left(\varphi - \frac{\alpha}{2}\right) \\ \frac{1}{(\bar{Q} - q_c) + 2} - \sigma \frac{\bar{Q} - q_c}{\sqrt{(\bar{Q} - q_c)^2 - 4}} \sin\left(\varphi - \frac{\alpha}{2}\right) + \frac{\kappa}{2} \end{pmatrix} = \begin{pmatrix} -\frac{\partial \bar{H}}{\partial \varphi} \\ \frac{\partial \bar{H}}{\partial \bar{Q}} \end{pmatrix} ,$$

where

$$\begin{aligned} \bar{H}(\bar{Q}, \varphi; \sigma, \alpha, \kappa) &= \bar{H}_E(\bar{Q}) + \bar{H}_S(\bar{Q}, \varphi; \sigma, \alpha) + \bar{H}_R(\bar{Q}; \kappa) \\ \bar{H}_E(\bar{Q}) &= \log\{(\bar{Q} - q_c) + 2\} = \widehat{K E}_E \\ \bar{H}_S(\bar{Q}, \varphi; \sigma, \alpha) &= -\sigma \sqrt{(\bar{Q} - q_c)^2 - 4} \sin\left(\varphi - \frac{\alpha}{2}\right) = 2\widehat{K E}_S \\ \bar{H}_R(\bar{Q}; \kappa) &= \frac{\kappa}{2} \bar{Q} = 2\widehat{K E}_R . \end{aligned} \tag{2.8}$$

From Eqn. (2.8) we can easily see that the Hamiltonian corresponds to the normalized excess kinetic energy. The terms \bar{H}_E , \bar{H}_S , and \bar{H}_R represent the contribution to the Hamiltonian from the UEV, the external strain, and the external vorticity, respectively. The facts that the total excess kinetic energy must be conserved in the entire flow domain and $\widehat{K\bar{E}}_{S,R}$ are induced by the external velocity field (i.e., $\widehat{K\bar{E}}_S$ by vortex interaction and $\widehat{K\bar{E}}_R$ by rotation of the Lagrangian frame), give the factor of 2 for \bar{H}_S and \bar{H}_R . This agrees with the results obtained by Melander et al. [1986] using a moment model to describe external straining effects through vortex interactions.

We choose $q_c = -2$ for convenience so that $I > 0$ and redefine

$$(I, \varphi, \tau) = (\hat{Q} - 2 = \frac{(\eta^2 - 1)^2}{\eta}, 2\theta, 2\omega_E t) .$$

The related Hamiltonian formulation is

$$\begin{pmatrix} \frac{dI}{d\tau} \\ \frac{d\varphi}{d\tau} \end{pmatrix} = \begin{pmatrix} \sigma \sqrt{I^2 - 4I} \cos(\varphi - \frac{\alpha}{2}) \\ \frac{1}{I+4} - \sigma \frac{I+2}{\sqrt{I^2+4I}} \sin(\varphi - \frac{\alpha}{2}) + \frac{\kappa}{2} \end{pmatrix} = \begin{pmatrix} -\frac{\partial \bar{H}}{\partial \varphi} \\ \frac{\partial \bar{H}}{\partial I} \end{pmatrix}$$

where

$$\begin{aligned} H(I, \varphi; \sigma, \alpha, \kappa) &= H_E(I) + H_S(I, \varphi; \sigma, \alpha) + H_R(I; \kappa) \\ H_E(I) &= \log(I + 4) = \widehat{K\bar{E}}_E \\ H_S(I, \varphi; \sigma, \alpha) &= -\sigma \sqrt{I^2 + 4I} \sin(\varphi - \frac{\alpha}{2}) = 2\widehat{K\bar{E}}_S \\ H_R(I; \kappa) &= \frac{\kappa}{2} I = 2\widehat{K\bar{E}}_R . \end{aligned} \tag{2.9}$$

We call I and φ the modified angular momentum and the modified inclination angle, respectively. The singularities at $I = 0$ in the $\frac{d\varphi}{d\tau}$ equation, which correspond to those at $\eta = 1$ in Eqn. (2.7), can be removed by adopting another set of transformation of variables.

$$(\delta, \zeta, \tau) = (\sqrt{2I} \cos \varphi, \sqrt{2I} \sin \varphi, \tau) .$$

The corresponding Hamiltonian system is

$$\begin{pmatrix} \frac{d\delta}{d\tau} \\ \frac{d\zeta}{d\tau} \end{pmatrix} = \begin{pmatrix} \frac{-2\zeta}{\sqrt{\delta^2 + \zeta^2 + 8}} + \frac{\sigma}{2} \frac{\delta^2 + 2\zeta^2 + 8}{\sqrt{\delta^2 + \zeta^2 + 8}} - \frac{\kappa}{2} \zeta \\ \frac{2\delta}{\sqrt{\delta^2 + \zeta^2 + 8}} - \frac{\sigma}{2} \frac{\delta\zeta}{\sqrt{\delta^2 + \zeta^2 + 8}} + \frac{\kappa}{2} \delta \end{pmatrix} = \begin{pmatrix} -\frac{\partial H}{\partial \zeta} \\ \frac{\partial H}{\partial \delta} \end{pmatrix}$$

$$H(\delta, \zeta; \sigma, \alpha, \kappa) = H_E(\delta, \zeta) + H_S(\delta, \zeta; \sigma, \alpha) + H_R(\delta, \zeta; \kappa) \quad (2.10)$$

$$H_E(\delta, \zeta) = \log \left(\frac{\delta^2 + \zeta^2 + 8}{2} \right)$$

$$H_S(\delta, \zeta; \sigma, \alpha) = -\frac{\sigma}{2} \zeta \sqrt{\delta^2 + \zeta^2 + 8}$$

$$H_R(\delta, \zeta; \kappa) = \frac{\kappa}{4} (\delta^2 + \zeta^2).$$

The transformation from (I, φ, τ) to (δ, ζ, τ) is canonical and a standard operation to remove the singularities (Greenspan and Holmes [1983]).

Neu [1984] also obtained a Hamiltonian formulation for the UEV motion in a steady external straining field. However, the transformation that Neu adopted involved η in the new time variable, and hence real (physical) time is not measured uniformly during the motion of the UEV. This fact makes it difficult to interpret the UEV dynamics in time, especially when we consider a time dependent external linear flow field.

Although the equations of motion are well-formulated in Eqns. (2.9) and (2.10) as Hamiltonian systems, the dynamics of the UEV can be easily understood in terms of the UEV configuration (η, θ) rather than the modified angular momentum and inclination angle (I, φ) . The relations between $(I, \varphi), (\delta, \zeta)$ coordinates and the UEV configuration (η, θ) are as follows. The modified angular momentum I and the aspect ratio η have one-to-one correspondence as shown in Fig. 2.5, and hence any I ($I \geq 0$) uniquely defines the aspect ratio η of the UEV. The longer and thinner UEV has more angular momentum and $\eta = 1, \infty$ correspond to $I = 0, \infty$, respectively. The definition of the modified inclination angle φ strictly depends on the symmetry of the UEV and external linear flow field. Fig. 2.6 shows the relation between (I, φ) and (δ, ζ) . The polar coordinate of (δ, ζ) Cartesian coordinate may be given by $(\sqrt{2I}, \varphi)$. The origin of (δ, ζ) coordinate corresponds to a circular

vortex ($I = 0, \eta = 1$), and the distance from the origin (i.e., $\sqrt{2I}$) has one-to-one correspondence to the aspect ratio η .

2.6 Figures for Chapter 2

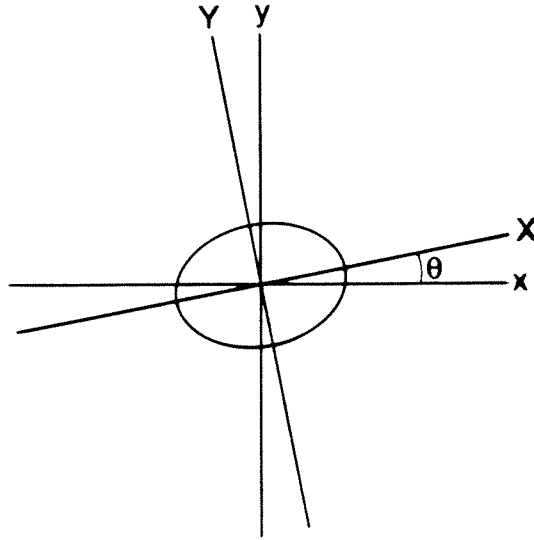


Figure 2.1 Lagrangean coordinate system and the UEV coordinate system

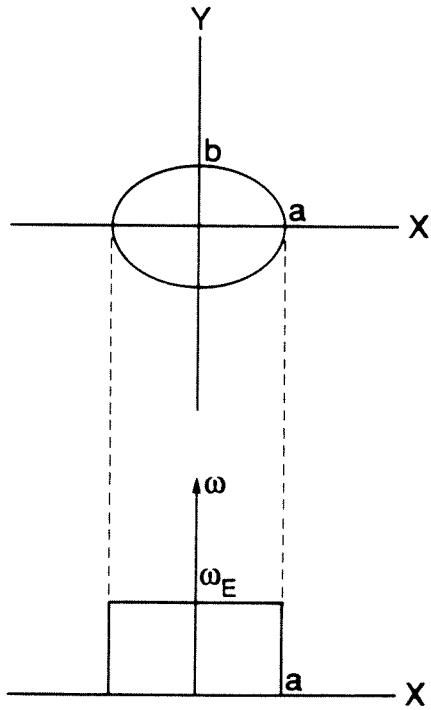


Figure 2.2 UEV configuration and vorticity distribution

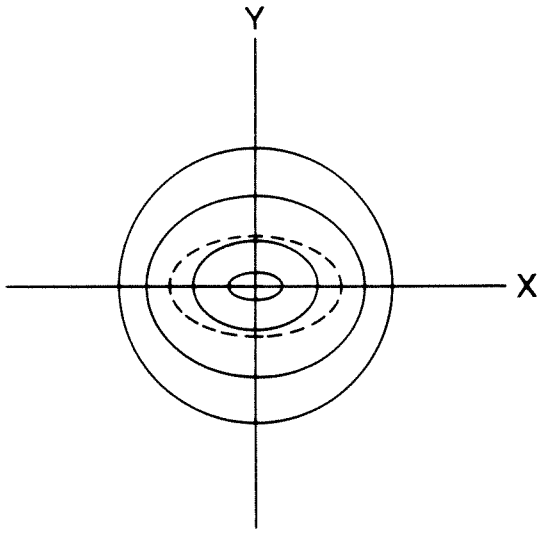


Figure 2.3 Stream lines induced by the UEV

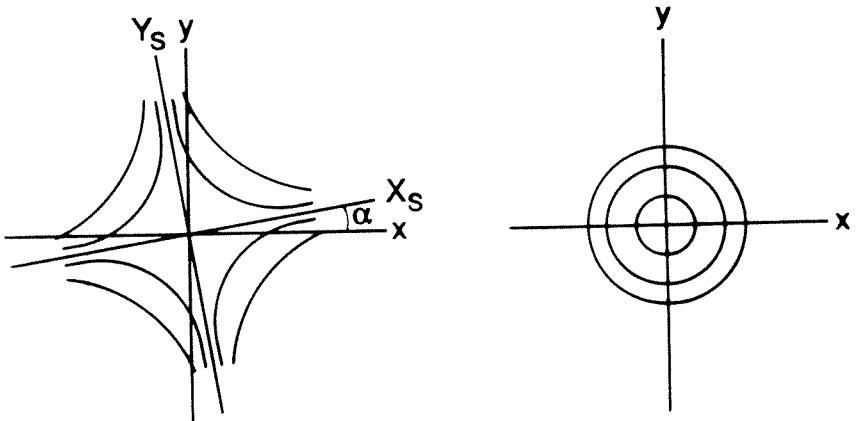


Figure 2.4 Stream lines induced by external linear flow fields
(a) external straining field (b) external rotational field.

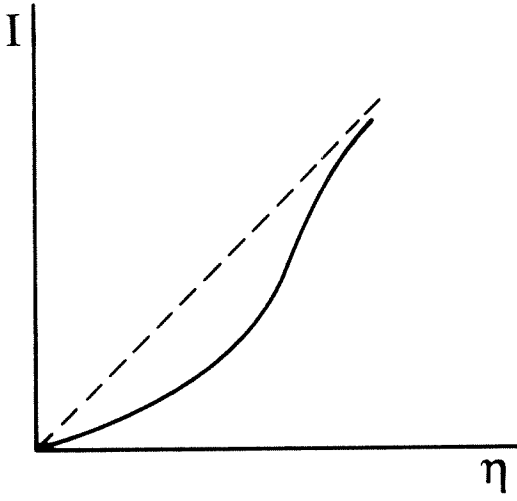


Figure 2.5 Relation between I and η

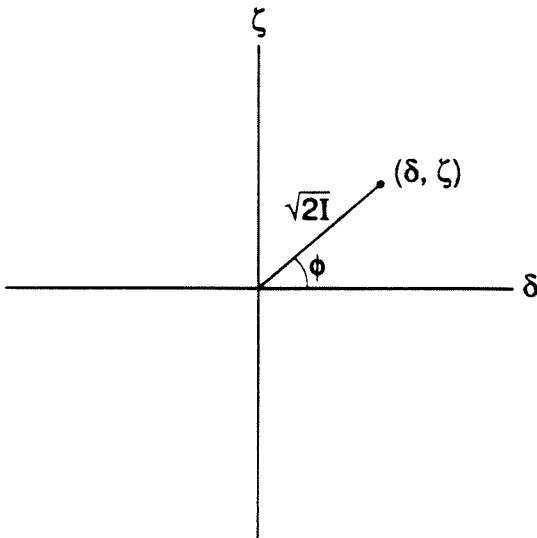


Figure 2.6 Relation between $\delta - \zeta$ phase space and $(\sqrt{2I}, \phi)$ coordinate

Chapter 3

UEV DYNAMICS IN A STEADY EXTERNAL LINEAR FLOW FIELD

In this chapter, we examine the dynamics of a UEV in a time-independent (steady) external linear flow field. For this purpose, we first study Eqn. (2.10) and obtain all the possible solutions, $q(\tau) = (\delta(\tau), \zeta(\tau))$, in the $\delta - \zeta$ phase space as a function of the external flow field parameter values (κ_0, σ_0) , where we can set $\alpha_0 = 0$ without loss of generality by choosing the Lagrangian frame axis to be aligned with the steady straining axis. We show that solutions can exhibit a variety of bifurcations, and we will give the bifurcation diagram in (κ_0, σ_0) parameter space, which agrees with Kida's results [1981]. We will give an interpretation of each orbit in the $\delta - \zeta$ phase space in terms of UEV motion. We will see that, even in a steady external linear flow field, there are quite a few possibilities for UEV motion depending on the initial configuration and external flow field parameter value. Finally, we will give an interpretation of the causes of the different UEV motions by examining the effects due to the self-induced motion, the external straining field and the rotational field.

3.1 Dynamics and bifurcation of Eqn. (2.10)

In this section, we present all the possible solutions of Eqn. (2.10) in the $\delta - \zeta$ phase space as a function of the parameters (κ_0, σ_0) . Because the system is autonomous and Hamiltonian, the solution curves in the $\delta - \zeta$ phase space are given by the level curves of the Hamiltonian function (H). This illustrates one of the advantages of the Hamiltonian formulation. (See Wiggins [1988]). An important feature of this problem is that the solution structure in the $\delta - \zeta$ phase space may change as the parameters are varied, i.e., bifurcations occur. (See Chow and Hale [1982]). We begin by discussing some typical orbits in the $\delta - \zeta$ phase space, and

then consider the solution structure and bifurcations in relation to the parameter values.

The possible motions, for any parameter values, are one of the following: (1) fixed points, (2) periodic orbits, (3) homoclinic orbits, (4) orbits connecting a hyperbolic fixed point to infinity, and (5) unbounded orbits. We describe each orbit more precisely.

(1) A fixed point is where the right hand side of Eqn. (2.10) is identically zero and hence the orbit remains at that point for all time. In a Hamiltonian system, fixed points are generically classified into two types according to its linearized stability.

(a) A hyperbolic fixed point, $q_h = (\delta_h, \zeta_h)$, is a fixed point where the eigenvalues associated with the linearized equations at q_h are real and of opposite sign. q_h possesses an invariant stable manifold denoted by $W^s(q_h)$ and an invariant unstable manifold denoted by $W^u(q_h)$ which are tangent to the eigenvectors associated with the linearized equations at q_h as shown in Fig. 3.1. Solutions starting on $W^s(q_h)$ ($W^u(q_h)$ resp.) approaches q_h asymptotically as $\tau \rightarrow \infty$ ($\tau \rightarrow -\infty$, resp.).

(b) An elliptic fixed point, $q_e = (\delta_e, \zeta_e)$, is a fixed point where the eigenvalues associated with the linearized equations at q_e are pure imaginary and of opposite sign. As shown in Fig. 3.2, q_e is typically surrounded by a one-parameter family of periodic orbits which we will define next.

(2) A periodic orbit, $q^H(\tau) = (\delta^H(\tau), \zeta^H(\tau))$, parametrized by the corresponding Hamiltonian value H , is represented as a closed curve in the $\delta - \zeta$ phase space and is time periodic with period T^H , i.e., $q^H(\tau + T^H) = q^H(\tau)$ for any τ . Periodic orbits associated with $H \in (H_1, H_2)$ are said to belong to a one-parameter family. The condition (see Fig. 3.3)

$$\frac{\partial}{\partial H} T^H \neq 0 \quad \text{for } H \in (H_1, H_2)$$

is referred to as the non-zero twist condition. If Eqn. (3.1) is violated, we will see that interesting dynamical phenomena may occur.

- (3) A homoclinic orbit is an orbit which connects a hyperbolic fixed point q_h to itself. Or, in other words, a branch of $W^s(q_h)$ and $W^u(q_h)$ coincide as shown in Fig. 3.4. If the region interior to a homoclinic orbit contains only periodic orbits around an elliptic fixed point q_e , then those periodic orbits typically belong to a one-parameter family parametrized by $H \in (H_1, H_2)$ where $H_1 = H(q_e)$ and $H_2 = H(q_h)$ as shown in Fig. 3.4. The period, T^H , approaches $2\pi/\Omega_e$ as $H \rightarrow H(q_e)$ where Ω_e is the absolute value of the eigenvalues of the linearized equations at q_e , approaches infinity as $H \rightarrow H(q_h)$.
- (4) A branch of $W^s(q_h)$ or $W^u(q_h)$ come together at a sink at infinity forming two heteroclinic orbits (Keith and Rand [1985]).
- (5) An unbounded orbit approaches infinity in both positive and negative time.

Now we consider the solution structure in the $\delta - \zeta$ phase space corresponding to different parameter values (κ_0, σ_0) . The curves $S^\pm, G^\pm, I_1^\pm, I_2^\pm, U^\pm$ and R in Fig. 3.5 are called bifurcation curves and define the boundaries of the regions in the (κ_0, σ_0) plane corresponding to topologically distinct orbit structures. Note that the bifurcations on G^\pm and U^\pm are associated with the singularities at $I = 0$ in Eqn. (2.9) and they are not bifurcations in the $\delta - \zeta$ phase space in a strict sense. However, since the UEV motion exhibits qualitatively different dynamics upon crossing these curves, we treat them as bifurcations. We now give a brief description of the dynamics near the bifurcation curves $S^+, G^+, I_1^+, I_2^+, U^+$ and R . The description for S^-, G^-, I_1^- and I_2^- follows by the symmetry of the system as we discussed in the previous chapter. See Appendix 2 for derivation of the bifurcation curves. The numbers $1^\pm, \dots, 17^\pm, 18, 19, 20, 21$ and 22 label the phase portraits in the different regions shown in Fig. 3.13.

S^+ : Saddle-node bifurcation

As we cross S^+ from above to below, (e.g., in crossing S^+ from 7^+ to 5^+ , 8^+ to 10^+ , or 17^+ to 15^+ as shown in Fig. 3.13) a hyperbolic fixed point, q_h^+ , and an elliptic fixed point, q_e^+ , are born on the positive ζ -axis ($\varphi = \frac{\pi}{2}$) with q_h^+ above q_e^+ as shown in Fig. 3.6. Since this is a Hamiltonian saddle-node bifurcation, a homoclinic orbit connecting q_h^+ to itself and surrounding q_e^+ , is born at the same time. The interior of the homoclinic orbit contains a one-parameter family of

periodic orbits whose direction of motion is counterclockwise (c-c) around q_e^+ . For (κ_0, σ_0) above both S^+ and I_2^+ (e.g., 7^+ in Fig. 3.13), the $\delta - \zeta$ phase space consists of only unbounded orbits with $\varphi \sim \pi - \sin(\frac{\kappa_0}{2\sigma_0})$ as $\tau \rightarrow -\infty$ and $\varphi \sim \sin(\frac{\kappa_0}{2\sigma_0})$ as $\tau \rightarrow \infty$ where for $\sin(\cdot)$ we take the principle value. As we cross S^+ above I_2^+ (e.g., in crossing S^+ from 7^+ to S^+ in Fig. 3.13), the saddle-node bifurcation takes place; however, the unbounded orbits are still the typical motion in the $\delta - \zeta$ phase space. We will discuss the saddle-node bifurcation that occurs on crossing S^+ below I_2^+ later. Note that fixed points born through the saddle-node bifurcation remain on the positive ζ -axis for any $(\kappa_0, \sigma_0), (\sigma_0 > 0)$ as long as the fixed points exist.

G^+ : Global bifurcation at the origin

As we pass G^+ from above to below (e.g., on crossing G^+ from 5^+ to 3^+ , 10^+ to 12^+ , or 15^+ to 13^+ in Fig. 3.13), the homoclinic orbit crosses the δ -axis and encircles the origin of the $\delta - \zeta$ phase space as shown in Fig. 3.7. This has important dynamical consequences for the UEV motion that we will discuss in Section 3.2.

I_1^+ : Bifurcation at infinity on the positive ζ -axis

As we approach I_1^+ from above (3^+), q_h^+ moves to infinity along the positive ζ -axis, and finally it disappears on I_1^+ . At the same time, the corresponding homoclinic orbit disappears at infinity. This results in that periodic orbits around q_e^+ become the typical motion in the $\delta - \zeta$ phase space in I_1^+ .

U^+ : Bifurcation at the origin for q_e^+

As we cross U^+ from above to below (e.g., in crossing U^+ from 1^+ to 1^- in Fig. 3.13), q_e^+ moves from the positive ζ -axis to the negative ζ -axis as shown in Fig. 3.8.

I_2^+ : Bifurcation at infinity on the negative ζ -axis

As we cross I_2^+ from above to below (e.g., in crossing I_2^+ from 3^+ to 13^+ , 4^+ to 14^+ , 5^+ to 15^+ , 6^+ to 16^+ , or 7^+ to 17^+ in Fig. 3.13), an elliptic fixed point q_e^- is born at infinity on the negative ζ -axis accompanied by clockwise (c) periodic orbits around itself. If we cross I_2^+ below S^+ (e.g., in crossing I_2^+

from 3^+ to 13^+ , 4^+ to 14^+ , or 5^+ to 15^+ in Fig. 3.13), then the branches of $W^s(q_h^+)$ and $W^u(q_h^+)$ which did not belong to the previous homoclinic orbit coincide, forming a new homoclinic orbit enclosing a newborn q_e^- as shown in Fig. 3.9. We call the original homoclinic orbit the inner homoclinic orbit (IHO) and the new homoclinic orbit, the outer homoclinic orbit (OHO). The $\delta - \zeta$ phase space is thus divided into three regions by the IHO and the OHO with a one parameter family of periodic orbits in each region.

Now we return to the saddle-node bifurcation on S^+ below I_2^+ .

S^+ below I_2^+ : Saddle-node bifurcation on a periodic orbit.

As we cross S^+ from above below I_2^+ (e.g., in crossing S^+ from 17 to 15 in Fig. 3.13) q_h^+ and q_e^+ are born on the positive ζ -axis through a saddle-node bifurcation along with a corresponding IHO. Since q_h^+ and q_e^+ are born on a (c) periodic orbit which encircles q_e^- , the periodic orbit turns into an OHO as shown in Fig. 3.10. On the other hand, if we cross S^+ from below to above (e.g., in crossing S^+ from 17^+ to 15^+ in Fig. 3.13), then the OHO turns into a periodic orbit.

U^- : Bifurcation at the origin for q_e^-

As we cross U^- from above to below (e.g., in crossing U^- from 17^+ to 17^- in Fig. 3.13), q_e^- moves from the negative ζ -axis to the positive ζ -axis as shown in Fig. 3.11. This has important dynamical consequences that we will discuss in section 3.2.

R : Ring bifurcation

As we approach R from above, q_e^+ moves toward the origin while both the IHO and the OHO coalesce. On R , q_e^+ reaches the origin and the two homoclinic orbits turn into a circular ring of fixed points in which q_e^- disappears as shown in Fig. 3.12. The ring of fixed points divides the $\delta - \zeta$ phase space into two regions which contain (c-c) circular periodic orbits and (c) circular periodic orbits, respectively. We define this bifurcation as the Ring Bifurcation.

In Fig. 3.13, we show all possible phase portraits as well as the behavior of the period of the periodic orbits.

3.2 UEV motion

Having described the solutions of Eqn. (2.10) in the $\delta - \zeta$ phase space as a function of the parameter (κ_0, σ_0) , we now interpret these solutions in terms of the UEV motion.

The interpretation of the dynamics of a UEV moving along a constant H curve is that the total excess energy of the entire flow field is conserved while the angular momentum and excess kinetic energy of the UEV change as the UEV evolves in the flow field. In other words, the deformation of the UEV, which results in the change of the angular momentum and inclination angle of the principle axis (semi-major axis), is caused so as to conserve the total excess kinetic energy through the vortex interaction.

The bifurcation analysis was most easily performed in the $\delta - \zeta$ coordinate system. However, for describing the motion of the UEV in physical space it will often be more clear to return to either the (η, θ) coordinates or the (I, φ) coordinates. Recall from Chapter 2 that $\theta = \frac{\varphi}{2}$, $\eta = \frac{a}{b}$, and $I = \frac{(\eta-1)^2}{\eta}$ with $(\delta, \zeta) = (\sqrt{2I} \cos \varphi, \sqrt{2I} \sin \varphi)$. We make the important remark that all rescalings of time were by constant factors. This is very important when we consider time dependent external velocity fields. Since the UEV dynamics can be understood as the change of UEV configuration (η, θ) and/or motion of a point at the tip of UEV semi-major axis $(\sqrt{\eta}, \theta)$, we first define the terminology for two main features of UEV dynamics in terms of the rate of change in (I, φ) . We call $\frac{dI}{d\tau}$ the deformation rate of the vortex shape and note that $\frac{dI}{d\tau} > 0$ implies $\frac{d\eta}{d\tau} > 0$ which corresponds to elongation of a UEV. Similarly, $\frac{dI}{d\tau} < 0$ implies $\frac{d\eta}{d\tau} < 0$ which corresponds to contraction of a UEV. Additionally, we refer to $\frac{d\varphi}{d\tau}$ as the modified angular velocity of the semi-major axis. In general, we can have $\frac{d\varphi}{d\tau} > 0$ or $\frac{d\varphi}{d\tau} < 0$ corresponding to counterclockwise (c-c) motion or clockwise (c) motion, respectively.

We next describe the five typical orbits described in Section 3.1 in terms of UEV motion.

- (1) A fixed point corresponds to a steady UEV which does not change its configuration (η, θ) for all time. A hyperbolic fixed point q_h (an elliptic fixed point q_e , resp.) corresponds to an unstable (stable, resp.) steady UEV. Any UEV

whose initial configuration (IC) is slightly shifted from a stable steady UEV configuration undergoes a periodic oscillatory motion with small change in its configuration, which corresponds to a periodic orbit around q_e , as we will see in (2). This may not be the case for a UEV whose IC is slightly perturbed from an unstable steady UEV configuration. Since all the fixed points q_h^+ , q_e^\pm in the $\delta - \zeta$ phase space exist only on the ζ -axis, a UEV can be steady only at some special inclination angle, i.e., $\theta(= \frac{\varphi}{2}) = \frac{\pi}{4}$ which corresponds to q_h^+ and q_e^+ and $\theta(= \frac{\varphi}{2}) = \frac{3\pi}{4}$ which corresponds to q_e^- .

- (2) The periodic motions of the UEV can be classified into six distinct types depending on 1) the direction of motion and 2) whether or not the periodic orbit contains the origin (in the $\delta - \zeta$ plane) in its interior. If the origin is not contained inside the interior of the periodic orbit then the angle φ cannot exceed 2π . This periodic motion is referred to as oscillation. If the origin is contained in the interior of the periodic orbit, then φ can increase through 2π , and the resulting periodic motion is referred to as rotation. In the case of a periodic orbit passing through the origin, the angle φ becomes undefined at the origin. This critical periodic orbit is special in that it separates oscillation from rotation. We refer to it as a periodic boundary orbit (PBO).

Hence the six types of periodic motions are

- 1) Oscillation about $\theta(= \frac{\varphi}{2}) = \frac{\pi}{4}$. In this case the tip of the semi-major axis of the UEV moves along a closed curve in a counterclockwise sense.
- 2) Rotation in a counterclockwise sense.
- 3) Counterclockwise periodic orbit passing through the origin.
- 4) Oscillation about $\theta(= \frac{\varphi}{2}) = \frac{3\pi}{4}$. In this case the top of the semi-major axis of the UEV moves along a closed curve in a clockwise sense.
- 5) Rotation in a clockwise sense.
- 6) Clockwise periodic orbit passing through the origin.

We illustrate different types of periodic orbits in the $\delta - \zeta$ phase plane in Figs. 3.14a and 3.14b, the right dashed hatched region, the right solid hatched region,

the left dashed hatched region and the left solid hatched region correspond to (e-c) oscillation around $\theta^{(c-c)} = \frac{\pi}{4}$, (c-c) rotation, (c) oscillation around $\theta^{(c)} = \frac{3\pi}{4}$ and (c) rotation, respectively.

Also note from Fig. 3.13 that the regions corresponding to periodic orbits in the $\delta - \zeta$ phase space are either unbounded or bounded by homoclinic orbits depending on parameter value (κ_0, σ_0) . We discuss this in more detail next.

- (3) A homoclinic orbit corresponds to a UEV motion which asymptotically approaches an unstable steady state in positive and negative time. The motion is said to be rotational or oscillatory depending on whether or not the orbit encloses the origin of the $\delta - \zeta$ phase space. Furthermore, homoclinic orbits define boundaries separating regions of qualitatively distinct UEV motions. If IHO (inner homoclinic orbit) is the only homoclinic orbit in the $\delta - \zeta$ phase space, then it divides the $\delta - \zeta$ plane into an interior region corresponding to a (c-c) periodic motion and an exterior region corresponding to irreversible elongation which we discuss next.

When both IHO and OHO (outer homoclinic orbit) exist in the $\delta - \zeta$ phase space, for some values (κ_0, σ_0) , they define the boundaries of three regions: the interior of IHO ((c-c) periodic motion), the region bounded by IHO and OHO ((c) periodic motion) and the exterior of OHO ((c) periodic motion).

The orbits connecting q_h^+ to infinity, i.e., the branches of $W^s(q_h^+)$ and $W^u(q_h^+)$ which don't belong to a homoclinic orbit, correspond to irreversible contraction of UEV (on $W^s(q_h^+)$) along the contraction axis θ_c and irreversible elongation of UEV (on $W^u(q_h^+)$) along elongation axis θ_e where

$$\theta_c = \frac{\pi}{2} - \sin^{-1} \left(\frac{\kappa_0}{2\sigma_0} \right)$$

$$\theta_e = \sin^{-1} \left(\frac{\kappa_0}{2\sigma_0} \right) .$$

- (4) Unbounded orbits correspond to irreversible elongation of UEV along θ_c and θ_e . These orbits are classified into two types depending on the direction of elongating motion, i.e., (c-c) elongation and (c) elongation. The boundaries of these two regions are defined by some orbits as follows.

Case 1: The origin of the $\delta - \zeta$ phase space is not enclosed by a homoclinic orbit. An unbounded orbit which goes through the origin defines the boundary as shown in Fig. 3.15.

Case 2: The origin of the $\delta - \zeta$ phase space is enclosed by a homoclinic orbit. $W^s(q_h^+)$ and $W^u(q_h^+)$ which connect q_h^+ to infinity define the boundary.

The orbits which define the boundary are called unbounded boundary orbits (UBO's). The unbounded orbits above UBO's in the $\delta - \zeta$ phase space correspond to (c) irreversible elongation and the unbounded orbits below UBO's corresponds to (c-c) elongation. In Figs. 3.15 and 3.16, the vertical (horizontal resp.) hatched region corresponds to (c) ((c-c) resp.) irreversible elongation.

Table 3.1 shows all possible motions of the UEV and their corresponding orbits in the $\delta - \zeta$ phase space together with the boundary orbits which divide regions corresponding to different types of UEV motion. In a steady external linear flow field, the UEV motion associated with orbits in the $\delta - \zeta$ phase space are regular and no transition between qualitatively different regions of motion can happen.

Finally, for a given external flow field parameter value (κ_0, σ_0) , all possible motions of UEV are summarized in Fig. 3.17 where $1^\pm \sim 17^\pm$, $18 \sim 22$ correspond to the parameter set values in the bifurcation diagram (Fig. 3.5).

3.3 The kinetic energy decomposition

UEV motion for a given initial configuration (I_0, φ_0) and an external linear flow field $(\sigma_0, \alpha_0 = 0, \kappa_0)$ is uniquely determined so as to conserve the total excess kinetic energy H of the entire flow domain. In this section, we discuss the decomposition of H into H_E, H_S and H_R as described in chapter 2 and describe how the external flow parameter (κ_0, σ_0) influences the UEV dynamics in terms of these three components of kinetic energy. Fig. 3.18abc shows the level curves of H_E, H_S and H_R in the $\delta - \zeta$ phase space. Because the time variable τ is normalized by the UEV vorticity ω_E , the sign of the Hamiltonian functions H_S and H_R corresponds to the direction of the motion induced by each effect. For example, if $H_S > 0$, then corresponding motion induced by the straining effect is in the same direction as self-induced motion, i.e.,

$\frac{d\varphi}{d\tau}|_S > 0$. Similarly, $H_S < 0$ corresponds to $\frac{d\varphi}{d\tau}|_S < 0$. Note that every level curve of H_E is circular, and H_E has its minimum at the origin ($I = 0$) with $H_E(0) = \log 4$. This results in all periodic motion being (c-c) rotations when $\kappa_0 = \sigma_0 = 0$. In Fig. 3.18b which shows that the level curves of H_S , $\varphi = 0$ and $\varphi = \pi$ correspond to contracting and stretching axes of the straining field, respectively. H_S is negative for $0 < \varphi < \pi$ because the flow field induced by the straining effect acts against the self-induced motion (i.e., the induced flow field is in clockwise direction). H_S is positive for $\pi < \varphi < 2\pi$ because the induced flow field is in the same direction as the self-induced motion. The straining effect is most effective on $\varphi = \frac{\pi}{2}, \frac{3}{2}\pi$ (i.e., a level curve of H_S is tangent to a level curve of H_R on those axes).

Any level curve of H_R is circular as is shown in Fig. 3.18c. If $\kappa_0 > 0$ (i.e., $H_R > 0$), then the flow field induced by the background vorticity is in the same direction as the self-induced motion. H_R has one minimum at $I = 0$, and all the corresponding motions are (c-c). Similarly for $\kappa_0 < 0$, H_R is negative with one maximum at $I = 0$, and all the corresponding motions are (c).

The asymptotic behavior of H_E , H_S and H_R for $I \ll 1$ and $I \gg 1$ is as follows

$$H_E \sim \begin{cases} \log 4 + \frac{1}{4}I & I \ll 1 \\ \log I & I \gg 1 \end{cases}$$

$$H_S \sim \begin{cases} -2\sigma_0\sqrt{I} \sin \varphi & I \ll 1 \\ -\sigma_0 I \sin \varphi & I \gg 1 \end{cases}$$

$$H_R = \frac{\kappa_0}{2} I .$$

For $I \gg 1$ the UEV dynamics is governed by the external flow field. Let us first consider the mechanism of the irreversible elongation. Irreversible elongation, which takes place when H_S dominates H_R for $I \gg 1$, is possible for $\sigma_0 \geq \frac{|\kappa_0|}{2}$. Another way of understanding irreversible elongation is as follows. On the elongation axis for $I \gg 1$, a UEV deforms without change in φ i.e., change in I does not affect H although change in φ does affect H , i.e., $\frac{\partial H}{\partial I} = 0$ and $\frac{\partial H}{\partial \varphi} \neq 0$ on the elongation axis. Note that if H_R dominates H_S for $I \gg 1$, then the UEV undergoes periodic rotation with a large aspect ratio.

Having described the behavior of each of the three components of the kinetic energy, we interpret the bifurcations in phase space in terms of a superposition of the effects of H_E , H_S and H_R . We start with $\sigma_0 = 0$. The number of regions and bifurcation curves are as listed in Fig. 3.5, and see Fig. 3.13 for the phase portraits.

- 22: H has one minimum at $I = 0$ and hence all the periodic motion are (c-c) rotation without deformation.
- 20: H_E and H_R have opposite sign, where H_E (H_R resp.) dominates H_R (H_E resp.) for $I < I_0 = -(\frac{2}{\kappa_0} + 4)$ ($I > I_0$ resp.) H has one minimum at $I = 0$, and a ring of maxima at $I = I_0$. This results in (c-c) rotation for $I < I_0$, steady UEV at $I = I_0$ and (c) rotation for $I > I_0$ without deformation.
- 18: H_E and H_R have opposite sign but H_R dominates H_E in the entire phase space. H has one maximum at $I = 0$ and hence all the periodic motions are (c) rotation without deformation.

When a small straining effect is imposed (i.e., we move off the κ_0 axis), the circular symmetry breaks down, and a small region corresponding to oscillating UEV's is born near $I = 0$. (Note: the notation $1^+(\Leftarrow 22)$ means moving of the κ_0 axis from the segment with phase portraits 22 into the region with phase portraits 1^+ .)

$1^+(\Leftarrow 22), 13^+(\Leftarrow 20)$: The minimum energy point moves up on $\varphi = \frac{\pi}{2}$, and a region corresponding to (c-c) oscillation is created. Furthermore, for the region 13^+ , the ring of maximum energy breaks down and forms two homoclinic orbits enclosing a region corresponding to (c) oscillation.

$17^+(\Leftarrow 18)$: The maximum energy point moves down on $\varphi = \frac{3}{2}\pi$, and a region corresponding to (c) oscillation is born.

As the straining effect becomes stronger, the minimum or maximum energy points move away from $I = 0$ on $\varphi = \frac{\pi}{2}$ or $\frac{3}{2}\pi$, respectively. Note that whether or not H_S and H_R balance determines the existence of a region corresponding to irreversible elongation on the phase space. (Note: the notation $3^+(\stackrel{I_1^+}{\Leftarrow} 1^+)$ implies crossing the bifurcation curve I_1^+ from the region with phase portraits 1^+ into the region with phase portraits 3^+ .)

3^+ ($\stackrel{I_1^+}{\leftarrow} 1^+$): On I_1 , H_S and H_R balance on $\varphi = \frac{\pi}{2}$ at $I + \infty$. In S^+ , there exists one local maximum and one local minimum of excess kinetic energy on $\varphi = \frac{\pi}{2}$. The local maximum, which is a saddle in the phase space, provides a homoclinic orbit going around the local minimum.

7^+ ($\stackrel{I_2^+}{\leftarrow} 17^+$), 5^+ ($\stackrel{I_2^+}{\leftarrow} 15^+$), 3^+ ($\stackrel{I_2^+}{\leftarrow} 13^+$): On I_2 , H_S and H_R balance in $\varphi = \frac{3\pi}{2}$ at $I + \infty$, and H becomes positive on $\varphi = \frac{3\pi}{2}$ with $\frac{\partial}{\partial I}H > 0$ resulting in disappearance of the maximum energy point. It follows that, above I_2 , there exists a region corresponding to irreversible elongation of the UEV.

Saddle-node bifurcation is a combination of effects from three excess kinetic energies.

7^+ ($\stackrel{S^+}{\leftarrow} 5^+$), 17^+ ($\stackrel{S^+}{\leftarrow} 15^+$): On S , the straining effect becomes strong enough to smooth out the local maximum and minimum on $\varphi = \frac{\pi}{2}$.

Now we examine how three components of the excess kinetic energy, H_E , H_S and H_R , interchange during the motion of UEV while the total excess kinetic energy is conserved for a given external flow field (κ_0, σ_0) . From Eqn. (2.9), we have

$$\frac{d}{d\tau}H = 0 = \frac{d}{d\tau}H_E + \frac{d}{d\tau}H_S + \frac{d}{d\tau}H_R .$$

The interchange rates between each excess kinetic energy are

$$\begin{aligned} \frac{d}{d\tau}H_E &= \frac{1}{I+4} \frac{dI}{d\tau} = \sigma_0 \sqrt{\frac{I}{I+4}} \cos \varphi \\ \frac{d}{d\tau}H_S &= - \left(\frac{1}{I+4} + \frac{\kappa_0}{2} \right) \frac{dI}{d\tau} = -\sigma_0 \left(\sqrt{\frac{I}{I+4}} + \frac{\kappa_0}{2} \sqrt{I^2 + 4I} \right) \cos \varphi \\ \frac{d}{d\tau}H_R &= \frac{\kappa_0}{2} \frac{dI}{d\tau} = -\frac{\sigma_0 \kappa_0}{2} \sqrt{I^2 + 4I} \cos \varphi \end{aligned}$$

Each of rate of chnges in kinetic energies are evaluated on the orbit defined by a constant H curve. Since every orbit is symmetric around $\varphi = \frac{\pi}{2}$ and $\frac{3}{2}\pi$ for any parameter (κ_0, σ_0) , we only have to consider the case $-\frac{\pi}{2} < \varphi < \frac{\pi}{2}$.

$\frac{d}{d\tau}H_E$: For any orbit, $\frac{d}{d\tau}H_E > 0$ with $\frac{d}{d\tau}H_E = 0$ on $\varphi = \pm \frac{\pi}{2}$.

$\frac{d}{d\tau}H_S$: For $\kappa_0 > 0$, $\frac{d}{d\tau}H_S < 0$ on any orbit with $\frac{d}{d\tau}H_S = 0$ on $\varphi = I\frac{\pi}{2}$. For $-\frac{1}{2} < \kappa_0 < 0$, $\frac{d}{d\tau}H_S$ may change its sign if the orbit crosses $I_0 = -\frac{2}{\kappa_0} - 4$. The

geometrical relations between I_0 and orbits in 13^+ and 15^+ are shown in Fig. 3.19. For $\kappa_0 < -\frac{1}{2}$, $\frac{d}{d\tau}H_S > 0$ with $\frac{d}{d\tau}H_S = 0$ on $\varphi = \pm\frac{\pi}{2}$.

$\frac{d}{d\tau}H_R$: For $\kappa_0 > 0$, $\frac{d}{d\tau}H_R > 0$ with $\frac{d}{d\tau}H_R = 0$ on $\varphi = \pm\frac{\pi}{2}$. For $\kappa_0 < 0$, $\frac{d}{d\tau}H_R < 0$ with $\frac{d}{d\tau}H_R = 0$ on $\varphi = \pm\frac{\pi}{2}$. For any orbit, $\frac{d}{d\tau}H_E > 0$ with $\frac{d}{d\tau}H_E = 0$ on $\varphi = \pm\frac{\pi}{2}$.

Furthermore, since our analysis of the UEV motion in unsteady external linear flow fields mainly concerns the dynamics along homoclinic orbits and periodic orbits as we will see in chapter 3, we examine $\frac{d}{d\tau}H_E$, $\frac{d}{d\tau}H_S$ and $\frac{d}{d\tau}H_R$ on those orbits. For homoclinic orbits, we choose $\tau = 0$ on ζ -axis (i.e., $\delta(0) = 0$) and examine for $\tau > 0$. For periodic orbits, we choose $\tau = 0$ on ζ -axis with $\zeta(0) < \zeta(\frac{T^H}{2})$, and examine for $0 < \tau < 0\frac{T^H}{2}$.

$\frac{d}{d\tau}H_E$:

$$\frac{d}{d\tau}H_E \begin{cases} > 0 & \text{on IHO} \\ < 0 & \text{on OHO} \\ > 0 & \text{on (c-c) periodic orbit} \\ < 0 & \text{on (c) periodic orbit} \end{cases}$$

$\frac{d}{d\tau}H_R$:

$$\frac{d}{d\tau}H_R \begin{cases} > 0 & \text{on IHO for } \kappa_0 > 0 \\ < 0 & \text{on IHO for } \kappa_0 < 0 \\ < 0 & \text{on OHO} \\ > 0 & \text{on (c-c) orbit for } \kappa_0 > 0 \\ < 0 & \text{on (c-c) orbit for } \kappa_0 < 0 \\ < 0 & \text{on (c) periodic motion} \end{cases}$$

$\frac{d}{d\tau}H_S$:

For $\frac{d}{d\tau}H_S$, we use the following fact.

$$\begin{aligned} \frac{d}{d\tau}H_S &= \frac{d}{d\tau}(H - H_E - H_R) \\ &= -\frac{d}{d\tau}(H_E + H_R) \\ &= -\left(\frac{1}{I+4} + \frac{\kappa_0}{2}\right)\frac{dI}{d\tau} \end{aligned} \tag{3.1}$$

with

$$-\left(\frac{1}{I+4} + \frac{\kappa_0}{2}\right) \begin{cases} < 0 & \text{for } I < I_0 \\ > 0 & \text{for } I > I_0 \end{cases} .$$

As a consequence,

$$\begin{aligned} \frac{d}{d\tau} H_S & \begin{cases} < 0 & \text{on IHO} \\ < 0 & \text{on (c-c) orbit} \\ > 0 & \text{on OHO for } I < I_0 \\ < 0 & \text{on OHO for } I > I_0 \\ > 0 & \text{on (c) orbit for } I < I_0 \\ < 0 & \text{on (c) orbit for } I > I_0 \end{cases} . \end{aligned}$$

Note from Eqn. (3.1) that $\frac{d}{d\tau} H_E$ dominates $\frac{d}{d\tau} H_R$ for $I < I_0$ and $\frac{d}{d\tau} H_R$ dominates $\frac{d}{d\tau} H_E$ for $I > I_0$. $\frac{d}{d\tau} H_S$ balances the difference of $\frac{d}{d\tau} H_E$ and $\frac{d}{d\tau} H_R$.

Some typical behavior of $\frac{d}{d\tau} H_E$, $\frac{d}{d\tau} H_S$ and $\frac{d}{d\tau} H_R$ are shown in Fig. 3.20 for some parameter values, i.e., $(\kappa_0 = 0, \sigma_0) = (0., 0.05)$ for (c-c) periodic orbits (corresponding to oscillation and rotation), and inner homoclinic orbit.

We will see later when we introduce the Melnikov technique that the rate of change in H_S and H_R are very important to understand the UEV dynamics in unsteady external flow field.

3.4 Figures and table for Chapter 3

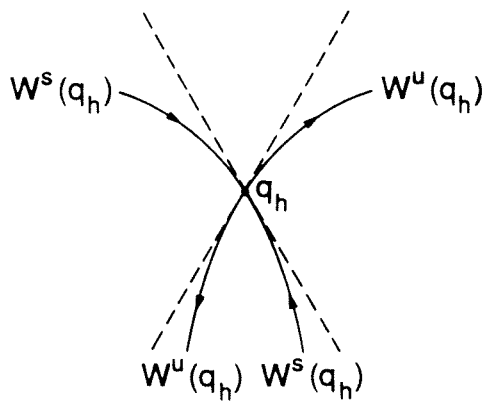


Figure 3.1 A hyperbolic fixed point q_h , a stable manifold $W^s(q_h)$ and a unstable manifold $W^u(q_h)$

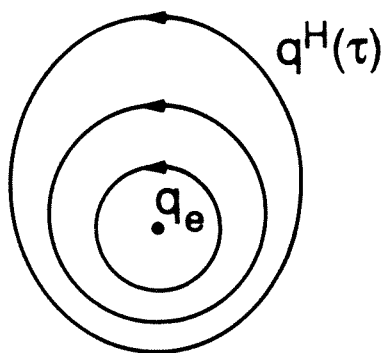


Figure 3.2 An elliptic fixed point q_e

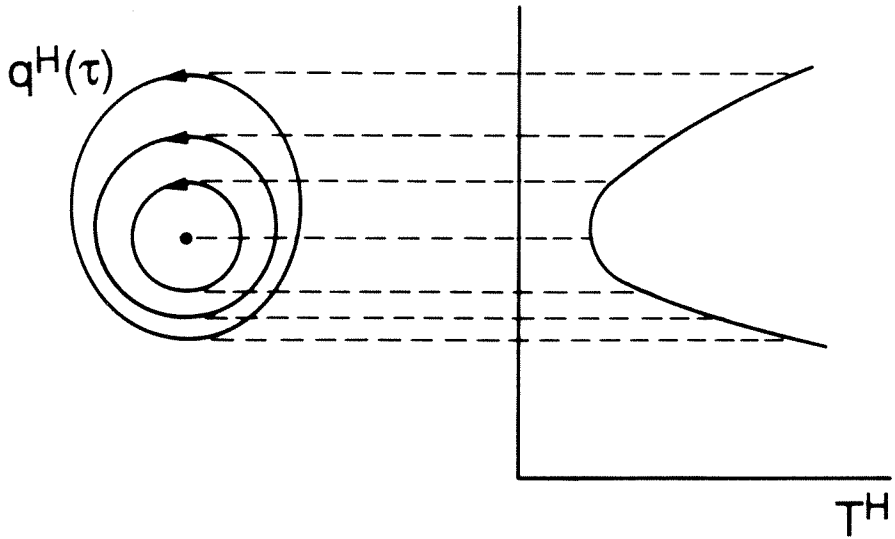


Figure 3.3 One parameter family periodic orbits around an elliptic fixed point q_e

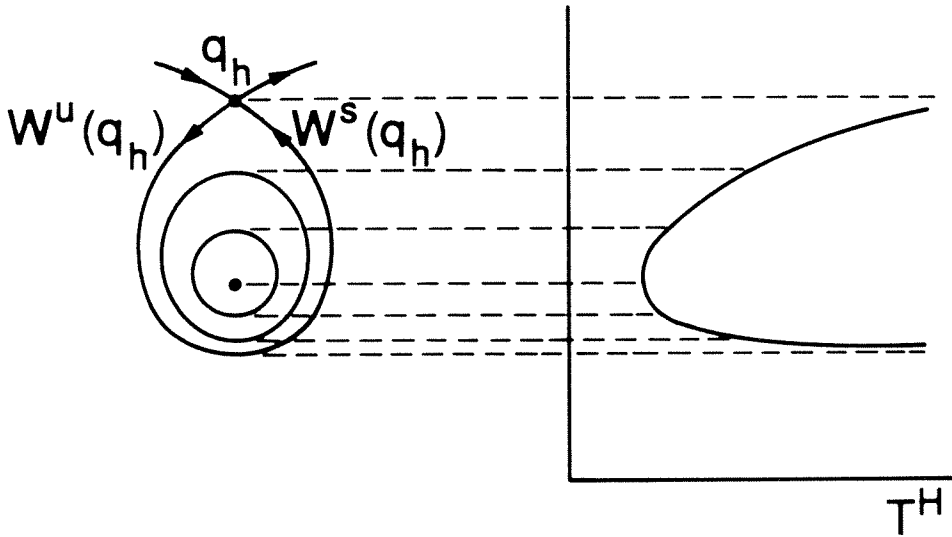


Figure 3.4 A homoclinic orbit and associated one parameter family periodic orbits

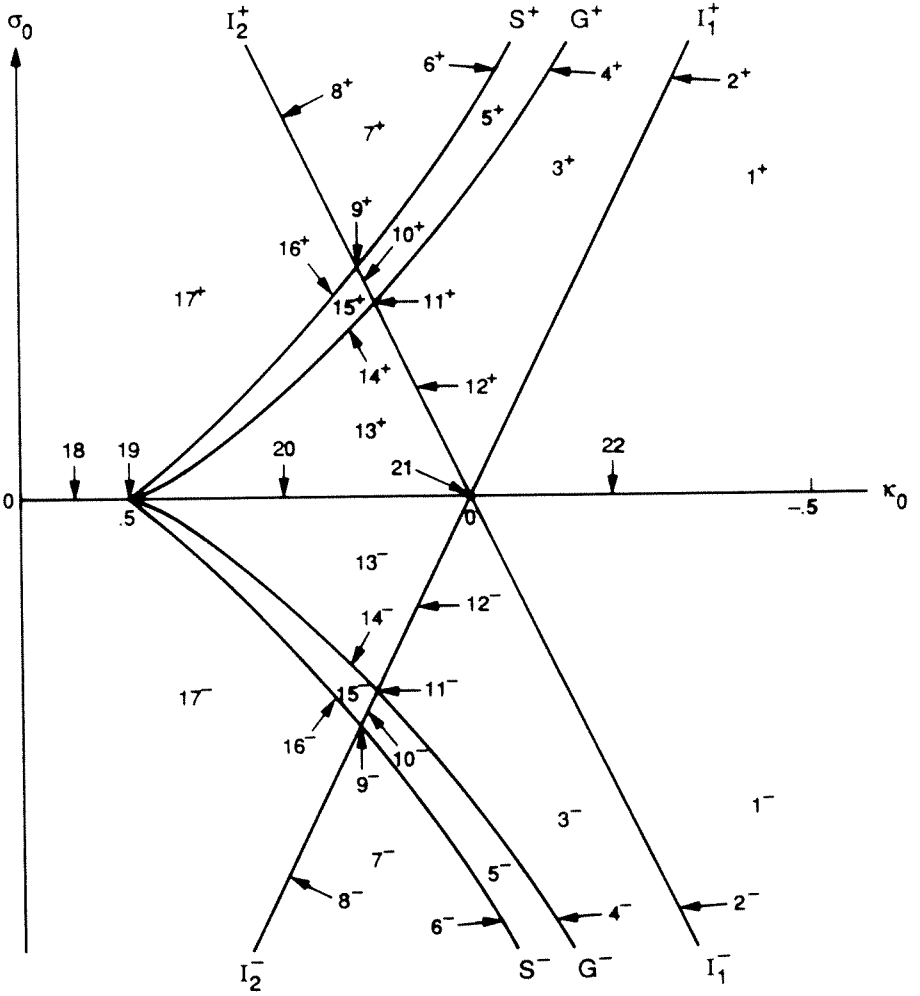


Figure 3.5 Bifurcation diagram in κ_0, σ_0 space

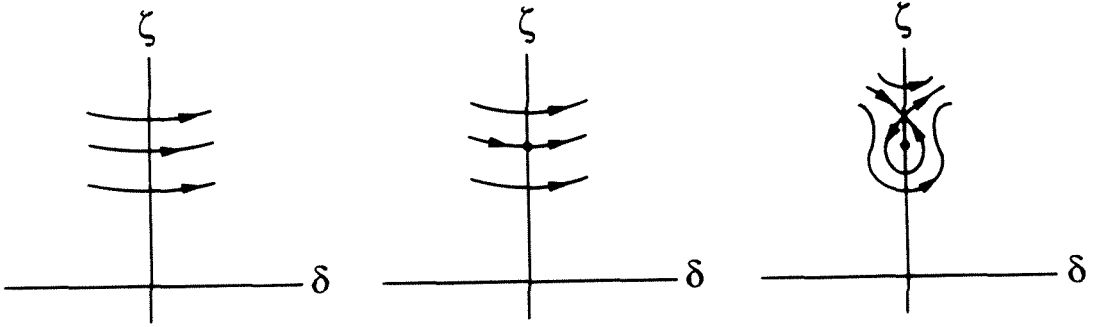


Figure 3.6 Saddle-node bifurcation across S^+ above I_2^+

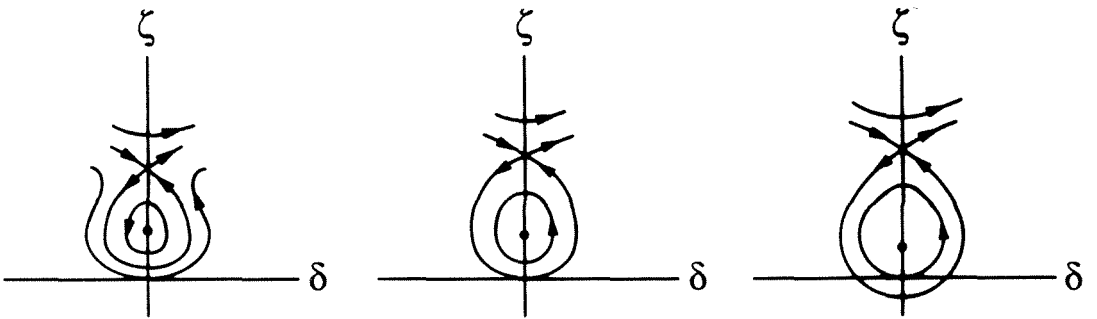


Figure 3.7 Global bifurcation across G^+

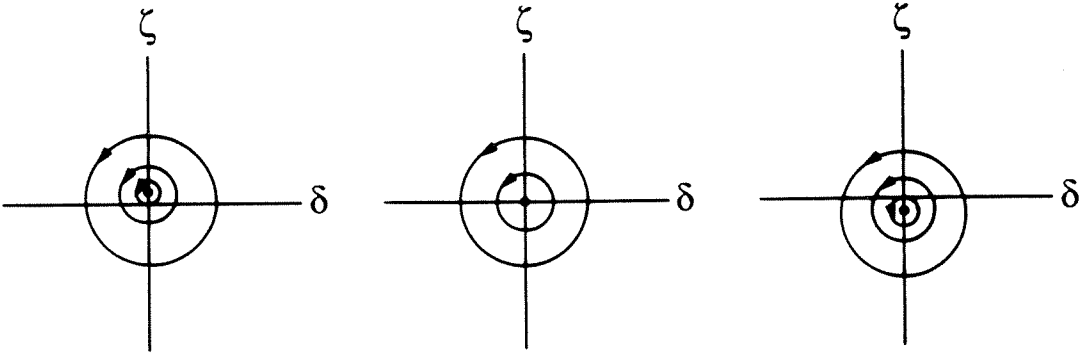


Figure 3.8 Bifurcation at the origin regarding q_e^+ across U^+

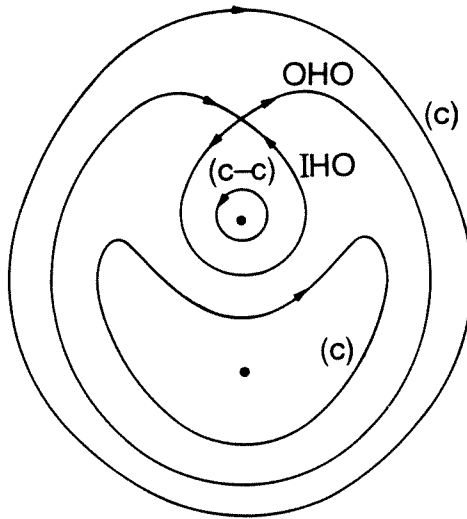


Figure 3.9 Bifurcation at $I = \infty$ on $\varphi = 3\pi/2$ across I_2^+ below S^+

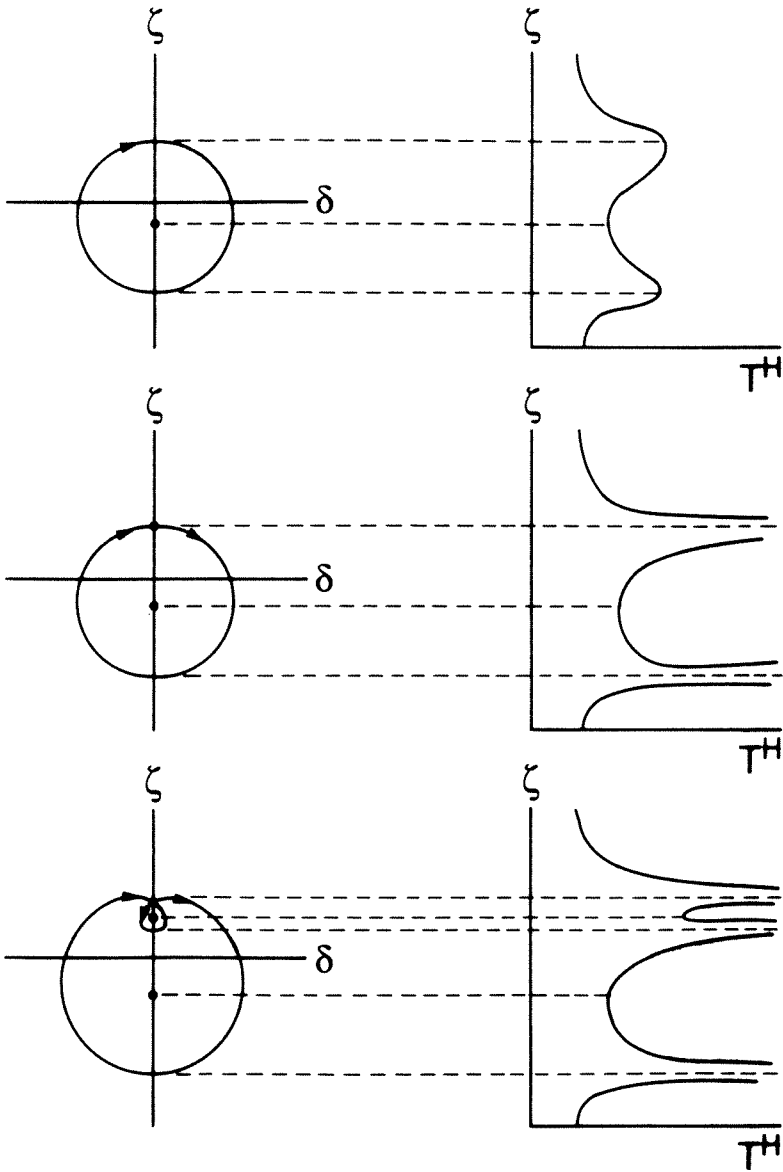


Figure 3.10 Saddle-node bifurcation on S^+ below I_2^+

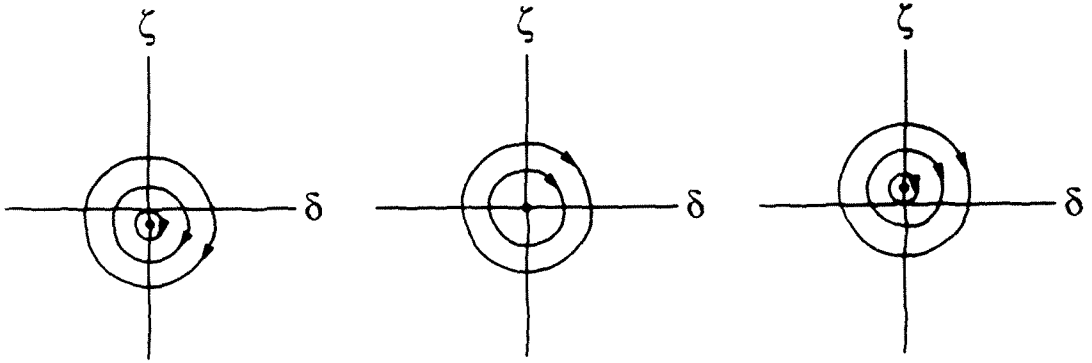


Figure 3.11 Bifurcation at the origin regarding q_e^+ across U^-

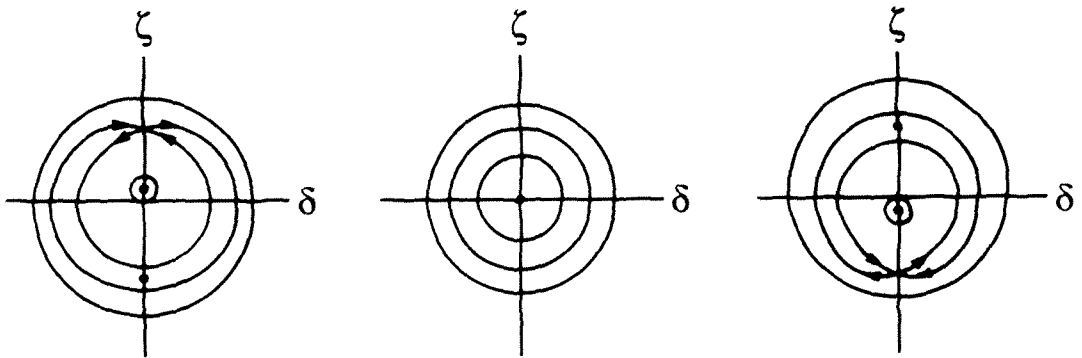


Figure 3.12 Ring bifurcation across R


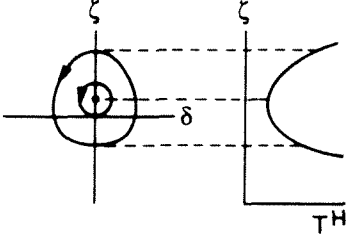
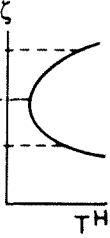
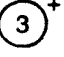
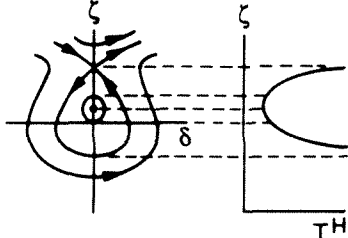
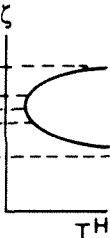

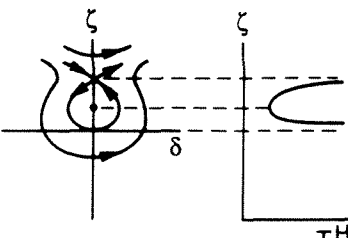
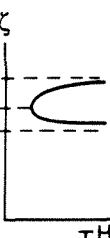

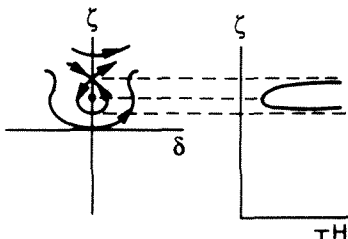
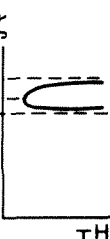

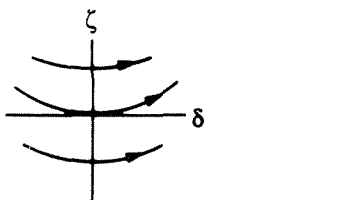
Region in (κ_0, σ_0)	The δ - ζ phase space	Corresponding period on ζ -axis	Possible solution
			q_e^+ (c-c) periodic orbits
			q_e^+ q_h (c-c) periodic orbits (c-c) periodic boundary orbit homoclinic boundary orbit unbounded orbits
			q_e^+ q_h (c-c) periodic orbits homoclinic boundary orbit unbounded orbits
			q_e^+ q_h (c-c) periodic orbits homoclinic orbit unbounded orbits
			unbound'

Figure 3.13 Possible UEV motion

<p>(13)⁺</p>		<p>q_e^+, q^- q_h (c-c) periodic orbits (c-c) boundary orbit IHO, OHO (c) periodic orbits</p>
<p>(14)⁺</p>		<p>q_e^+, q^- q_h (c-c) periodic orbits IHO, OHO (c) periodic orbits</p>
<p>(15)⁺</p>		<p>q_e^+, q^- q_h (c-c) periodic orbits IHO, OHO (c) periodic orbits (c) periodic boundary orbit</p>
<p>(17)⁺</p>		<p>q_e^- (c) periodic orbits (c) periodic boundary orbit</p>

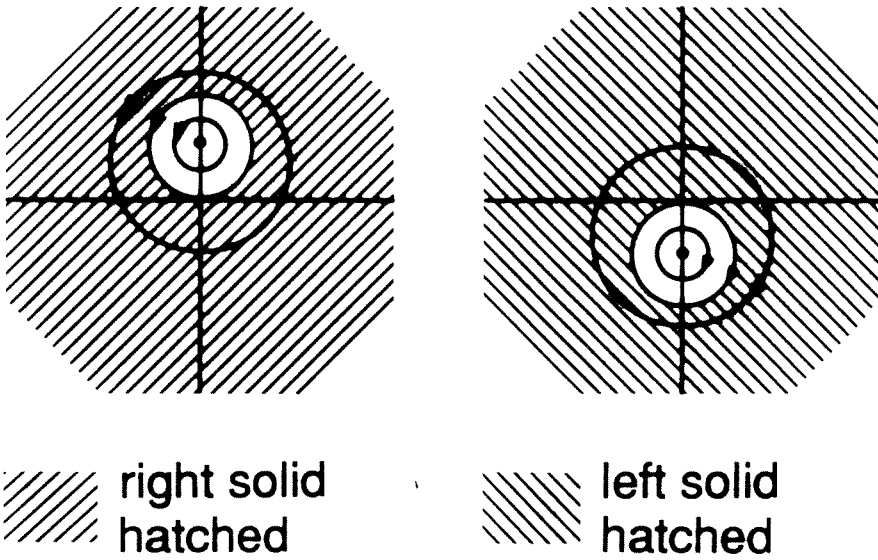


Figure 3.14 UEV periodic motion

(a) counterclockwise motion (b) clockwise motion

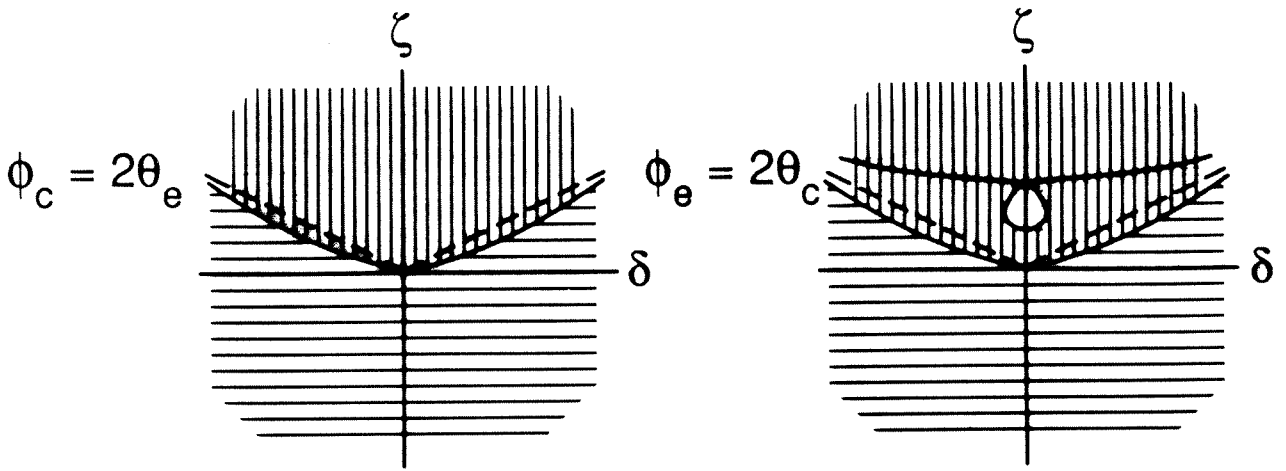


Figure 3.15 Unbounded orbit

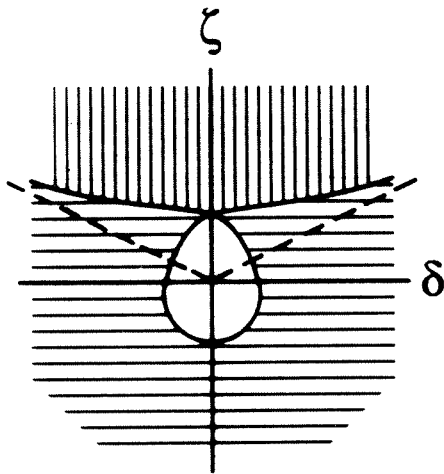
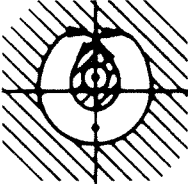
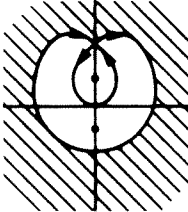
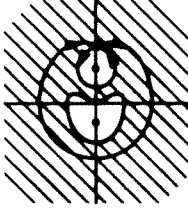
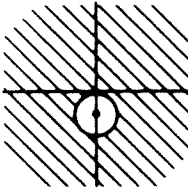


Figure 3.16 irreversible elongation

Region in (κ_0, σ_0)	The δ - ζ phase space	Possible UEV motion	Boundary orbit
①		<p>stable steady motion $(\theta_0 = \pi/4)$ (c-c) OSC. ($\theta_0^{(c-c)} = \pi/4$) (c-c) C.P.M. (c-c) rotation</p>	(c-c) PBO
③		<p>stable steady motion $(\theta_0 = \pi/4)$ unstable steady motion (c-c) OSC. ($\theta_0^{(c-c)} = \pi/4$) (c-c) C.P.M. (c-c) rotation (c-c) elongation (c) elongation</p>	(c-c) PBO IHO UBO
④		<p>stable steady motion $(\theta_0^{(c-c)} = \pi/4)$ unstable steady motion (c-c) OSC. ($\theta_0^{(c-c)} = \pi/4$) (c-c) elongation (c) elongation</p>	IHO UBO
⑤		<p>stable steady motion $(\theta_0^{(c-c)} = \pi/4)$ unstable steady motion (c-c) OSC. ($\theta_0^{(c-c)} = \pi/4$) (c-c) elongation (c) elongation</p>	IHO UBO
⑦		<p>(c-c) elongation (c) elongation</p>	UBO

Figure 3.17 Possible UEV motion

<p>(13)</p>		<p>stable steady motion $(\theta_0 = \pi/4 \text{ and } \theta_0 = 3\pi/4)$ unstable steady motion (c-c) OSC. $(\theta_0^{(c-c)} = \pi/4)$ (c-c) C.P.M. (c-c) rotation (c-c) H.B.M. (c) OSC. $(\theta_0^{(c)} = 3\pi/4)$ (c) H.B.M. (c) rotation</p>	<p>(c-c) PBO IHO OBO</p>
<p>(14)</p>		<p>stable steady motion $(\theta_0 = \pi/4 \text{ and } \theta_0 = 3\pi/4)$ unstable steady motion (c-c) OSC. $(\theta_0^{(c-c)} = \pi/4)$ (c-c) H.B.M. (c) OSC. $(\theta_0^{(c)} = 3\pi/4)$ (c) H.B.M. (c) rotation</p>	<p>IHO OBO</p>
<p>(15)</p>		<p>stable steady motion $(\theta_0 = \pi/4 \text{ and } \theta_0 = 3\pi/4)$ unstable steady motion (c-c) OSC. $(\theta_0^{(c-c)} = \pi/4)$ (c-c) H.B.M. (c) OSC. $(\theta_0^{(c)} = 3\pi/4)$ (c) C.P.M. (c) rotation (c) H.B.M.</p>	<p>IHO OBO (c) PBO</p>
<p>(17)</p>		<p>stable steady notion $(\theta_0 = 3\pi/4)$ (c) OSC. $(\theta_0^{(c)} = 3\pi/4)$ (c) P.P.M. (c) rotation</p>	<p>(c) PBO</p>

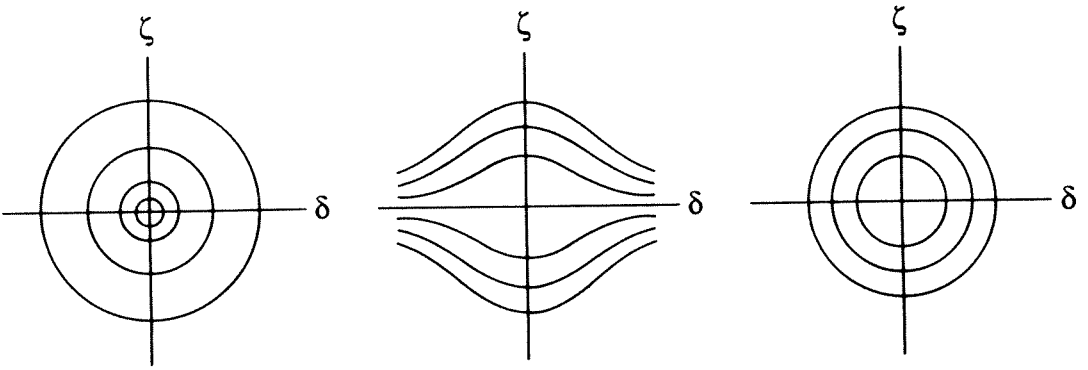


Figure 3.18 Level curves of excess kinetic energies
(a) H_E (b) H_S (c) H_R

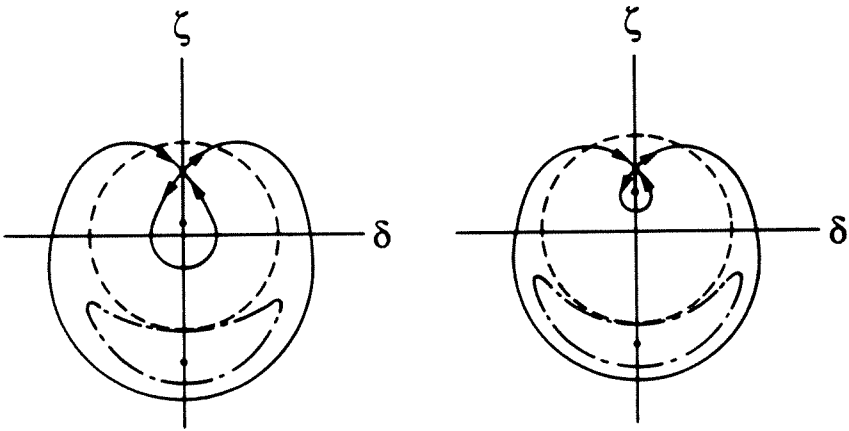


Figure 3.19 Geometrical relation between I_0 and orbits

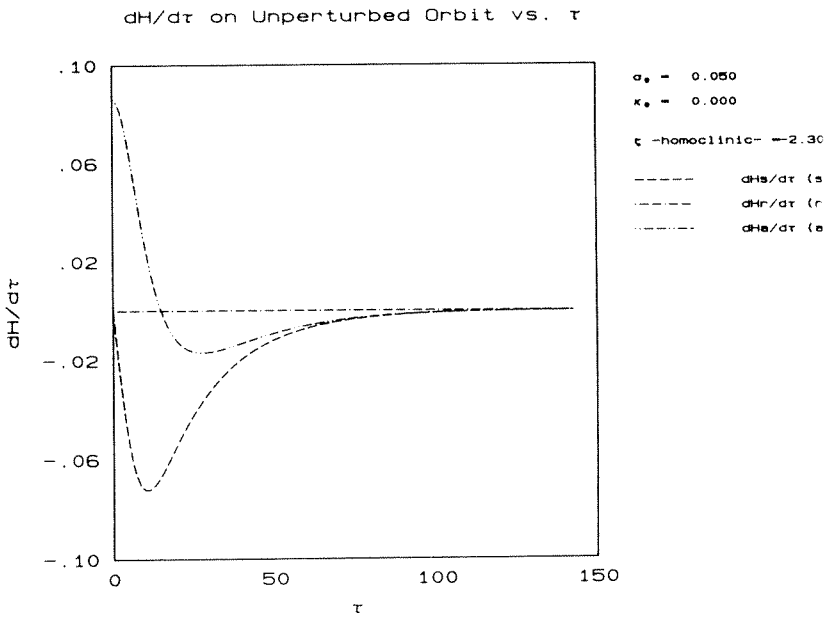
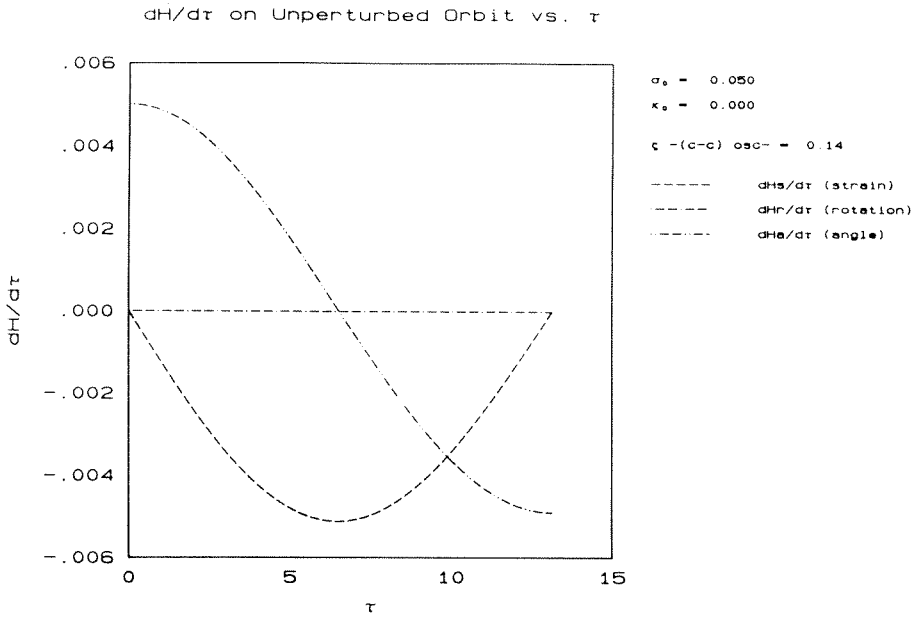
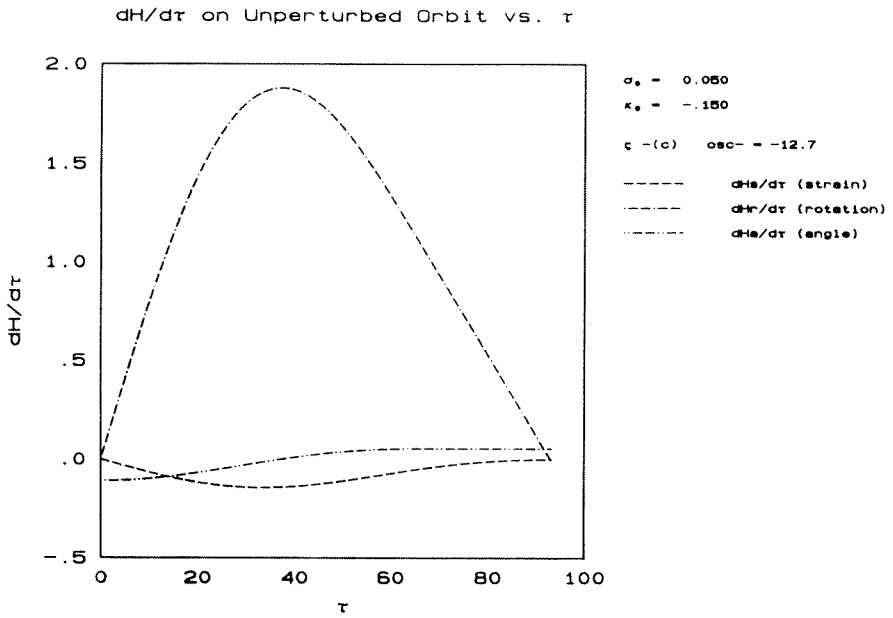


Figure 3.20 Rate of change in H_E , H_s and H_R on some unperturbed orbits
 a) (c-c) periodic orbit b) IHO c) (c) periodic orbit



on (c) periodic orbit

Orbit in the $\delta - \sigma$ phase space		UEV motion	corresponding region in (κ_0, σ_0)
fixed points	q_e^+	stable steady motion ($\theta_0 = \frac{\pi}{4}$)	1, 3, 5, 13, 14, 15
	q_e^-	stable steady motion ($\theta_0 = \frac{3\pi}{4}$)	13, 14, 15, 17
	q_h	unstable steady motion ($\theta_0 = \frac{\pi}{4}$)	3, 4, 5, 13, 14, 15
periodic		(C-C) oscillation ($\theta_0^{(C-C)} = \frac{\pi}{4}$)	1, 3, 4, 5, 13, 14, 15
		(C-C) rotation	3, 13
orbits (C-C) pbo (C-C) critical periodic motion 3, 13
 (C-C) pbo (C) oscillation ($\theta_0^{(C-C)} = \frac{\pi}{4}$) 13, 14, 15, 17
 (C-C) pbo (C) rotation 13, 14, 15, 17
 (C-C) pbo (C-C) critical periodic motion 3, 13
homoclinic orbits	iho	(C-C) homoclinic boundary motion	3, 4, 5, 13, 14, 15
	oho	(C) homoclinic boundary motion	13, 14, 15
unbounded orbits	ubo	irreversible contraction and elongation	3, 4, 5, 7
 (C-C) elongation and (C) elongation 3, 4, 5, 7

Table 3.1 Regular UEV motions in steady external flow field for (κ_0, σ_0) and thier corresponding orbits

Chapter 4

UEV DYNAMICS IN AN UNSTEADY EXTERNAL LINEAR FLOW FIELD

We study UEV dynamics in an external linear flow field which is slightly perturbed in a time periodic manner. The UEV dynamics drastically changes under the perturbation and a few types of new motion become possible. Our analysis will consist of the following four steps, 1) describe a mathematical method, the Poincaré map technique, which is useful for studying systems of two-dimensional nonautonomous O.D.E.'s with periodic dependence in time (the perturbed system), 2) examine Eqns. (2.9) and (2.10) with small time periodic perturbation in the parameters using the Poincaré map technique together with dynamical systems ideas so as to obtain all the possible solution types (qualitative analysis), 3) interpret those solutions in terms of UEV dynamics (i.e., possible motions for UEV), and 4) use an additional mathematical method, the Melnikov function technique, to give some quantitative analysis in relation to the perturbation types and perturbation frequency effects.

4.1 The Poincaré map technique

Recall that the solutions to Eqns. (2.9) and (2.10) for a given constant parameter value (κ_0, σ_0) ($\alpha_0 = 0$ w.l.o.g.) can be represented by invariant curves in the $\delta - \zeta$ phase plane, i.e., a level set of the Hamiltonian function. However, when the system is perturbed periodically in time, the dimension of the system is effectively increased by one, with the result that a level set of the Hamiltonian function in the $\delta - \zeta$ phase space at some specific time $\bar{\tau}$ may not give any useful information concerning the dynamics, and following the solutions with respect to all the initial conditions for all time is hardly possible. To conquer the difficulties, we use the Poincaré map technique. This technique offers some advantages in the study

of two-dimensional nonautonomous O.D.E.'s with periodic dependence in time. In particular, numerically or analytically computed global structure of the orbits, for example invariant manifolds associated with a fixed point, gives insightful display of dynamics. As we will see later, the Poincaré map technique together with other dynamical systems theories enables us to abstract much information for the understanding of the dynamics. Now let us briefly describe the construction of a Poincaré map. Eqn. (2.9) with time periodic perturbation in its parameter can be represented in the following form

$$\begin{aligned} \frac{dq}{d\tau} &= f(q) + \epsilon g(q, \tau; \Omega) \\ q &= (\delta, \zeta) \in \mathbf{R}^2 . \end{aligned} \tag{4.1}$$

where g is time periodic with period $T = 2\pi/\Omega$, i.e., for any q and τ , $g(q, \tau) = g(q, \tau + 2\pi/\Omega)$. By defining a new function $\mu(\tau)$

$$\mu(\tau) = \Omega\tau \pmod{2\pi} \in (0, 2\pi] ,$$

we can rewrite Eqn. (4.1) as a three dimensional autonomous O.D.E.'s

$$\begin{aligned} \frac{dq}{d\tau} &= f(q) + \epsilon g(q, \frac{\mu}{\Omega}; \Omega) \\ \frac{d\mu}{d\tau} &= \Omega . \end{aligned} \tag{4.2}$$

A two dimensional cross section of three dimensional space of Eqn. (4.2) is given by

$$\Sigma^{\bar{\mu}} = \{ (\delta, \zeta, \mu) | \mu = \bar{\mu} \in (0, 2\pi] \} .$$

The Poincaré map $P^{\bar{\mu}}$ of $\Sigma^{\bar{\mu}}$ to $\Sigma^{\bar{\mu}}$ is defined as

$$\begin{aligned} P^{\bar{\mu}} &: \Sigma^{\bar{\mu}} &\mapsto &\Sigma^{\bar{\mu}} \\ \left(\delta\left(\frac{\bar{\mu}}{\Omega}\right), \zeta\left(\frac{\bar{\mu}}{\Omega}\right) \right) &&\mapsto &\left(\delta\left(\frac{\bar{\mu} + 2\pi}{\Omega}\right), \zeta\left(\frac{\bar{\mu} + 2\pi}{\Omega}\right) \right) , \end{aligned}$$

where the dimension of the phase space of Eqn. (4.2) is reduced by one. The Poincaré map associated with a two dimensional time periodic Hamiltonian system has the following properties: 1) any two cross section $\Sigma^{\bar{\mu}_1}$ and $\Sigma^{\bar{\mu}_2}$ of $\bar{\mu}_1, \bar{\mu}_2 \in (0, 2\pi]$ have topologically equivalent structure which is referred to as variation of cross section. Hence from now on we eliminate the superscript $\bar{\mu}$ for convenience 2) it preserves orientation, and 3) it preserves area. See Wiggins [1988] for more details.

Before embarking on the study of the perturbed phase space structure, we go back to the unperturbed system and examine the behavior of some typical orbits in the Poincaré map with return time $T = 2\pi/\Omega$. It is clear that an orbit in the Poincaré map follows the invariant curve defined by a level set of the Hamiltonian function. However, the orbit is now a collection of points instead of a continuous curve. For example, a homoclinic orbit follows $W^u(q_h)$ and $W^s(q_h)$ of q_h and approaches q_h under positive and negative iteration. Dynamics along invariant circles corresponding to periodic orbits of O.D.E.'s may be classified into two types in the Poincaré map depending on the rotation number ρ which is a ratio of the period T^H of the corresponding periodic orbit of the O.D.E.'s and the Poincaré return time $T = 2\pi/\Omega$, i.e., $\rho = T^H/T$ (see Arnold and Avez [1968]).

- a. $\rho = \frac{m}{n} = \text{rational}$, i.e., m and n are relatively prime integers : During m iterates of the Poincaré map, every orbit on the invariant circle makes n complete revolutions along the circle and returns to its original position. In other words, every point on the circle is a period m point.
- b. $\rho = \text{irrational}$: Any orbit on the invariant circle never comes back to its original position in the Poincaré map, i.e., the orbit is dense along the circle.

4.2 Some typical orbits of the perturbed system in the Poincaré map

We are concerned with how unperturbed structures of some typical orbits which we saw in the previous chapter break down under small time periodic perturbation and provide mechanisms for new classes of dynamics. These include, 1) breaking-up of the invariant manifolds of a hyperbolic fixed point which provides mechanisms for chaos and transition dynamics, and 2) irregular and quasiperiodic motion associated with the breaking up or persistence of the invariant circles of the unperturbed system. We mean by the transition dynamics that the UEV changes its type of motion (for example (c-c) oscillation to (c-c) elongation) which occurs when the corresponding orbit crosses the boundary between two regions describing different types of the UEV motion. Furthermore, we say the UEV motion is

chaotic when the following conditions hold, 1) slight difference in its initial configuration results in totally different types of the UEV motion 2) the period of the UEV periodic motion can be arbitrarily long, and 3) there exist infinitely many initial UEV configurations which satisfy the previous two conditions. (see Devaney [1988] for the definition of the chaotic invariant cantor set). We will discuss transition dynamics and chaotic UEV motion in detail later. In this section, we take a geometrical approach together with some analytical techniques, i.e., the Melnikov functions (Melnikov [1963]). They provide us physical and insightful information for understanding of the perturbed dynamics.

4.2.1. Homoclinic tangle

Here we geometrically show how unperturbed structure along a homoclinic orbit breaks up and forms a so-called homoclinic tangle which provides a mechanism for complicated dynamics, such as transition dynamics and chaos. Since the purpose of this research is to understand UEV dynamics in the time periodic external linear flow field, we study two cases corresponding to unperturbed phase structures of the UEV motion, i.e., case 1: there exists only one homoclinic orbit (the phase structure is similar to the one corresponding to UEV motion for a parameter value given in 3^+ , 4^+ and 5^+ of the bifurcation diagram (Fig. 3.5), and case 2: there exist two homoclinic orbits with one encircling the other (the phase structure of UEV motion for a parameter value set given in 13^+ , 14^+ and 15^+). For both cases, we first describe generic dynamics regarding the breaking up of the homoclinic orbit(s) and then interpret the UEV motion in time periodic unsteady external linear flow field for corresponding parameter value (κ_0, σ_0) .

case 1

In the Poincaré map, $W^s(q_h)$ and $W^u(q_h)$ persist, but may break up and intersect transversely (see Frenichel[1971] and Hirsch et.al.[1977]). Because of the invariance of the manifolds, the iterations under the Poincaré map result in a structure referred to as the homoclinic tangle as shown in Fig. 4.1. Whether or not $W^s(q_h)$ and $W^u(q_h)$ intersect transversely is determined analytically by the Melnikov technique which detects the transverse intersections in the following manner.

The first order term, up to a known normalization factor, of the Taylor expansion of the ‘signed’ distance $d(\tau_0, \epsilon)$ from $W^u(q_h)$ to $W^s(q_h)$ along the unperturbed homoclinic orbit $q_h(\tau)$ is given by

$$d(\tau_0, \epsilon) = \epsilon \frac{M(\tau_0)}{\|f(q_h(-\tau_0))\|} + O(\epsilon^2) ,$$

where

$$M(\tau_0) = \int_{-\infty}^{\infty} (f \wedge g)(q_h(\tau), \tau + \tau_0) d\tau .$$

f and g are given in Eqn. (4.1), τ_0 is a parameterization variable along $q_h(\tau)$, \wedge denotes the usual wedge product and $M(\tau_0)$ is called the Melnikov function. The Melnikov theorem states that a simple zero of $M(\tau_0)$ (i.e., $M(\tau_0) = 0$, $\frac{\partial}{\partial \tau_0} M(\tau_0) \neq 0$) implies the transverse intersection of $W^u(q_h)$ and $W^s(q_h)$. Furthermore, if all the intersection are transverse, then $M(\tau_0)$ has an even number of simple zeroes per perturbation period, i.e., for $\tau_0 \in (0, \frac{2\pi}{\Omega}]$. The geometrical explanation of the Melnikov function is shown in Fig. 4.1. As we will see later, the Melnikov function provides not only the geometrical meaning but also some physical consequences of the perturbation.

< Transition dynamics >

In order to study the transition dynamics, i.e., how an orbit crosses the boundary between two distinct regions, we first describe so-called transport dynamics. See Rom-Kedar et.al. [1989] and Rom-Kedar and Wiggins [1989] for more details. The relation of transport dynamics and transition dynamics through the homoclinic tangle is as follows. The transport dynamics through the homoclinic tangle involves not only a single orbit but also all orbits which belong to a part of one of the two distinct regions. The region which crosses the boundary is defined by segments of $W^u(q_h)$ and $W^s(q_h)$ which form the homoclinic tangle as we will see in detail later. We call this region a lobe. The transition dynamics associated with the transport dynamics concerns how an orbit which belongs to a lobe crosses the boundary between two distinct regions. Hence describing the transport dynamics through the homoclinic tangle is, in a sense, equivalent to describing the transition dynamics through the homoclinic tangle.

Now we examine how the dynamics associated with the homoclinic tangle plays a significant role in the transport between two regions separated by the segments of $W^u(q_h)$ and $W^s(q_h)$. To demonstrate the transport dynamics, we begin with some definitions.

Definition 4.1. Consider a point $p \in W^s(q_h) \cap W^u(q_h)$ and let $q_h p^u$ ($q_h p^s$ resp.) denote the segment of $W^u(q_h)$ ($W^s(q_h)$ resp.) from q_h to p on $W^u(q_h)$ ($W^s(q_h)$ resp.). Then p is called a primary intersection point (pip) if $q_h p^u$ and $q_h p^s$ intersect only in p as shown in Fig. 4.1.

Definition 4.2. Let p_1 and p_2 be two adjacent pip's. We refer to the region bounded by the segments of $W^u(q_h)$ and $W^s(q_h)$ which connect p_1 and p_2 as a lobe L as shown in Fig. 4.1.

The area of the lobe $\mu(L)$ is computed using the Melnikov function

$$\mu(L) = \epsilon \int_{\tau_1}^{\tau_2} M(\tau_0) d\tau_0 + O(\epsilon^2) ,$$

where τ_1 and τ_2 are parameterization variables corresponding p_1 and p_2 respectively. Now let p_0 be a pip which defines a region bounded by $q_h p_0^u \cup q_h p_0^s$ nearest to the unperturbed homoclinic orbit as shown in Fig. 4.2. We refer to this region as A . We want to describe the mechanism of the transport dynamics across the boundary ∂AB of A . Note that the regions C is separated from other regions by $W^s(q_h)$ and $W^u(q_h)$ which do not intersect any other manifolds. Because of the invariance of the manifolds, no orbit can across the boundary ∂BC (i.e., no transition).

Definition 4.3. A lobe is called an exterior lobe, if no part of the lobe is contained in A . A lobe is called an interior lobe if it is not an exterior lobe.

Furthermore, we make some ordering of the lobes as shown in Fig. 4.3 so that the following relation holds

$$\begin{aligned} P(E_i) &= E_{i+n} \\ P(D_i) &= D_{i+n} , \end{aligned}$$

where E_j ($j \leq 1$) and D_j ($j \leq 1$) are exterior lobes, E_k ($k > 1$) and D_k ($k > 1$) are interior lobes and n corresponds to the number $2n$ of the simple zeroes of $M(\tau_0)$

per perturbation period. The transport mechanism is completely governed by the lobe dynamics in the following way: 1. after one cycle of the perturbation (one iterate of the map) E_0, \dots, E_{-n+1} enter region A . Similarly, D_0, \dots, D_{-n+1} leave region A , and 2. the lobes maintain their orderings which results in complete order in the transport dynamics. Recall that the number, n , of the lobes per cycle is related to the number, $2n$, of transverse intersection of $W^u(q_h)$ and $W^s(q_h)$ per cycle, and hence it is also related to the number, $2n$, of the simple zeros of $M(\tau_0)$. One of the significant consequences of the transport mechanism governed by the lobe dynamics is that one can precisely predict how long it takes for a point to cross the boundary ∂A of A depending on which lobes contain that point. Another significant consequence is that one can compute “the resident time distribution” i.e., how long the points in E_1 can stay in A which is determined by how images of E_1 under the Poincaré maps intersect with D_1, \dots, D_n as shown in Fig. 4.3. For more detailed discussion concerning the transport dynamics, see Rom-Kedar et. al. [1988]. As we mentioned earlier, the transition dynamics can be understood as how an orbit crosses the boundary ∂AB associated with the transport dynamics.

The corresponding UEV dynamics for various (κ_0, σ_0) is the following. For (κ_0, σ_0) in 3^+ in a steady external linear flow field, the homoclinic orbit defines the boundary of (c-c) rotation and (c-c) elongation. Hence in the time periodic external linear flow field, the UEV may change its type of motion between (c-c) rotation and (c-c) elongation. The lobe dynamics enables us to compute the residence time (i.e., how long the UEV can undergo (c-c) rotation before it changes its type of motion to (c-c) elongation). Once the UEV changes its motion from (c-c) rotation to (c-c) elongation, then it can never change its type of motion to (c-c) rotation. For (κ_0, σ_0) in 5^+ , the same argument for 3^+ holds, but (c-c) rotation is replaced by (c-c) oscillation. For (κ_0, σ_0) near 4^+ , the homoclinic tangle may contain the origin of the coordinate system. This means that the argument for 3^+ holds, but (c-c) rotation is replaced by (c-c) rotation and (c-c) oscillation. Note that the transition between (c-c) rotation and (c-c) oscillation can occur an arbitrary number of times because the corresponding regions for both types of motion lies in the same side of the boundary defined by parts of $W^u(q_h)$ and $W^s(q_h)$.

< Chaos >

Now let us describe another important dynamics associated with the homoclinic tangle, i.e., chaotic dynamics. The so-called horseshoe map associated with the homoclinic tangle provides a complicated dynamics which we will briefly demonstrate now. See Wiggins [1988], Guckenheimer and Holmes[1983], Greenspan and Holmes [1984], Holmes [1984] and Holmes and Marseden[1984]. In doing so, we assume $n = 1$ for convenience, i.e., only $n = 1$ lobe enters A across ∂AB per cycle. For $n > 1$, the mechanism is the same as the case for $n = 1$.

Consider a region denoted by V as shown in Fig. 4.6. After four iterates of the Poincaré map, $P^5(B)$ returns onto itself as a horseshoe shaped domain having been stretched and folded as demonstrated in Fig. 4.6. It can be shown, see Wiggins [1988], that V contains an invariant Cantor set Λ such that $P^m|_{\Lambda}$, for some $m \geq 4$, 1) a countable infinity of unstable periodic orbits of all possible periods, 2) an infinity of unstable nonperiodic orbits, and 3) two points initially close together eventually end up in completely different positions. Λ is called a chaotic invariant Cantor set for P^m associated with the horseshoe map. Note that V is contained in A and hence the chaotic dynamics exists only in the interior of A .

We make one more definition.

Definition 4.3. We call a region which contains the homoclinic tangle and provides the mechanism for transition dynamics and chaotic dynamics as the chaotic transition region.

Note that the size of the chaotic transition region is closely related to the size of a lobe, and hence the Melnikov function $M(\tau_0)$ defines the size of the chaotic transition region.

In terms of the UEV motion, the chaotic Cantor set along the horseshoe map means the following, 1) slight difference in its initial configuration results in totally different type of the UEV motion, 2) the period of the UEV periodic motion can be arbitrarily long, and 3) there exist infinitely many initial UEV configurations which satisfy the previous two conditions. For (κ_0, σ_0) in 3^+ , the UEV may undergo chaotic (c-c) rotation. For (κ_0, σ_0) in 5^+ , the UEV may undergo chaotic (c-c)

oscillation. For (κ_0, σ_0) near 4^+ , the UEV may undergo chaotic motion between (c-c) rotation and (c-c) oscillation.

case 2

When two homoclinic orbits break up under the time periodic perturbation, the resulting homoclinic tangle structure may look as shown in Fig. 4.5. The tangles of inner and outer homoclinic orbits generically intersect and wrap around themselves. The dynamics along the tangles are again governed by those tangles which provide the transport between three regions as shown in Fig. 4.5 and the chaotic dynamics. The mechanisms of the transport and chaotic dynamics are basically the same as the ones for case 1, however, they are more complicated. For example, we need careful consideration whether or not some lobe may come back onto itself after some iterates of the Poincaré map because it effects the transport dynamics. The chaotic region can exist on both side of the boundaries along the heteroclinic tangles in case 2.

< Transition dynamics and chaotic motion >

The corresponding UEV dynamics for various (κ_0, σ_0) is the following. For (κ_0, σ_0) in 13^+ in the steady external linear flow field, two homoclinic orbits define the boundaries of (c-c) rotation, (c) oscillation and (c) rotation. Hence in the time periodic external linear flow field, the UEV may change its types of motion between (c-c) rotation, (c) oscillation and (c) rotation. The lobe dynamics enables us to compute the residence time (i.e., how long the UEV can stay in the same type of motion before it changes type of motion to the other). Note that the UEV can change its type of motion arbitrary times because there exist two homoclinic tangles intersecting each other. Furthermore, the chaotic periodic motion of UEV exists for (c-c) rotation, (c) oscillation and (c) rotation along two homoclinic tangles. For (κ_0, σ_0) in 15^+ , the same argument for 13^+ holds, but (c-c) rotation is replaced by (c-c) oscillation, and (c) oscillation and (c) rotation are replaced by two kinds of (c) rotation. For (κ_0, σ_0) near 14^+ , the homoclinic tangle may contain the origin of the coordinate system. This means that the argument for 3^+ holds, but (c-c) rotation is replaced by (c-c) rotation and (c-c) oscillation.

4.2.2 Breaking-up of the invariant circles of the unperturbed system

In this section, we study how the unperturbed dynamics along the invariant circles may be destroyed under time periodic perturbation. This corresponds to irregular oscillation or rotation of the UEV. Recall that, qualitatively speaking, dynamics on an unperturbed invariant circle in the Poincaré map depends on whether or not its rotation number ρ is rational, where ρ is a ratio of the return time of the Poincaré map $2\pi/\Omega$ and the period of the corresponding invariant circle of natural frequency Ω^H . In the perturbed system, again the rotation number ρ of the corresponding unperturbed system plays an important role in determining the qualitative dynamics of the orbit, although the dynamics itself may exhibit completely different behavior from the unperturbed dynamics. We discuss the possible dynamics and their mechanisms to see how the unperturbed invariant circles may be destroyed depending on ρ . Finally we describe the corresponding UEV motion.

4.2.2.1 Resonance band of order $\frac{m}{n}$

When the time periodic perturbation is imposed, the unperturbed invariant circle with a resonance relation $m\Omega^H = n\Omega$ may break up and leave $2m\ell$ period m points where ℓ is some integer and Ω is the perturbation frequency, Ω^H is the natural frequency of the unperturbed periodic orbit. Generically, of those $2m\ell$ period m points are $m\ell$ hyperbolic period m points and $m\ell$ elliptic period m points with alternating stability type along ϵ -close to the unperturbed invariant circle as is shown in Fig. 4.6 for $m = 3$, $n = 1$ and $\ell = 1$. The stable and unstable invariant manifolds of hyperbolic period m points intersect transversely and form heteroclinic tangles while surrounding their neighboring elliptic period m points. This results in a chain-like structure, the so-called resonance band of order $\frac{m}{n}$ (henceforth RB $\frac{m}{n}$). Clearly, the dynamics along a resonance band is governed by these heteroclinic tangles through the same mechanism as we described for the homoclinic tangle, i.e., the lobe dynamics determines the process of passage through the resonance band, and also the horseshoe maps associated with the heteroclinic tangles provides chaotic dynamics along the band. If the orbit corresponding to the UEV motion is contained in RB $\frac{m}{n}$, then the UEV oscillates (or rotates) with fairly large

fluctuation amplitude from its original unperturbed motion. The UEV motion can also be chaotic if the corresponding orbit lies in the chaotic Cantor set associated with the horseshoe map along the heteroclinic tangles.

An analytical technique, the Melnikov function $M^{\frac{m}{n}}(\tau_0)$ on RB $\frac{m}{n}$, tells us the conditions for the existence of period m points which is equivalent to the existence of the resonance band itself. $M^{\frac{m}{n}}(\tau_0)$ can also provide more information regarding not only the possible dynamics along the band but also how the perturbation influences the motion as we will see later.

First we consider the orbits belonging to a one-parameter family, i.e., $\frac{\partial}{\partial H} T^H \neq 0$ on the unperturbed orbits. Let us define $M^{\frac{m}{n}}(\tau_0)$ as follows:

$$M^{\frac{m}{n}}(\tau_0) = \int_{-\frac{mT}{2}}^{\frac{mT}{2}} f \wedge g(q^{\frac{m}{n}}(\tau), \tau + \tau_0) d\tau ,$$

where $\tau_0 \in (-\frac{mT}{2}, \frac{mT}{2}]$ is the parametrization variable on the corresponding unperturbed orbit $q^{\frac{m}{n}}(\tau)$ and the integral is evaluated on $q^{\frac{m}{n}}(\tau)$. Then the Melnikov technique tells us that the simple zeroes of $M^{\frac{m}{n}}(\tau_0)$, (i.e., $M^{\frac{m}{n}}(\tau_0) = 0$, $\frac{\partial}{\partial \tau_0} M^{\frac{m}{n}}(\tau_0) \neq 0$) imply the period m points of RB $\frac{m}{n}$ with alternating stability type between elliptic and hyperbolic.

Besides the existence of RB $\frac{m}{n}$, the Melnikov function $M^{\frac{m}{n}}(\tau_0)$ also gives us more points of information. Among them, the following three are particularly useful, 1) it gives the width of RB $\frac{m}{n}$, 2) it gives the bifurcation condition of RB $\frac{m}{n}$, and 3) it tells us that, if some symmetry exists in the unperturbed phase space, then $M^{\frac{m}{n}}(\tau_0)$ may be identically zero for $n \neq 1$ which means that the ultraharmonics are hard to identify if the symmetry exists. We describe these three properties and interpret the UEV motion now.

- 1) As $M(\tau_0)$ on the homoclinic orbit relates to the distance between unstable and stable invariant manifolds, it can be shown that $M^{\frac{m}{n}}(\tau_0)$ on the resonance band relates to the width of the band $d^{\frac{m}{n}}(\tau_0, \epsilon)$ in the following manner. $M^{\frac{m}{n}}(\tau_0)$ is the first order term of the width of the band up to a known normalization factor.

$$d^{\frac{m}{n}}(\tau_0, \epsilon) = \epsilon \frac{M^{\frac{m}{n}}(\tau_0)}{\|f(q^{\frac{m}{n}}(-\tau_0))\|} + O(\epsilon^2).$$

It is clear that larger $d^{\frac{m}{n}}$ means larger fluctuation in the UEV configuration from the original motion. Using the width of RB $\frac{m}{n}$, we can compute the perturbation frequency range for the origin of the coordinate system, i.e., $(\delta, \zeta) = (0, 0)$, to be contained in RB $\frac{m}{n}$ up to the first order in ϵ . This is extremely important when we consider the transition dynamics of the UEV between oscillation and rotation in the same direction through RB $\frac{m}{n}$ as we will see later. (Recall that we distinguish the UEV oscillation from rotation depending on whether or not the corresponding orbit contains the origin of the coordinate system interior to itself.)

$$\Omega \in \left(\frac{m}{n} \Omega_0^H - \Delta \Omega^{\frac{m}{n}}, \frac{m}{n} \Omega_0^H + \Delta \Omega^{\frac{m}{n}} \right),$$

where

$$\Delta \Omega^{\frac{m}{n}} = \frac{1}{2} \frac{m}{n} \frac{\partial \Omega^H}{\partial \zeta} \Big|_{(\delta, \zeta) = (0, 0)} d_0^H(\tau_0) \Big|_{\tau_0 = \bar{\tau}_0}$$

with

$$d_0^H(\tau_0) = \epsilon \frac{M^{\frac{m}{n}}(\tau_0)}{\|f(q_0^H(-\tau_0))\|}.$$

The Melnikov function is evaluated on the unperturbed orbit going through the origin, denoted by $q_0^H(\tau)$, Ω_0^H is the natural frequency of the corresponding orbit, and $\bar{\tau}_0$ is the value of parametrization variable on the orbit at the origin (or on the ζ -axis).

- 2) The Melnikov function $M^{\frac{m}{n}}(\tau_0)$ also gives the condition for the bifurcation on RB $\frac{m}{n}$. We consider two types of bifurcations of RB $\frac{m}{n}$ which occur in the motion of the UEV as we will see later. First we consider a bifurcation that occurs when the Melnikov function is identically zero, i.e., $M^{\frac{m}{n}}(\tau_0) = 0$ for $\tau_0 \in (0, mT]$ and either one of the following conditions holds

$$\begin{aligned} \frac{\partial}{\partial \Omega} M^{\frac{m}{n}}(\tau_0) &\neq 0 \\ \frac{\partial}{\partial c} M^{\frac{m}{n}}(\tau_0) &\neq 0, \end{aligned}$$

where c is some parameter. The following dynamical consequences can be proven. If $\frac{\partial}{\partial \Omega} M^{\frac{m}{n}}(\tau_0) \neq 0$ ($\frac{\partial}{\partial c} M^{\frac{m}{n}}(\tau_0) \neq 0$ resp.), then, as Ω (c resp.) varies, the resonance band disappears once and reappears with the stability type of

the period m points exchanged as is demonstrated in Fig. 4.7 for $m = 3$, $n = 1$ and $\ell = 1$. We call this bifurcation the ring bifurcation. The consequence of this bifurcation is as follows. When a resonance band disappears, the passage through the resonance band and chaotic dynamics associated with the horseshoe map do not exist. As Ω (c resp.) varies, the band reappears although the stability types of the period m points have been exchanged. The meaning of this bifurcation in terms of the UEV motion is the following. When RB $\frac{m}{n}$ disappears, the corresponding UEV motion becomes regular. The UEV motion sensitively depend on the value of Ω (c resp.).

The other bifurcation, which occurs in the $\delta - \zeta$ phase space corresponding to the UEV motion, is a bifurcation corresponding to the non-twisting band (i.e., $\frac{\partial}{\partial H}\Omega^H = 0$) in the unperturbed phase space. (Recall that the non-twisting band may exist in the $\delta - \zeta$ phase space for (κ_0, σ_0) in 17^+ corresponding to the UEV motion, see Chapter 3.) We refer to Wiggins [1988] for the detail and only demonstrate the result of the bifurcation. Also see Van der Weele et. al. [1988] for more discussion for a special bifurcation. When the resonance relation $m\Omega^H = n\Omega$ is satisfied on the non-twisting band, a combination of local saddle-node bifurcation and global effect may end in the birth of twin RB $\frac{m}{n}$ on both side of the non-twisting band as shown in Fig. 4.8. For a given perturbation frequency, there exist two distinct RB $\frac{m}{n}$ next to each other. There exist two layers where the orbits fluctuate with the same frequency. Before the birth of the twin RB $\frac{m}{n}$, the corresponding UEV motion is regular. After the birth, there exist two layers of the UEV configuration for the UEV to undergo irregular oscillation or rotation.

- 3) We make the last remark on $M^{\frac{m}{n}}(\tau_0)$. It regards the symmetry in the unperturbed phase space. Let us assume that there exists some symmetry in the unperturbed phase structure as shown in Fig. 4.9. Symmetry type 1 as shown in Fig. 4.9a corresponds to the motion of the UEV for $\sigma_0 \neq 0$ and symmetry type 2 as shown in Fig. 4.9b corresponds to the motion of UEV for $\sigma_0 = 0$. Suppose the time periodic perturbation is imposed sinusoidally for reasons which

we will state later. For example, the perturbation in $\sigma(\tau)$ in Eqn. (2.12) is written

$$\sigma(\tau) = \sigma_0 + \sigma_0 \epsilon_\sigma \sin \Omega(\tau + \tau_\sigma)$$

where ϵ_σ is a perturbation amplitude and τ_σ describes the phase shift of the perturbation. Then the $M^{\frac{m}{n}}(\tau_0)$ generically has the following property for both types of perturbation.

$$M^{\frac{m}{n}}(\tau_0) \equiv 0 \quad \text{for } n \neq 1$$

See Appendix 3 for proof. It can also be shown (Appendix 3) that Symmetry type 2 may have furthermore property as follows depending on how the perturbation is imposed.

$$M^{\frac{2k+1}{1}}(\tau_0) \equiv 0 \quad \text{or} \quad M^{\frac{2k}{1}}(\tau_0) \equiv 0$$

Recall that the $M^{\frac{m}{n}}(\tau_0)$ is related to the first order term of the width of the resonance band. Hence, if $M^{\frac{m}{n}}(\tau_0) \equiv 0$, then it does not necessarily follow that RB $\frac{m}{n}$ does not exist, i.e., it may exist, however the width is higher order. Hence we can conclude that the ultraharmonic resonance bands are hard to identify when the symmetry exists in the unperturbed structure. Furthermore, if the symmetry exists as is shown in Fig. 4.9, then some of the subharmonic resonance bands are hard to identify. It follows that, due to the symmetry in the UEV itself and the steady external linear flow field, the ultraharmonic motion of the UEV is very hard to identify.

4.2.2.2 KAM torus and cantorus

The perturbed dynamics along an invariant circle whose rotation number ρ is irrational is classified into two types depending on the degree of ‘irrationality’ of ρ .

KAM torus: When ρ is sufficiently poorly approximated by rational numbers, the invariant circle, called a KAM torus, survives under the perturbation. Orbit on a KAM torus is again dense in the phase space which implies that the motion

in a continuous time system can be viewed as quasiperiodic to the perturbation frequency. The KAM torus, which is an invariant circle, is extremely important because it prohibits any passage across itself.

cantorus : When ρ fails to satisfy the condition for KAM torus, the motion may still be quasiperiodic but orbits do not densely fill a circle, but rather a Cantor set. This structure has been called a cantorus since it geometrically appears as a circle with an infinite number of gaps.

If an orbit corresponding to the UEV motion lies in either KAM torus or cantorus, then the UEV motion is fairly regular with very small fluctuations from the original motion, but it is quasiperiodic to the perturbation frequency.

4.2.2.3 The global structure

We consider the resulting global structure of a one-parameter family invariant circles of case 1 as shown in Fig. 4.9a because it is the case for the UEV motion for $\sigma_0 \neq 0$. Suppose that the family is parametrized by $H \in (H_1, H_2)$, then the corresponding period T^H satisfies $T_{\min}^H < T^H < T_{\max}^H$ where $T_{\min}^H = \inf\{T^{H_1}, T^{H_2}\}$, $T_{\max}^H = \sup\{T^{H_1}, T^{H_2}\}$ and $\frac{\partial}{\partial H}T^H \neq 0$ for any $H \in (H_1, H_2)$. The corresponding natural frequency $\Omega^H = 2\pi/T^H$ ranges between $T^H \in (\Omega_{\min}^H, \Omega_{\max}^H) = (2\pi/T_{\max}^H, 2\pi/T_{\min}^H)$. If the family contains an elliptic fixed point q_e at its center, then $T_{\min}^H = T^{H(q_e)} = 2\pi/\Omega_e$ where Ω_e is the imaginary part of eigenvalues associated with the linearization of the vector field at q_e . Moreover, if the family is bounded by homoclinic orbits, then T_{\max}^H goes to infinity logarithmically, in other words Ω_{\min}^H goes to zero, due to the presence of the hyperbolic fixed point q_h .

Now we want to geometrically describe the resulting structure of the phase space in the Poincaré map and see how the perturbation frequency Ω influences the global dynamics. Since the dynamics on RB $\frac{m}{1}$, KAM torus and can torus are completely different, locating them globally in the phase space is very important for understanding of the global dynamics. For this purpose, we locate RB $\frac{m}{1}$ for all possible m first. Note that possible m 's depend on the perturbation frequency Ω and the natural frequency range $(\Omega_{\min}^H, \Omega_{\max}^H)$. For a given family, Ω plays an

important role for determining the global structure of the perturbed phase space as we will see later.

Since the global structures are completely different depending on whether or not the one-parameter family is bounded by homoclinic orbits, we consider two cases which are related to the UEV motion separately, i.e., 1) a family bounded by homoclinic orbits, meaning that $\Omega_{\min}^H = 0$. (this corresponds to the unsteady global structure of the UEV motion with (κ_0, σ_0) in 3^+ , 4^+ , 5^+ , 13^+ , 14^+ , and 15^+), and 2) a family not bounded by homoclinic orbits meaning that $\Omega_{\min}^H > 0$ (this corresponds to the unsteady global structure of the UEV motion with (κ_0, σ_0) in 1^+ and 17^+).

case 1: a family bounded by homoclinic orbits.

In Fig. 4.10, the curves are the graph of the position of the corresponding unperturbed orbit on ζ -axis with respect to the perturbation frequency Ω for several m 's of RB $\frac{m}{1}$. Note that the curve for $m = 1$ corresponds to the graph of the position of the unperturbed orbit with natural frequency $\Omega^H = \Omega$. Because the natural frequency is bounded as $\Omega \in (\Omega_{\min}^H, \Omega_{\max}^H)$, we can obtain the lowest order m_{\min} of the resonance band from the resonance relation $\Omega = m\Omega^H$ for a given Ω .

$$m_{\min} = \left\lceil \frac{\Omega}{\Omega_{\max}^H} \right\rceil + 1 .$$

For a fixed perturbation frequency Ω , the higher order resonance band approaches the homoclinic tangle (see Fig. 4.10). Eventually, the resonance bands of high enough order are absorbed in the homoclinic tangle. Typical structure is shown in Fig. 4.11.

case 2: a family not bounded by homoclinic orbits. $\Omega^H \in (\Omega_{\min}^H, \Omega_{\max}^H)$, $(\Omega_{\min}^H \neq 0)$

In Fig. 4.12, similar to Fig. 4.10, the curves are the graph of the position of the corresponding unperturbed orbit on ζ -axis with respect to the perturbation frequency Ω for several m 's of RB $\frac{m}{1}$. Because the natural frequency is bounded away from zero, the dynamics is strongly governed by the perturbation frequency. We make some remarks regarding perturbation frequency effects on the global dynamics.

Remark 1: Frequency range for RB $\frac{m}{1}$

Let us define frequency range for RB $\frac{m}{1}$ as follows:

$$\begin{aligned}\Omega_1^m &= m\Omega_{\min}^H \\ \Omega_2^m &= m\Omega_{\max}^H .\end{aligned}\tag{4.3}$$

Then RB $\frac{m}{1}$ exists only if the perturbation frequency Ω satisfies the following condition.

$$\Omega \in (m\Omega_{\min}^H, m\Omega_{\max}^H) .$$

Remark 2: Minimum frequency for the existence of RB $\frac{m}{1}$ for any order.

The minimum perturbation frequency to have any resonance band is $\Omega = \Omega_{\min}^H$ and the corresponding resonance band is RB $\frac{1}{1}$. For $\Omega < \Omega_{\min}^H$, there exists no RB $\frac{m}{1}$ for any m , i.e., a perturbation with a low frequency may not cause any irregular dynamics as is observed in Figs. 4.12 and 4.13. This means that the UEV motion in unsteady external flow field with low perturbation frequency is fairly regular for any initial configuration. As the frequency increases, the UEV motion near stable steady configuration begins to undergo irregular oscillation.

Remark 3: Frequency gap of order k

Suppose that there exists a k such that

$$\Omega_2^k < \Omega_1^{k+1} .$$

Then, for $\Omega \in (\Omega_2^k, \Omega_1^{k+1})$, there exists no unperturbed periodic orbit which satisfies the resonance relation $m\Omega^H = \Omega$ for any m . In other words, there exists no RB $\frac{m}{1}$ for any m . See Appendix 5 for proof. We call the interval in the perturbation frequency Ω (i.e., $\Omega \in (\Omega_2^k, \Omega_1^{k+1})$) as the frequency gap of order k . If the perturbation frequency of the external linear flow field for the UEV motion is in the frequency gap of order k , then the UEV motion is fairly regular for any initial configuration. We illustrate the frequency gap of order

k for $k = 1$ in Fig. 4.12.

Remark 4: Frequency gap of order $k^* < k$

Suppose that k satisfies the condition given in Remark 3. Then there exists a frequency gap of order k^* for $k^* < k$, and the frequency gap is given by $\Omega \in (\Omega_2^{k^*}, \Omega_1^{k^*+1})$. See Appendix 5 for proof.

Remark 5: Number of the frequency gaps N_g (highest of order N_g)

From Remark 4, the number of the frequency gaps N_g and the highest order for the frequency gap are the same.

$$N_g = \left[\frac{\Omega_{\min}^H}{\Omega_{\max}^H - \Omega_{\min}^H} + 1 \right],$$

where $[\Omega]$ denote the minimum integer which does not exceed Ω . See Appendix 5 for proof.

Remark 6: Further general remarks in terms of the UEV motion

If the perturbation frequency is in a gap, then every orbit lies in either KAM torus or cantorus, meaning that the motion is fairly regular for any orbit. Furthermore, if the order of the resonance m is less than N_g , then RB $\frac{m}{1}$ is the only resonance band in the phase space. The corresponding UEV motion for a perturbation with Ω in a gap is that the UEV undergoes fairly regular quasiperiodic motion to the perturbation frequency. Typical structure for a family which contains q_e at its center is shown in Fig. 4.13.

4.2.2.4 Transition dynamics through RB $\frac{m}{1}$

Recall that when the boundary of two regions corresponding to oscillation and rotation in the same direction in a steady external flow is defined by a PBO (periodic boundary orbit) which is an orbit going through the origin of the (δ, ζ) coordinate system ((c-c) PBO for (κ_0, σ_0) in 1^+ , 3^+ , 13^+ and (c) PBO for 15^+ ,

17^+). An orbit corresponding to oscillation (rotation resp.) does not (does resp.) contain the origin interior to itself.

In an unsteady external linear flow field, the transition dynamics of the UEV motion depends on whether the origin lies in a RB $\frac{m}{1}$, KAM torus or can torus. If the origin lies in KAM torus or can torus, then the UEV motion is regular and there exists no transition dynamics between oscillation and rotation. If the origin is contained in a RB $\frac{m}{1}$, then it may fluctuate in the band with large fluctuation amplitude. This corresponds to the irregular motion of the UEV flipping its type of motion between oscillation and rotation.

Notice that the transition dynamics through RB $\frac{m}{1}$ is strongly governed by the perturbation frequency Ω . The transition dynamics may not exist for some Ω , which is different from the transition dynamics through the homoclinic tangle. From Eqn. (4.3), the frequency range for the origin to be contained in RB $\frac{M}{1}$ is as follows:

$$\Omega \in ((m(\Omega_0^H - \Delta\Omega^{\frac{m}{1}}), (m(\Omega_0^H + \Delta\Omega^{\frac{m}{1}})) .$$

See Appendix 4 for proof. If the width of RB $\frac{m}{1}$ is larger, then the frequency range for the transition is larger.

4.3 Summary for qualitative UEV motion in time periodic external linear flow field

We summarize the qualitative UEV motion in time periodic linear external flow field for corresponding various (κ_0, σ_0) in $1^+, 3^+, 4^+, 5^+, 13^+, 14^+, 15^+$ and 17^+ in Table 4.1 together with mechanisms of the motion and the corresponding typical Poincaré maps.

4.4 The Melnikov techniques and its physical implication

4.4.1 Three types of perturbation and excess kinetic energy

We now come back to the equations of UEV motion and see how the perturbation imposed on the external linear flow field influences the UEV motion. Recall that the external linear flow field is determined by three parameters, i.e., the strength of the straining effect $\sigma(\tau)$, the inclination of the straining axis $\alpha(\tau)$ and the strength of the background vorticity $\kappa(\tau)$. Hence there are three types of perturbation corresponding to three parameters. For simplicity, we assume that the perturbation is imposed sinusoidally with period $T = 2\pi/\Omega$, but our methods apply to any periodic perturbation with period $T = 2\pi/\Omega$.

$$\begin{aligned}\sigma(\tau) &= \sigma_0 + \epsilon_\sigma \sigma_0 \sin \Omega(\tau + \tau_\sigma) \\ \alpha(\tau) &= \epsilon_\alpha \sin \Omega(\tau + \tau_\alpha) \\ \kappa(\tau) &= \kappa_0 + \epsilon_\kappa \kappa_0 \sin \Omega(\tau + \tau_\kappa) ,\end{aligned}$$

where $\epsilon_\sigma, \epsilon_\alpha, \epsilon_\kappa$ are perturbation amplitudes and $\tau_\sigma, \tau_\alpha, \tau_\kappa$ are phase shifts for each perturbation type. The equations of the UEV motion in the unsteady external linear flow field are written

$$\begin{pmatrix} \frac{dI}{d\tau} \\ \frac{d\varphi}{d\tau} \end{pmatrix} = \begin{pmatrix} -\frac{\partial}{\partial \varphi} \{H(I, \varphi; \sigma(\tau), \alpha(\tau), \kappa(\tau))\} \\ \frac{\partial}{\partial I} \{H(I, \varphi; \sigma(\tau), \alpha(\tau), \kappa(\tau))\} \end{pmatrix},$$

where

$$H(I, \varphi; \sigma(\tau), \alpha(\tau), \kappa(\tau)) = H_E(I) + H_S(I, \varphi; \sigma(\tau), \alpha(\tau)) + H_R(I; \kappa(\tau))$$

$$H_E(I) = \log(I + 4)$$

$$H_S(I, \varphi; \sigma(\tau), \alpha(\tau)) = \sigma(\tau) \sqrt{I^2 + 4I} \sin(\varphi - 2\alpha(\tau))$$

$$H_R(I; \kappa(\tau)) = \frac{\kappa(\tau)}{2} I .$$

The total Hamiltonian function $H(I, \varphi; \sigma, \alpha, \kappa)$ is constant in time,

$$\frac{d}{d\tau} H(I, \varphi; \sigma(\tau), \alpha(\tau), \kappa(\tau)) = \frac{dI}{d\tau} \frac{\partial H}{\partial I} + \frac{d\varphi}{d\tau} \frac{\partial H}{\partial \varphi} = 0 .$$

This physically means that the total excess kinetic energy in the entire flow field is conserved through the unsteady vortex interaction. (The external flow field can be viewed as the results from the vortex interaction.)

Recall that the arguments in Section 4.1-4.3 do not require any assumption on the perturbation but structural stability and time periodicity. Hence the dynamics of UEV is qualitatively the same under any type of time periodic perturbation in the external linear flow field. In this section, we discuss dynamics more quantitatively for each type of perturbation and examine how each perturbation influences the UEV dynamics using the Melnikov techniques. In doing so, we describe the geometrical meaning of the Melnikov function in terms of the UEV motion first.

The Melnikov functions on the homoclinic orbits and resonance bands are interpreted in terms of the UEV motion as follows. On the homoclinic orbit, the Melnikov function $M(\tau_0; \sigma_0, \kappa_0; \Omega)$ is related to the signed distance between stable and unstable manifolds of the hyperbolic fixed point and measures the size of the chaotic transition region, i.e., it defines a range for the UEV configuration along the unperturbed homoclinic orbit so that a UEV may undergo chaotic or transition motion induced by lobe dynamics. It also defines the amplitude of the fluctuation in the UEV configuration. If the amplitude of $M(\tau_0; \sigma_0, \kappa_0; \Omega)$ is larger, then the corresponding UEV motion is more irregular. On RB $\frac{m}{1}$, the Melnikov function $M^{\frac{m}{1}}(\tau_0; \sigma_0, \kappa_0; \Omega)$, which is related to the existence of period m points, also measures the width of the band and gives the range for the UEV configuration to be contained in the band. The UEV motion whose corresponding orbit is contained in RB $\frac{m}{1}$ is irregular. The amplitude of the fluctuation in the UEV configuration can be computed based on $M^{\frac{m}{1}}(\tau_0; \sigma_0, \kappa_0; \Omega)$. Again the larger the amplitude of $M^{\frac{m}{1}}(\tau_0; \sigma_0, \kappa_0; \Omega)$ is, the more irregular corresponding UEV motion is. Furthermore, the frequency range for the transition between oscillation and rotation in the same direction to occur can be computed by $M^{\frac{m}{n}}(\tau_0; \sigma_0, \kappa_0; \Omega)$. Moreover, $M^{\frac{m}{n}}(\tau_0; \sigma_0, \kappa_0; \Omega)$ is identically zero for $n \neq 1$, meaning that there does not exist any ultraharmonic motion of the UEV up to the first order in ϵ .

Now we describe how each perturbation influences the UEV motion. Three perturbations are classified into two categories depending on how they influence the excess kinetic energies induced by the external linear flow field. The perturbation in $\sigma(\tau)$ for a fixed α_0 excites $H_S(I, \varphi; \sigma_0, \alpha_0)$ time periodically. Similarly, the perturbation in $\kappa(\tau)$ excites $H_R(I; \kappa_0)$ time periodically. We define that the

perturbation is the Hamiltonian perturbation of type 1 (external perturbation) if the time periodic perturbation in the parameter causes time periodic excitation of a part of the Hamiltonian. The perturbations in $\sigma(\tau)$ and $\kappa(\tau)$ are of this type.

$$H_S(I, \varphi; \sigma(\tau), \alpha_0) = \{1 + \epsilon_\sigma \sin \Omega(\tau + \tau_\sigma)\} H_S(I, \varphi; \sigma_0, \alpha_0)$$

$$H_R(I; \kappa(\tau)) = \{1 + \epsilon_\kappa \sin \Omega(\tau + \tau_\kappa)\} H_R(I; \kappa_0) .$$

The perturbation in $\alpha(\tau)$ for a fixed σ_0 is rewritten as follows:

$$H_S(I, \varphi; \sigma_0, \alpha(\tau)) = H_S(I, \varphi - 2\alpha(\tau); \sigma_0, 0)$$

$$= H_S(I, \varphi - 2\epsilon_\alpha \sin \Omega(\tau + \tau_\alpha); \sigma_0, 0) .$$

The perturbation in $\alpha(\tau)$ has the same effect on H_S as the oscillation of the absolute coordinate axis. Generally, it can be viewed as the origin of one of canonical variables (in this case φ) is perturbed around some level time periodically. We call this type of perturbation the Hamiltonian perturbation of type 2 (internal perturbation).

As is shown in Appendix 6, the forms of the Melnikov functions for both types of Hamiltonian perturbations in general provide nice physical implications regarding how the perturbations influence the dynamics. Here, we just use the consequences for each type of perturbation, i.e., $\sigma(\tau)$, $\alpha(\tau)$ and $\kappa(\tau)$, and interpret them as the UEV motion so as to understand the UEV dynamics together with the mechanisms of the motion in time periodic external linear flow fields.

4.4.2 Perturbation in $\sigma(\tau)$

On homoclinic orbit

The Melnikov function $M_\sigma(\tau_0; \sigma_0, \kappa_0; \Omega)$ for $\epsilon_\alpha = \epsilon_\kappa = 0$ (i.e., the perturbation imposed only on the strength of the straining effect $\sigma(\tau)$) is written as follows because the perturbation is the Hamiltonian perturbation of type 1 (see Appendix 6).

$$M_\sigma(\tau_0; \sigma_0, \kappa_0; \Omega) = \int_{-\infty}^{\infty} \left\{ \frac{d}{d\tau} H_S(I, \varphi; \sigma_0, \kappa_0) \right\} \sin \Omega(\tau + \tau_0 + \tau_\sigma) d\tau$$

$$= F_\sigma(\sigma_0, \kappa_0; \Omega) \cos \Omega(\tau_0 + \tau_\sigma)$$

$$F_\sigma(\sigma_0, \kappa_0; \Omega) = \int_{-\infty}^{\infty} \left\{ \frac{d}{d\tau} H_S(I, \varphi; \sigma_0, \kappa_0) \right\} \sin \Omega \tau d\tau ,$$

where the integrals are evaluated on the corresponding unperturbed homoclinic orbit. The Melnikov function $M_\sigma(\tau_0; \sigma_0, \kappa_0; \Omega)$ is related to the Fourier transform of the rate of change in the excess kinetic energy induced by the steady external straining effect. $F_\sigma(\sigma_0, \kappa_0; \Omega)$ is similar to $M_\sigma(\tau_0; \sigma_0, \kappa_0; \Omega)$ without phase shift τ_σ and parametrization variable τ_0 . In other words, if we know the UEV motion in the steady external linear flow field and how the straining effect contributes to the motion, then we also know how the UEV motion receives the influences of the perturbation in $\sigma(\tau)$ for a given perturbation frequency Ω through the Melnikov function. If the perturbation is imposed so that it is ‘synchronized with’ $\frac{d}{d\tau} H_S$ as the UEV evolves along the homoclinic orbit, then the UEV motion becomes most irregular.

In Section 3.3, we examined how the excess kinetic energy induced by the straining effect (H_S) changes in time for several types of the UEV motion in various (κ_0, σ_0) (see Fig. (3.5)). On IHO (inner homoclinic orbit), typically $|\frac{d}{d\tau} H_S|$ increases in time, attains a local and global maximum and decays exponentially as $\tau \rightarrow \infty$ due to the existence of the hyperbolic fixed point. Hence the typical behavior of the graph of $F_\sigma(\sigma_0, \kappa_0; \Omega)$ with respect to Ω is as follows (see Fig. 4.14). $|F_\sigma(\sigma_0, \kappa_0; \Omega)|$ increases linearly for Ω small, attains the local and global maximum at some frequency (Ω^e), and decays exponentially as $\Omega \rightarrow \infty$. We call the frequency which gives the global maximum of the $F_\sigma(\sigma_0, \kappa_0; \Omega)$ the extremum frequency and denote it by Ω_σ^e . The amplitude of $F_\sigma(\sigma_0, \kappa_0; \Omega)$ sensitively depends on Ω , i.e., the perturbation frequency is an important factor for the chaotic transition of the UEV when the perturbation is imposed on $\sigma(\tau)$.

On RB $\frac{m}{1}$

The Melnikov function $M_\sigma^{\frac{m}{1}}(\tau_0; \sigma_0, \kappa_0; \Omega)$ for $\epsilon_\alpha = \epsilon_\kappa = 0$ is written as follows for the Hamiltonian perturbation of type 1.

$$\begin{aligned} M_\sigma^{\frac{m}{1}}(\tau_0; \sigma_0, \kappa_0; \Omega) &= \int_{-\frac{mT}{2}}^{\frac{mT}{2}} \left\{ \frac{d}{d\tau} H_S(I, \varphi; \sigma_0, \kappa_0) \right\} \sin \Omega(\tau + \tau_0 + \tau_\sigma) d\tau \\ &= F_\sigma^{\frac{m}{1}}(\sigma_0, \kappa_0; \Omega) \cos \Omega(\tau_0 + \tau_\sigma) \end{aligned}$$

$$F_{\sigma^1}^{\frac{m}{1}}(\sigma_0, \kappa_0; \Omega) = \int_{-\frac{mT}{2}}^{\frac{mT}{2}} \left\{ \frac{d}{d\tau} H_S(I, \varphi; \sigma_0, \kappa_0) \right\} \sin \Omega \tau d\tau ,$$

where the integrals are evaluated on the corresponding invariant circle with the resonance relation $\Omega = m\Omega^H$ and Ω^H of the natural frequency of the unperturbed orbit. The Melnikov function $M_{\sigma^1}^{\frac{m}{1}}(\tau_0; \sigma_0, \kappa_0; \Omega)$ is related to the Fourier coefficient of the rate of change in the excess kinetic energy induced by the steady external straining effect. $F_{\sigma^1}^{\frac{m}{1}}(\sigma_0, \kappa_0; \Omega)$ is similar to $M_{\sigma^1}^{\frac{m}{1}}(\tau_0; \sigma_0, \kappa_0; \Omega)$ without phase shift τ_σ and parametrization variable τ_o . Again, if we know the UEV motion in the steady external linear flow field and how the straining effect contributes to the motion, then we also know how the UEV motion receives the influences of the perturbation in $\sigma(\tau)$ for a given perturbation frequency Ω through the Melnikov function. It is clear from the form of the Melnikov function and the graph of $\frac{d}{d\tau} H_S$ as shown in Fig. 3.5 that, on a given orbit of Ω^H , the amplitude of $F_{\sigma^1}^{\frac{m}{1}}(\sigma_0, \kappa_0; \Omega)$ with $\Omega = m\Omega^H$ is the largest for $m = 1$ because $\frac{d}{d\tau} H_S$ is more naturally ‘synchronized with’ $\sin \Omega \tau$ than $\sin \Omega m \tau$ for $m \geq 2$. Fig. 4.15 show the relation between the signed width of RB $\frac{m}{1}$ up to the first order on ϵ (i.e., $F_{\sigma^1}^{\frac{m}{1}}(\sigma_0, \kappa_0; \Omega) / \|f(q^H(-\tau_0))\|$), which is on the horizontal axis, and the position of the band on the ζ -axis, which is on the vertical axis. Each figure regards three types of perturbations for a (κ_0, σ_0) corresponding to either one of 1^+ , 3^+ , 5^+ , 13^+ , 17^+ in Fig. 3.5. The solid curve corresponds to the perturbation in $\sigma(\tau)$. On the vertical axis, the position of q_e (elliptic fixed point) is marked by a circle, the positions corresponding to PBO (periodic boundary orbit which governs the transition dynamics) are marked by an asterisk, and the positions corresponding to homoclinic orbits or q_h (hyperbolic fixed point) are marked by a triangle. When there exists a homoclinic orbit, the width of RB $\frac{m}{1}$ accumulates to the distance between stable and unstable manifolds of the homoclinic tangle (see Guckenheimer and Holmes [1983]).

4.4.3 Perturbation in $\kappa(\tau)$

On homoclinic orbit

Since the perturbation in $\kappa(\tau)$ excites H_R time periodically as the perturbation in $\sigma(\tau)$ excites H_S time periodically, we now examine the influence of the perturbation in the strength of the background vorticity effect on the UEV dynamics by examining the Melnikov function as we did for the perturbation in $\sigma(\tau)$. The Melnikov function $M_\kappa(\tau_0; \sigma_0, \kappa_0; \Omega)$ for $\epsilon_\sigma = \epsilon_\alpha = 0$ (i.e., the perturbation imposed only on the strength of the straining effect $\kappa(\tau)$) is written as follows:

$$\begin{aligned} M_\kappa(\tau_0; \sigma_0, \kappa_0; \Omega) &= \int_{-\infty}^{\infty} \left\{ \frac{d}{d\tau} H_R(I, \varphi; \sigma_0, \kappa_0) \right\} \sin \Omega(\tau + \tau_0 + \tau_\kappa) d\tau \\ &= F_\kappa(\sigma_0, \kappa_0; \Omega) \cos \Omega(\tau_0 + \tau_\kappa) \end{aligned}$$

$$F_\kappa(\sigma_0, \kappa_0; \Omega) = \int_{-\infty}^{\infty} \left\{ \frac{d}{d\tau} H_R(I, \varphi; \sigma_0, \kappa_0) \right\} \sin \Omega\tau d\tau ,$$

where the integrals are evaluated on the corresponding unperturbed homoclinic orbit. The Melnikov function $M_\kappa(\tau_0; \sigma_0, \kappa_0; \Omega)$ is related to the Fourier transform of the rate of change in the excess kinetic energy induced by the steady external background vorticity effect. If we know the UEV motion in the steady external linear flow field and how the background vorticity effect contributes to the motion, then we also know how the UEV motion receives the influences of the perturbation in $\kappa(\tau)$ for a given perturbation frequency Ω through the Melnikov function. If the perturbation is imposed so that it is ‘synchronized with’ $\frac{d}{d\tau} H_R$ as the UEV evolves along the homoclinic orbit, then the UEV motion becomes most irregular.

Again, we make use of the behavior of the excess kinetic energy (induced by the background vorticity effect in this case) with respect to time on the homoclinic orbit to predict the behavior of the Melnikov functions. On IHO, the behavior of $|\frac{d}{d\tau} H_R|$ is similar to $|\frac{d}{d\tau} H_S|$. Typically $|\frac{d}{d\tau} H_R|$ increases in time, attains a local and global maximum and decays exponentially as $\tau \rightarrow \infty$ due to the existence of the hyperbolic fixed point. Hence the typical behavior of the graph of $F_\kappa(\sigma_0, \kappa_0; \Omega)$ with respect to Ω is as follows (see Fig. 4.14). $|F_\kappa(\sigma_0, \kappa_0; \Omega)|$ increases linearly for Ω small, attains the local and global maximum at some frequency (Ω^ϵ), and decays exponentially as $\Omega \rightarrow \infty$. We call the frequency which gives the global maximum of the $F_\kappa(\sigma_0, \kappa_0; \Omega)$ the extremum frequency and denote it by Ω_κ^ϵ . The amplitude of $F_\kappa(\sigma_0, \kappa_0; \Omega)$ sensitively depends on the Ω , i.e., the perturbation frequency is an important factor for the chaotic transition of the UEV when the perturbation

is imposed on $\kappa(\tau)$. The behavior of $|\frac{d}{d\tau}H_R|$ on OHO (outer homoclinic orbit) is similar to $|\frac{d}{d\tau}H_R|$ on IHO, hence the behavior of the graph of $F_\kappa(\sigma_0, \kappa_0; \Omega)$ with respect to Ω on OHO is similar to the one on IHO.

On RB $\frac{m}{1}$

The Melnikov function $M_{\kappa^{\frac{m}{1}}}(\tau_0; \sigma_0, \kappa_0; \Omega)$ for $\epsilon_\kappa = \epsilon_\alpha = 0$ is written as follows:

$$\begin{aligned} M_{\kappa^{\frac{m}{1}}}(\tau_0; \sigma_0, \kappa_0; \Omega) &= \int_{-\frac{mT}{2}}^{\frac{mT}{2}} \left\{ \frac{d}{d\tau} H_R(I, \varphi; \sigma_0, \kappa_0) \right\} \sin \Omega(\tau + \tau_0 + \tau_\kappa) d\tau \\ &= F_{\kappa^{\frac{m}{1}}}(\sigma_0, \kappa_0; \Omega) \cos \Omega(\tau_0 + \tau_\kappa) \end{aligned}$$

$$F_{\kappa^{\frac{m}{1}}}(\sigma_0, \kappa_0; \Omega) = \int_{-\frac{mT}{2}}^{\frac{mT}{2}} \left\{ \frac{d}{d\tau} H_R(I, \varphi; \sigma_0, \kappa_0) \right\} \sin \Omega\tau d\tau ,$$

where the integrals are evaluated on the corresponding invariant circle with the resonance relation $\Omega = m\Omega^H$ and Ω^H of the natural frequency of the unperturbed orbit. The Melnikov function $M_{\kappa^{\frac{m}{1}}}(\tau_0; \sigma_0, \kappa_0; \Omega)$ is related to the Fourier coefficient of the rate of change in the excess kinetic energy induced by the steady external background vorticity effect. Again, if we know the UEV motion in the steady external linear flow field and how the background vorticity effect contributes to the motion, then we also know how the UEV motion receives the influences of the perturbation in $\kappa(\tau)$ for a given perturbation frequency Ω through the Melnikov function. It is clear from the form of the Melnikov function and the graph of $\frac{d}{d\tau}H_R$ as shown in Fig. 3.5 that, on a given orbit with Ω^H , the amplitude of $F_{\kappa^{\frac{m}{1}}}(\sigma_0, \kappa_0; \Omega)$ with $\Omega = m\Omega^H$ is largest for $m = 1$ because $\frac{d}{d\tau}H_S$ is more naturally synchronized with $\sin \Omega\tau$ than $\sin \Omega m\tau$ for $m \geq 2$. Fig. 4.15 show the relation between the signed width of RB $\frac{m}{1}$ up to the first order on ϵ (i.e., $F_{\kappa^{\frac{m}{1}}}(\sigma_0, \kappa_0; \Omega)/\|f(q^H(-\tau_0))\|$), which is on the horizontal axis, and the position of the band on the ζ -axis, which is on the vertical axis. Each figure regards three types of perturbations for a (κ_0, σ_0) corresponding to either one of 1^+ , 3^+ , 5^+ , 13^+ , 17^+ in Fig. 3.5. The broken curve with a dot corresponds to the perturbation in $\kappa(\tau)$. On the vertical axis, the position of q_e (elliptic fixed point) is marked by a circle, the positions corresponding to PBO (periodic boundary orbit which governs the transition dynamics) are marked by an asterisk, and the positions corresponding to homoclinic orbits or q_h (hyperbolic fixed point) are marked by a triangle. When there exists a homoclinic orbit, the

width of RB $\frac{m}{1}$ accumulates to the distance between stable and unstable manifolds of the homoclinic tangle (see Guckenheimer and Holmes [1983]).

4.4.4 Perturbation in $\alpha(\tau)$

On homoclinic orbit

The Melnikov function $M_\alpha(\tau_0; \sigma_0, \kappa_0; \Omega)$ for $\epsilon_\sigma = \epsilon_\kappa = 0$ (i.e., the perturbation imposed only on the inclination angle of the straining axis $\alpha(\tau)$) is written as follows because the perturbation is of Hamiltonian perturbation of type 2 (see Appendix 6).

$$\begin{aligned} M_\alpha(\tau_0; \sigma_0, \kappa_0; \Omega) &= \int_{-\infty}^{\infty} \left\{ \frac{d^2}{d\tau^2} I \right\} \sin \Omega(\tau + \tau_0 + \tau_\alpha) d\tau \\ &= F_\alpha(\sigma_0, \kappa_0; \Omega) \sin \Omega(\tau_0 + \tau_\alpha) \\ F_\alpha(\sigma_0, \kappa_0; \Omega) &= \int_{-\infty}^{\infty} \left\{ \frac{d^2}{d\tau^2} I \right\} \cos \Omega\tau d\tau, \end{aligned} \quad (4.4)$$

where the integrals are evaluated on the corresponding unperturbed homoclinic orbit. The Melnikov function $M_\sigma(\tau_0; \sigma_0, \kappa_0; \Omega)$ is related to the Fourier transform of the second derivative of the angular momentum of the UEV with respect to time in the steady external straining effect. $F_\alpha(\sigma_0, \kappa_0; \Omega)$ is similar to $M_\alpha(\tau_0; \sigma_0, \kappa_0; \Omega)$ without phase shift τ_α and parametrization variable τ_0 . In other words, if we know the UEV motion in the steady external linear flow field and how the angular momentum (or equivalently the aspect ratio) of the UEV changes, then we also know how the UEV motion receives the influences of the perturbation in $\alpha(\tau)$ for a given perturbation frequency Ω through the Melnikov function. If the perturbation is imposed so that it is ‘synchronized with’ $\frac{d^2}{d\tau^2} I$ as the UEV evolves along the homoclinic orbit, then the UEV motion becomes most irregular.

Again, we can use the same type of argument to predict the values of $M_\alpha(\tau_0; \sigma_0, \kappa_0; \Omega)$ as we used for $M_\sigma(\tau_0; \sigma_0, \kappa_0; \Omega)$ and $M_\kappa(\tau_0; \sigma_0, \kappa_0; \Omega)$. However,

if we integrate Eqn. (4.4) by parts once

$$M_\alpha(\tau_0; \sigma_0, \kappa_0; \Omega) = -\Omega \int_{-\infty}^{\infty} \left\{ \frac{d}{d\tau} I \right\} \sin \Omega(\tau + \tau_0 + \tau_\alpha) d\tau$$

$$F_\alpha(\sigma_0, \kappa_0; \Omega) = -\Omega \int_{-\infty}^{\infty} \left\{ \frac{d}{d\tau} I \right\} \sin \Omega\tau d\tau ,$$

then $F_\alpha(\sigma_0, \kappa_0; \Omega)$ and $F_\kappa(\sigma_0, \kappa_0; \Omega)$ have the following relation.

$$-\kappa_0 F_\alpha(\sigma_0, \kappa_0; \Omega) = \Omega F_\kappa(\sigma_0, \kappa_0; \Omega) . \quad (4.5)$$

For a given (κ_0, σ_0) , the ratio of values of $F_\alpha(\sigma_0, \kappa_0; \Omega)$ and $F_\sigma(\sigma_0, \kappa_0; \Omega)$ is proportional to the perturbation frequency Ω . The perturbation in $\alpha(\tau)$ and $\kappa(\tau)$ both are related to the angular velocity $\frac{d\varphi}{d\tau}$. This fact gives the relation in Eqn. (4.5).

Typical behavior of the graph of $F_\alpha(\sigma_0, \kappa_0; \Omega)$ with respect to Ω on both IHO and OHO is shown in Fig. 4.14, which can be predicted by Eqn. (4.5). The graph of $|F_\alpha(\sigma_0, \kappa_0; \Omega)|$ with respect to Ω increases quadratically in Ω for small Ω , attains the local and global maximum at Ω_α^e , and decays exponentially as $\Omega \rightarrow \infty$. From Eqn. (4.5) and the behavior of $F_\alpha(\sigma_0, \kappa_0; \Omega)$ and $F_\kappa(\sigma_0, \kappa_0; \Omega)$, it can be shown that the following relation holds:

$$\Omega_\alpha^e < \Omega_\kappa^e .$$

On RB $\frac{m}{1}$

The Melnikov function $M_\alpha^{\frac{m}{1}}(\tau_0; \sigma_0, \kappa_0; \Omega)$ for $\epsilon_\sigma = \epsilon_\kappa = 0$ is written as follows.

$$M_\alpha^{\frac{m}{1}}(\tau_0; \sigma_0, \kappa_0; \Omega) = \int_{-\frac{mT}{2}}^{\frac{mT}{2}} \left\{ \frac{d^2}{d\tau^2} I \right\} \sin \Omega(\tau + \tau_0 + \tau_\alpha) d\tau$$

$$= F_\alpha^{\frac{m}{1}}(\sigma_0, \kappa_0; \Omega) \sin \Omega(\tau_0 + \tau_\alpha)$$

$$F_\alpha^{\frac{m}{1}}(\sigma_0, \kappa_0; \Omega) = \int_{-\frac{mT}{2}}^{\frac{mT}{2}} \left\{ \frac{d^2}{d\tau^2} I \right\} \cos \Omega\tau d\tau ,$$

where the integrals are evaluated on the corresponding invariant circle with the resonance relation $m\Omega^H = \Omega$ and Ω^H of the natural frequency of the unperturbed orbit. The Melnikov function $M_\alpha^{\frac{m}{1}}(\tau_0; \sigma_0, \kappa_0; \Omega)$ is related to the Fourier coefficient of the second derivative of the angular momentum of the UEV with respect to time

in the steady external linear flow field. If we know the UEV motion in the steady external linear flow field and how the angular momentum (or equivalently the aspect ratio) of the UEV changes, then we also know how the UEV motion receives the influences of the perturbation in $\alpha(\tau)$ for a given perturbation frequency Ω through the Melnikov function. Again, the following relation holds for $F_\alpha^{\frac{m}{1}}(\sigma_0, \kappa_0; \Omega)$ and $F_\kappa^{\frac{m}{1}}(\sigma_0, \kappa_0; \Omega)$, i.e.,

$$-\kappa_0 F_\alpha(\sigma_0, \kappa_0; \Omega) = \Omega F_\kappa(\sigma_0, \kappa_0; \Omega) .$$

$F_\alpha^{\frac{m}{1}}(\sigma_0, \kappa_0; \Omega)$ is the largest for $m = 1$ because $\frac{d^2 I}{d\tau^2}$ is more naturally synchronized with $\sin \Omega\tau$ than $\sin \Omega m\tau$ for $m \geq 2$. Fig. 4.15 show the relation between the signed width of RB $\frac{m}{1}$ up to the first order on ϵ (i.e., $F_\alpha^{\frac{m}{1}}(\sigma_0, \kappa_0; \Omega)/\|f(q^H(-\tau_0))\|$), which is on the horizontal axis, and the position of the band on the ζ -axis, which is on the vertical axis. Each figure regards three types of perturbations for a (κ_0, σ_0) corresponding to either one of 1^+ , 3^+ , 5^+ , 13^+ , 17^+ in Fig. 3.5. The broken curve corresponds to the perturbation in $\alpha(\tau)$. On the vertical axis, the position of q_e (elliptic fixed point) is marked by a circle, the positions corresponding to PBO (periodic boundary orbit which governs the transition dynamics) are marked by an asterisk, and the positions corresponding to homoclinic orbits or q_h (hyperbolic fixed point) are marked by a triangle. When there exists a homoclinic orbit, the width of RB $\frac{m}{1}$ accumulates to the distance between stable and unstable manifolds of the homoclinic tangle (see Guckenheimer and Holmes [1983]).

4.4.5 Relation between perturbations and influences of parameters

Because the total kinetic energy is conserved in the flow field, there are some relations among F 's and among $F^{\frac{m}{1}}$'s. We make some remarks regarding those relations on both homoclinic orbits and periodic orbits, which we did not mention in the previous sections.

On homoclinic orbit

Remark 1:

From Eqn. (3.1), $F_\sigma(\sigma_0, \kappa_0; \Omega)$ and $F_\kappa(\sigma_0, \kappa_0; \Omega)$ have the following relation.

$$F_\sigma(\sigma_0, \kappa_0; \Omega) = -(F_\kappa(\sigma_0, \kappa_0; \Omega) + F_E(\sigma_0, \kappa_0; \Omega)) ,$$

where

$$\begin{aligned} F_E(\sigma_0, \kappa_0; \Omega) &= \int_{-\infty}^{\infty} \left\{ \frac{d}{d\tau} H_E(I, \varphi; \sigma_0, \kappa_0) \right\} \sin \Omega \tau d\tau \\ &= \int_{-\infty}^{\infty} \left\{ \left(\frac{1}{I+4} \right) \left(\frac{dI}{d\tau} \right) \right\} \sin \Omega \tau d\tau . \end{aligned}$$

$F_E(\sigma_0, \kappa_0; \Omega)$ corresponds to the Fourier transform of the rate of change in the self-induced excess kinetic energy. From the discussion in Sections 4.1,2,3,4 and 3.3, the graph of $F_E(\sigma_0, \kappa_0; \Omega)$ typically behaves like other F 's with respect to Ω . Since the level sets for $H_E(I)$ and $H_R(I)$ are both circular in $\delta - \zeta$ space, the extremum frequency for $F_E(\sigma_0, \kappa_0; \Omega)$ is same order as $F_\kappa(\sigma_0, \kappa_0; \Omega)$. It follows from the above equation that the extremum frequencies for $F_\sigma(\sigma_0, \kappa_0; \Omega)$ and $F_\kappa(\sigma_0, \kappa_0; \Omega)$ are the same order, i.e.,

$$\Omega_\sigma^e \sim \Omega_\kappa^e .$$

Remark 2:

Let us consider the steady parameter effects (κ_0, σ_0) on the extremum frequencies. In general, the extremum frequency Ω^e depends on how fast the orbit approaches the hyperbolic fixed point q_h . Hence, Ω^e sensitively depends on the eigenvalues at q_h and the elliptic fixed point on the positive $\zeta -$ axis (q_e^+) for IHO. For OHO, Ω^e depends on the eigenvalues at q_h and the elliptic fixed point on the negative $\zeta -$ axis (q_e^-), and the natural frequency at $I \rightarrow \infty$. It follows that $\Omega^e \rightarrow 0$ for (κ_0, σ_0) near bifurcation values given by the bifurcation curves S^+ , R and I_1^+ for IHO, and S^+ and R for OHO.

Remark 3:

Next we consider the steady parameter effects (κ_0, σ_0) on the amplitude of F 's. It is clear from the form of F 's that the amplitude of F 's is larger when $\frac{dI}{d\tau}$ on the corresponding is larger. Recall that IHO disappears to infinity for (κ_0, σ_0) close to I_1^+ , meaning that the amplitude of F 's also grows.

RB₁^m

Remark 1:

Eqn. (3.1) provides us with the same relation for $F_{\sigma}^{\frac{m}{1}}, F_{\kappa}^{\frac{m}{1}}(\sigma_0, \kappa_0; \Omega)$ as for the homoclinic orbit, i.e., we have the following relation.

$$F_{\sigma}^{\frac{m}{1}}(\sigma_0, \kappa_0; \Omega) = -(F_{\kappa}^{\frac{m}{1}}(\sigma_0, \kappa_0; \Omega) + F_E^{\frac{m}{1}}(\sigma_0, \kappa_0; \Omega)),$$

where

$$\begin{aligned} F_E^{\frac{m}{1}}(\sigma_0, \kappa_0; \Omega) &= \int_{-\frac{mT}{2}}^{\frac{mT}{2}} \left\{ \frac{d}{d\tau} H_E(I, \varphi; \sigma_0, \kappa_0) \right\} \sin \Omega \tau d\tau \\ &= \int_{-\frac{mT}{2}}^{\frac{mT}{2}} \left\{ \left(\frac{1}{I+4} \right) \left(\frac{dI}{d\tau} \right) \right\} \sin \Omega \tau d\tau . \end{aligned}$$

$F_E^{\frac{m}{1}}(\sigma_0, \kappa_0; \Omega)$ corresponds to the Fourier coefficient of the rate of change in the self-induced excess kinetic energy.

Remark 2:

When $F_{\tau}^{\frac{m}{1}}$'s changes its sign as the perturbation frequency varies for a given (κ_0, σ_0) , the bifurcation of RB $\frac{m}{1}$ which we discussed in Section 4.2.2.1 occurs.

4.4.6 Perturbation in all parameters

When the perturbation is imposed on all parameters $(\sigma(\tau), \alpha(\tau), \kappa(\tau))$ in the external linear flow field simultaneously, it can be shown that the total Melnikov functions on the homoclinic orbit $M_{tot}(\tau_0; \sigma_0, \kappa_0; \Omega)$ and on RB $\frac{m}{1}$ $M_{tot}^{\frac{m}{1}}(\tau_0; \sigma_0, \kappa_0; \Omega)$ are a superposition of the Melnikov functions corresponding to three types of the perturbations, i.e., on the homoclinic orbit

$$M_{tot}(\tau_0, \sigma_0, \kappa_0; \Omega) =$$

$$\epsilon_{\sigma} M_{\sigma}(\tau_0; \sigma_0, \kappa_0; \Omega) + \epsilon_{\alpha} M_{\alpha}(\tau_0; \sigma_0, \kappa_0; \Omega) + \epsilon_{\kappa} M_{\kappa}(\tau_0; \sigma_0, \kappa_0; \Omega) .$$

Similarly, on RB $\frac{m}{1}$

$$M_{tot}^{\frac{m}{1}}(\tau_0, \sigma_0, \kappa_0; \Omega) =$$

$$\epsilon_{\sigma} M_{\sigma}^{\frac{m}{1}}(\tau_0; \sigma_0, \kappa_0; \Omega) + \epsilon_{\alpha} M_{\alpha}^{\frac{m}{1}}(\tau_0; \sigma_0, \kappa_0; \Omega) + \epsilon_{\kappa} M_{\kappa}^{\frac{m}{1}}(\tau_0; \sigma_0, \kappa_0; \Omega) .$$

Note that both total Melnikov functions are order of ϵ here.

Now we discuss the properties of the total Melnikov functions. We first discuss $M_{tot}(\tau_0; \sigma_0, \kappa_0; \Omega)$ on the homoclinic orbit. A similar argument holds for $M_{tot}^{\frac{m}{1}}(\tau_0; \sigma_0, \kappa_0; \Omega)$.

To discuss the properties of the Melnikov function on the homoclinic orbit $M_{tot}(\tau_0; \sigma_0, \kappa_0; \Omega)$, we first redefine the phase shifts $\tau_\sigma, \tau_\alpha, \tau_\kappa$ to $\tau_\sigma^*, \tau_\alpha^*, \tau_\kappa^*$ as follows:

$$\begin{aligned}\epsilon_\sigma F_\sigma \sin \Omega(\tau_0 + \tau_\sigma) &= |\epsilon_\sigma F_\sigma| \sin \Omega(\tau_0 + \tau_\sigma^*) \\ \epsilon_\alpha F_\alpha \sin \Omega(\tau_0 + \tau_\alpha) &= |\epsilon_\alpha F_\alpha| \sin \Omega(\tau_0 + \tau_\alpha^*) \\ \epsilon_\kappa F_\kappa \sin \Omega(\tau_0 + \tau_\kappa) &= |\epsilon_\kappa F_\kappa| \sin \Omega(\tau_0 + \tau_\kappa^*),\end{aligned}$$

i.e., for $i = \sigma$ and κ

$$\tau_i^* = \begin{cases} \tau_i & \text{if } F_i > 0 \\ \tau_i + \frac{\pi}{\Omega} & \text{if } F_i < 0 \end{cases},$$

i.e., for α

$$\tau_\alpha^* = \begin{cases} \tau_\alpha & \text{if } F_\alpha > 0 \\ \tau_\alpha + \frac{\pi}{2\Omega} & \text{if } F_\alpha < 0 \end{cases},$$

The total Melnikov function is as follows:

$$M_{tot}(\tau : \sigma_0, \kappa_0; \Omega) = F_{tot}(\sigma_0, \kappa_0; \Omega) \sin \Omega(\tau_0 + \tau_{tot}),$$

where

$$\begin{aligned}F_{tot} &= \{(c_\sigma + c_\alpha + c_\kappa)^2 + (s_\sigma + s_\alpha + s_\kappa)^2\}^{\frac{1}{2}} \\ \tau_{tot} &= \frac{1}{\Omega} \tan^{-1} \frac{s_\sigma + s_\alpha + s_\kappa}{c_\sigma + c_\alpha + c_\kappa}\end{aligned}$$

with

$$\begin{aligned}(c_\sigma, s_\sigma) &= (|\epsilon_\sigma F_\sigma| \cos \Omega \tau_\sigma^*, |\epsilon_\sigma F_\sigma| \sin \Omega \tau_\sigma^*) \\ (c_\alpha, s_\alpha) &= (|\epsilon_\alpha F_\alpha| \cos \Omega \tau_\alpha^*, |\epsilon_\alpha F_\alpha| \sin \Omega \tau_\alpha^*) \\ (c_\kappa, s_\kappa) &= (|\epsilon_\kappa F_\kappa| \cos \Omega \tau_\kappa^*, |\epsilon_\kappa F_\kappa| \sin \Omega \tau_\kappa^*).\end{aligned}$$

Recall that F_σ, F_α and F_κ are given for a fixed (κ_0, σ_0) and Ω . We now examine how the phase shift effects control the total UEV motion through the Melnikov function. We consider the following two cases, i.e., 1) maximization of $F_{tot}(\sigma_0, \kappa_0; \Omega)$, and 2) minimization of $F_{tot}(\sigma_0, \kappa_0; \Omega)$.

1) maximization of $F_{tot}(\sigma_0, \kappa_0; \Omega)$:

$F_{tot}(\sigma_0, \kappa_0; \Omega)$ can be rewritten as follows:

$$\begin{aligned} F_{tot}(\sigma_0, \kappa_0; \Omega) &= (\epsilon_\sigma F_\sigma)^2 + (\epsilon_\alpha F_\alpha)^2 + (\epsilon_\kappa F_\kappa)^2 \\ &\quad + 2 | \epsilon_\sigma \epsilon_\alpha F_\sigma F_\alpha | \cos \Omega(\tau_\sigma^* - \tau_\kappa^*) \\ &\quad + 2 | \epsilon_\sigma \epsilon_\kappa F_\sigma F_\kappa | \cos \Omega(\tau_\sigma^* - \tau_\alpha^*) \\ &\quad + 2 | \epsilon_\alpha \epsilon_\kappa F_\alpha F_\kappa | \cos \Omega(\tau_\alpha^* - \tau_\kappa^*) . \end{aligned}$$

It is clear that $F_{tot}(\sigma_0, \kappa_0; \Omega)$ is maximum when the following relation is satisfied:

$$\tau_\sigma^* = \tau_\alpha^* = \tau_\kappa^* .$$

The corresponding $F_{tot}(\sigma_0, \kappa_0; \Omega)$ is

$$\begin{aligned} F_{tot}(\sigma_0, \kappa_0; \Omega)|_{\max} &= (\epsilon_\sigma F_\sigma)^2 + (\epsilon_\alpha F_\alpha)^2 + (\epsilon_\kappa F_\kappa)^2 \\ &\quad + 2(| \epsilon_\sigma \epsilon_\alpha F_\sigma F_\alpha | + | \epsilon_\sigma \epsilon_\kappa F_\sigma F_\kappa | + | \epsilon_\alpha \epsilon_\kappa F_\alpha F_\kappa |) . \end{aligned}$$

2) minimization of $F_{tot}(\sigma_0, \kappa_0; \Omega)$:

For the minimization of $F_{tot}(\sigma_0, \kappa_0; \Omega)$, we first define F_1, F_2 and F_3 as follows:

$$\begin{aligned} F_1 &= \sup\{|\epsilon_\sigma F_\sigma|, |\epsilon_\alpha F_\alpha|, |\epsilon_\kappa F_\kappa|\} \\ F_2 &= \inf\{|\epsilon_\sigma F_\sigma|, |\epsilon_\alpha F_\alpha|, |\epsilon_\kappa F_\kappa|\} \\ F_3 &= \{|\epsilon_\sigma F_\sigma|, |\epsilon_\alpha F_\alpha|, |\epsilon_\kappa F_\kappa| \mid F_3 \neq F_1, F_3 \neq F_2\} . \end{aligned}$$

Then the minimum value of $F_{tot}(\sigma_0, \kappa_0; \Omega)$ depends on the relation among F_1, F_2 and F_3 .

$$F_1 > F_2 + F_3:$$

$$F_{tot}(\sigma_0, \kappa_0; \Omega)|_{\min} = F_1 - F_2 - F_3 ,$$

with

$$\tau_2^* = \tau_3^* = \tau_1^* + \frac{\pi}{\Omega} ,$$

where subscripts for F 's and τ^* commute each other.

$$F_1 < F_2 + F_3:$$

$$F_{tot}(\sigma_0, \kappa_0; \Omega)|_{\min} = 0 ,$$

where τ_1^*, τ_2^* and τ_3^* satisfy the following condition.

$$\sin \Omega(\tau_3^* + \tau_1^*) = -\frac{F_2}{F_3} \sin \Omega(\tau_2^* + \tau_1^*) .$$

When $F_{tot}(\sigma_0, \kappa_0; \Omega)$ is maximum, the UEV motion becomes wild (i.e., enhancement of chaos). On the other hand, if $F_{tot}(\sigma_0, \kappa_0; \Omega)$ is small, then the UEV motion becomes less irregular (i.e., suppression of chaos). By changing the phase shifts of the perturbation, we can control the UEV motion.

Similar argument holds for the UEV motion on RB $\frac{m}{1}$. Again, by changing the phase shifts in the perturbations, we can control the UEV motion.

4.5 Figures and table for Chapter 4

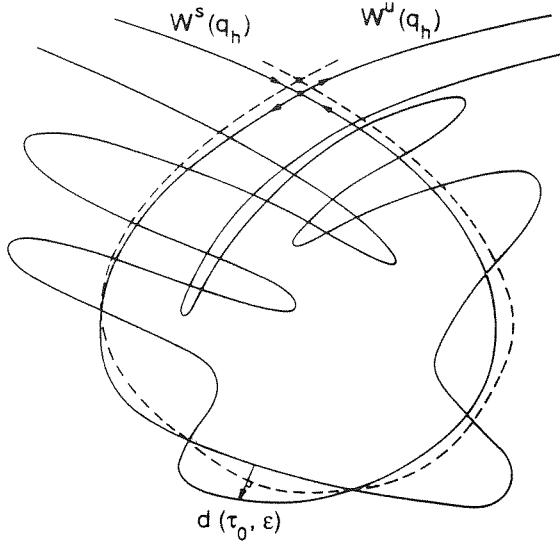


Figure 4.1 Geometrical structure of a homoclinic tangle

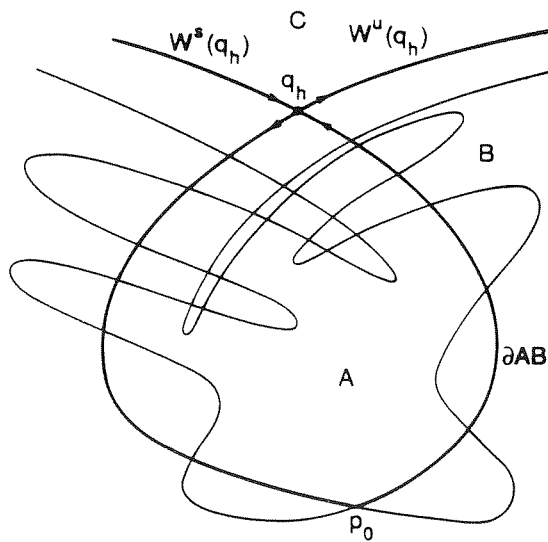


Figure 4.2 Primary intersection point

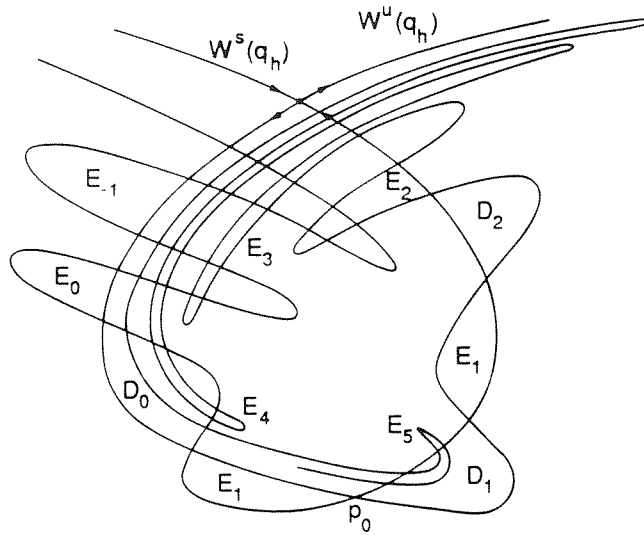


Figure 4.3 Ordering of the lobes

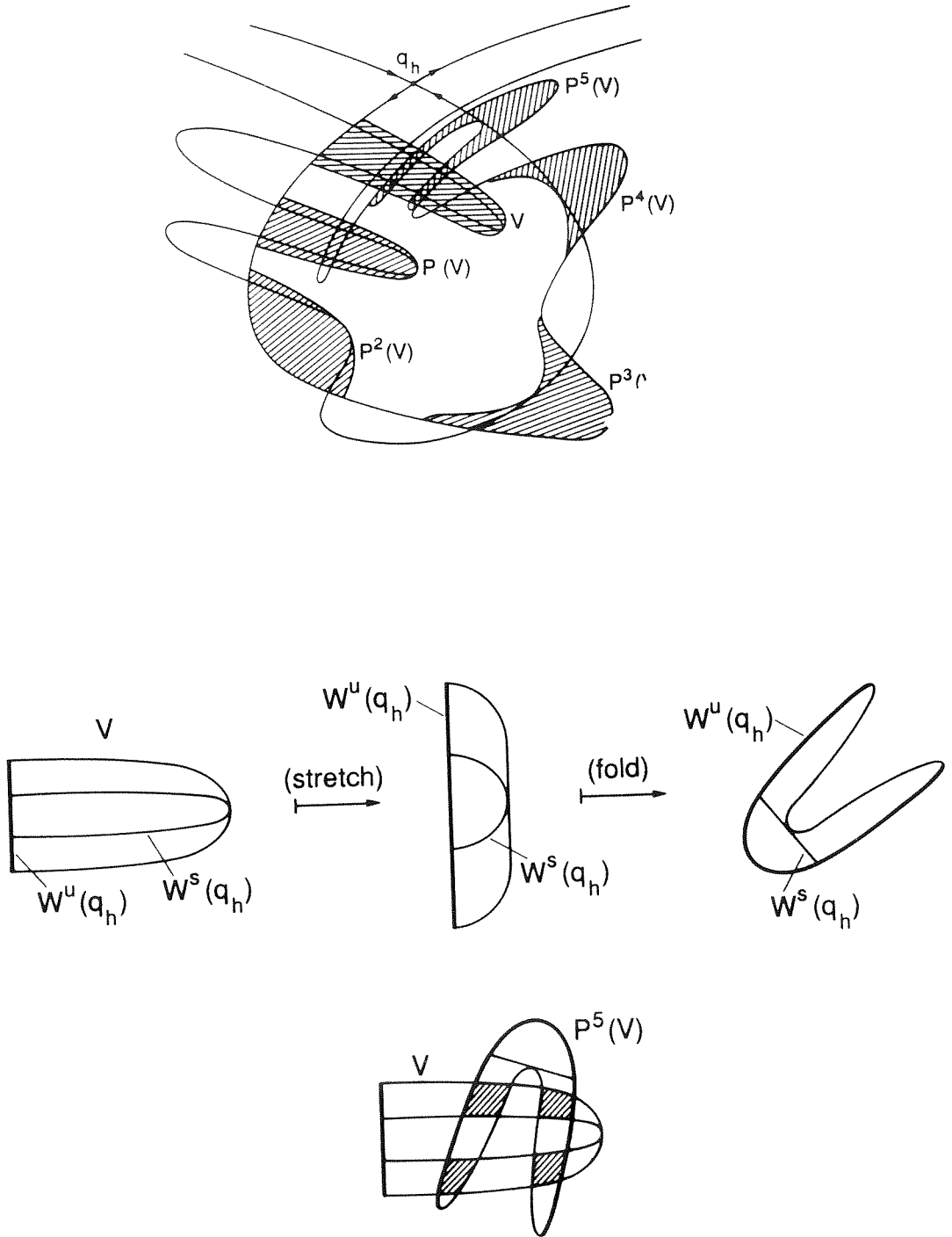


Figure 4.4 Horseshoe map

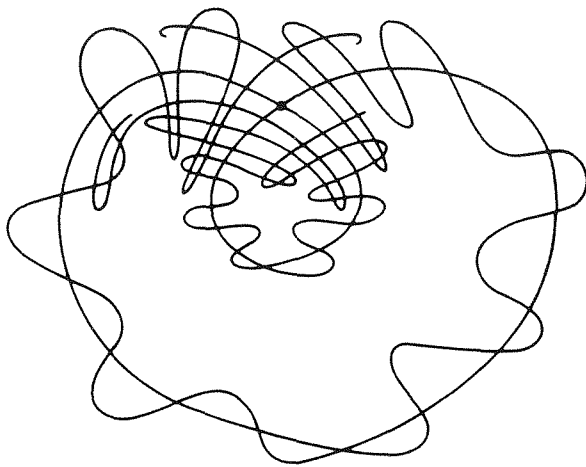


Figure 4.5 Two homoclinic tangles

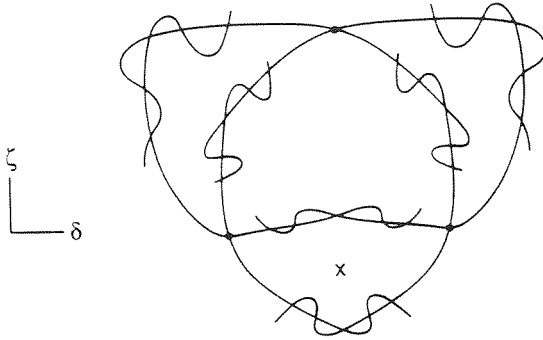


Figure 4.6 Resonance band of order $\frac{m}{n}$ for $m = 3, n = 1$ and $\ell = 1$

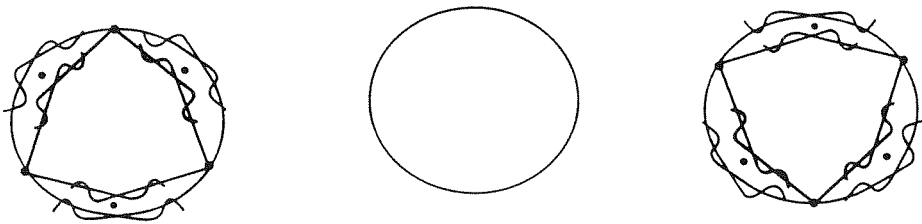


Figure 4.7 Bifurcation on resonance band of order $\frac{m}{n}$ for $m = 3, n = 1$ and $\ell = 1$

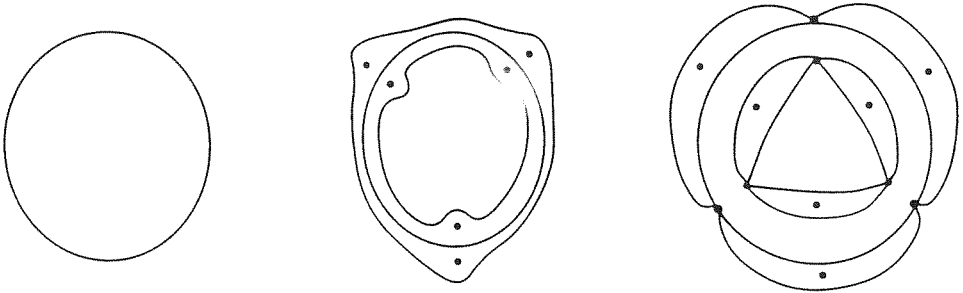


Figure 4.8 Bifurcation of a resonance band on nontwisting band for $m = 3, n = 1$ and $l = 1$

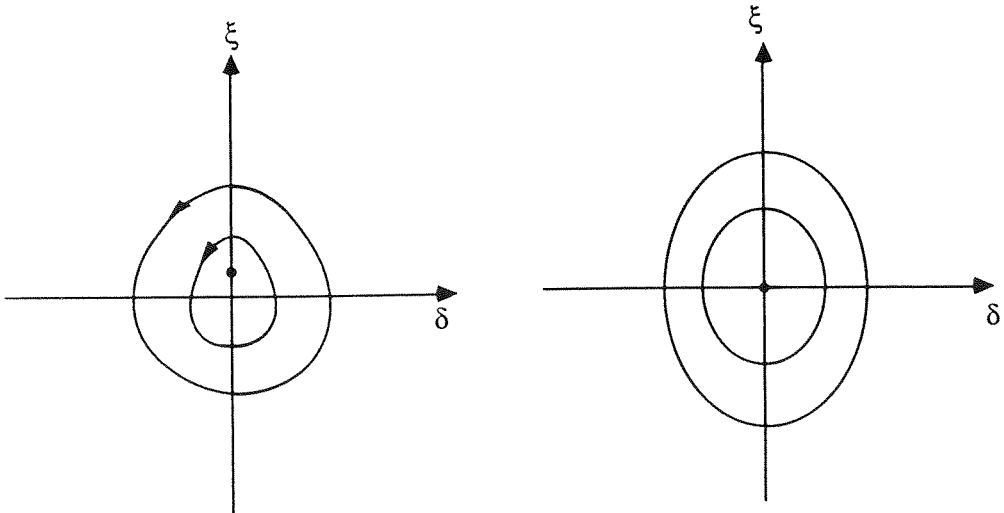


Figure 4.9 Geometrical symmetry in the unperturbed phase space
(a) ζ -axis (b) δ -axis and ζ -axis

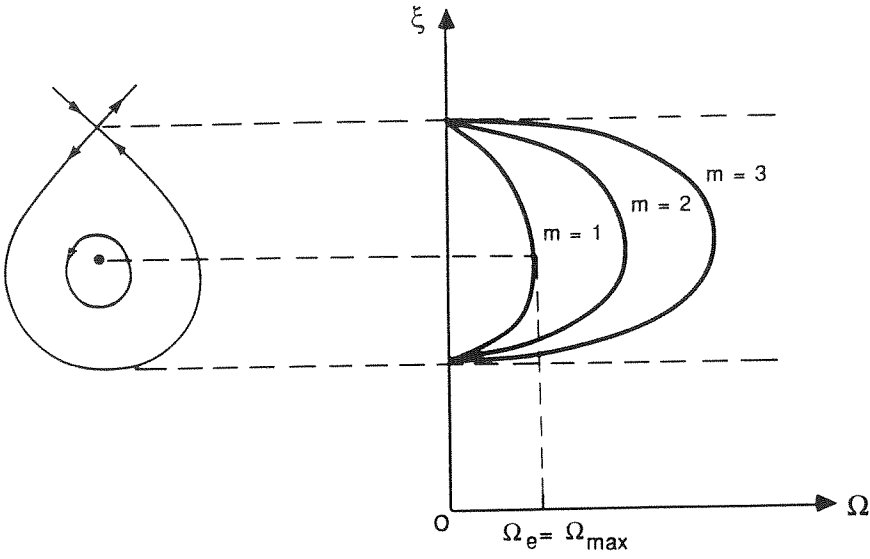


Figure 4.10 Periodic orbits bounded by a homoclinic orbit and its geometrical relation to RB $\frac{m}{n}$

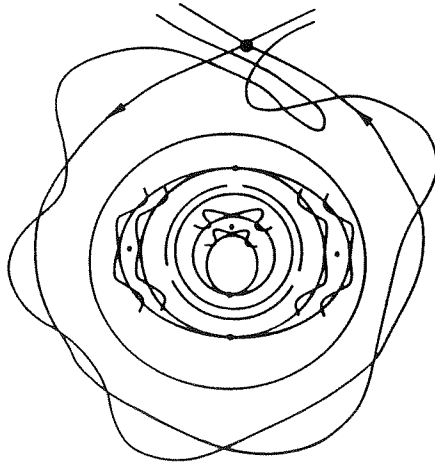


Figure 4.11 Global resulting structure for one parameter family of periodic orbits bounded by a homoclinic orbit

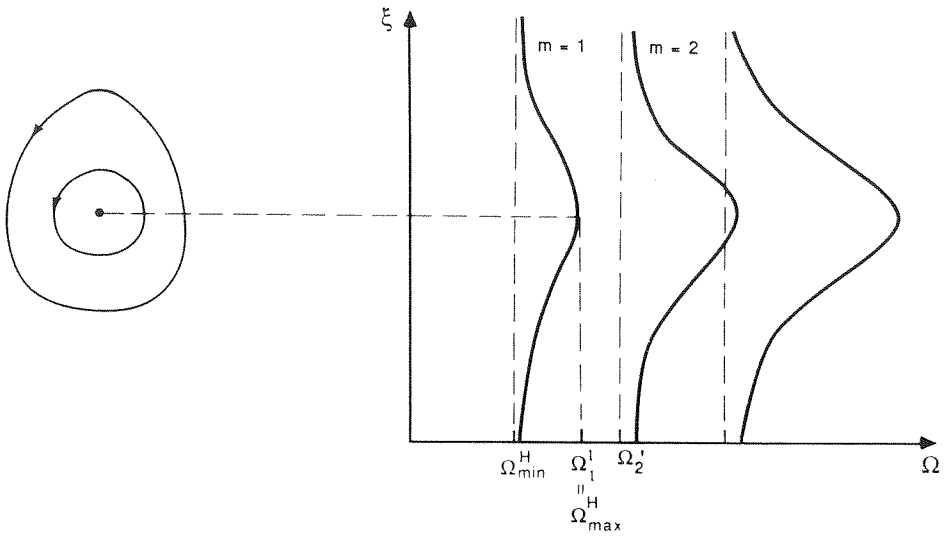


Figure 4.12 Periodic orbits not bounded by a homoclinic orbit and their geometrical relation to RB $\frac{m}{n}$

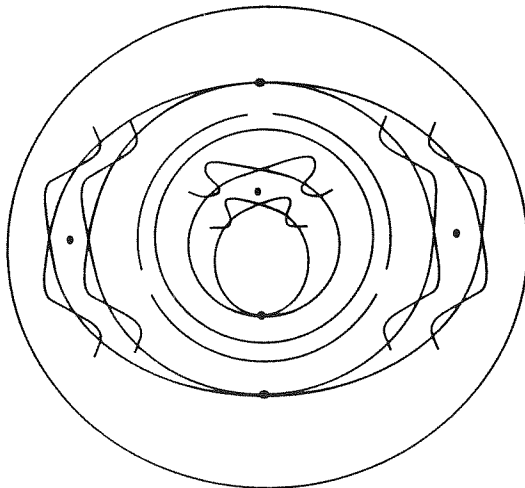


Figure 4.13 Global resulting structure for periodic orbits not bounded by a homoclinic orbit

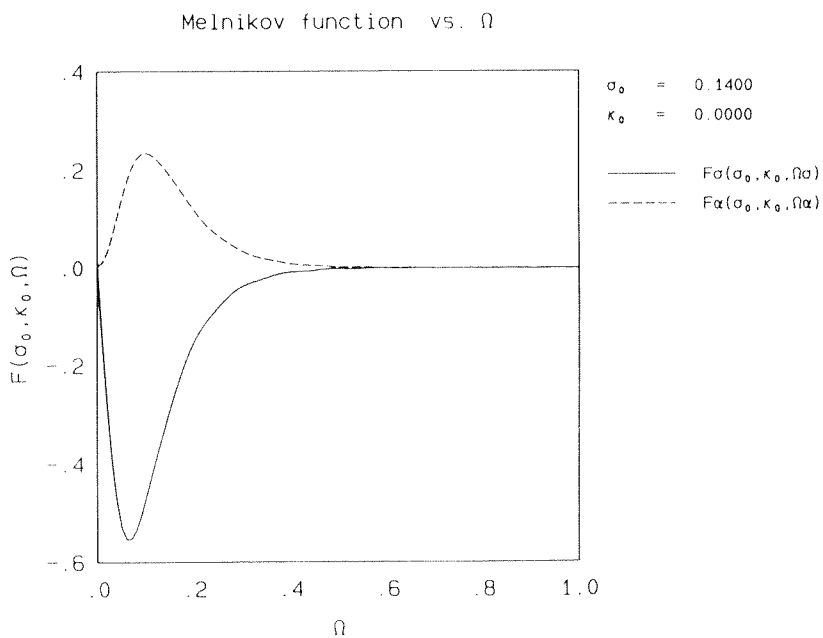
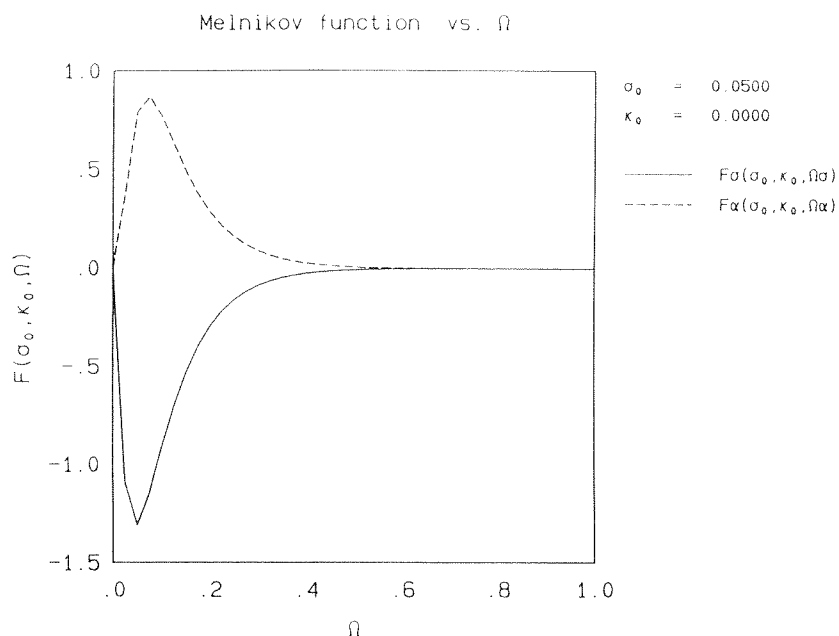
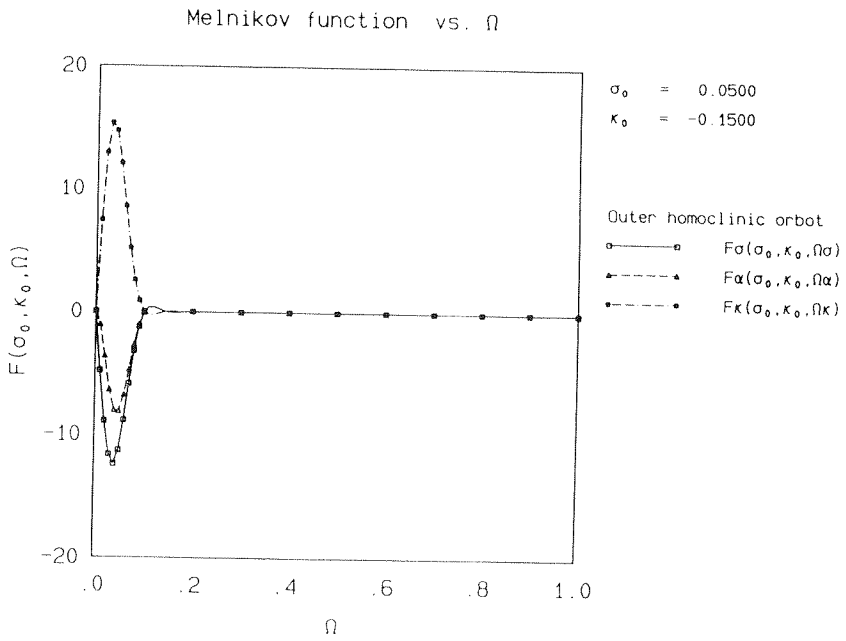
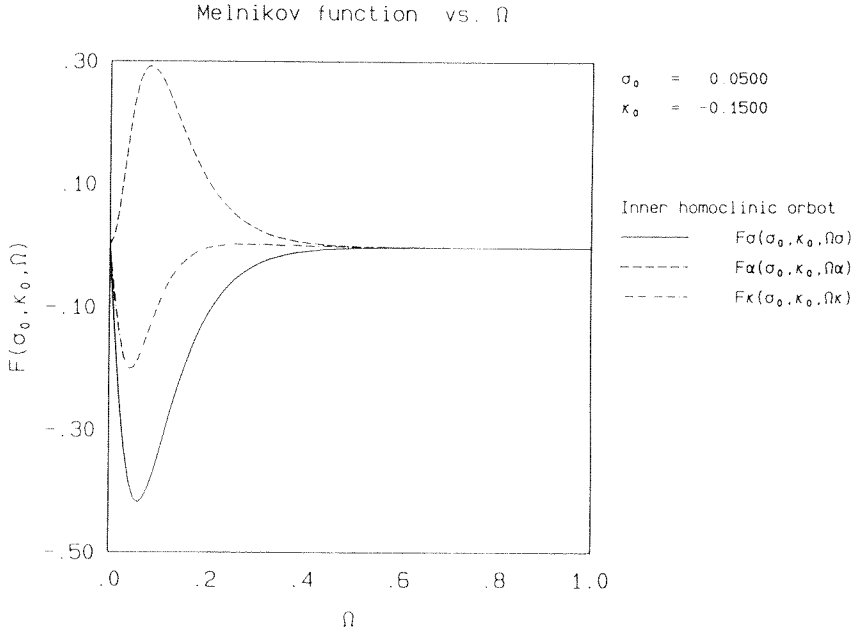
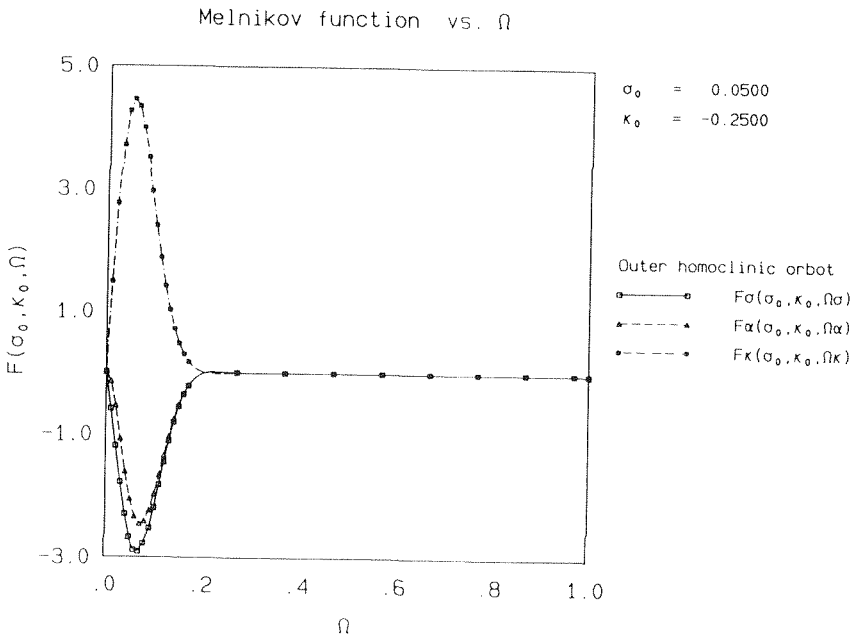
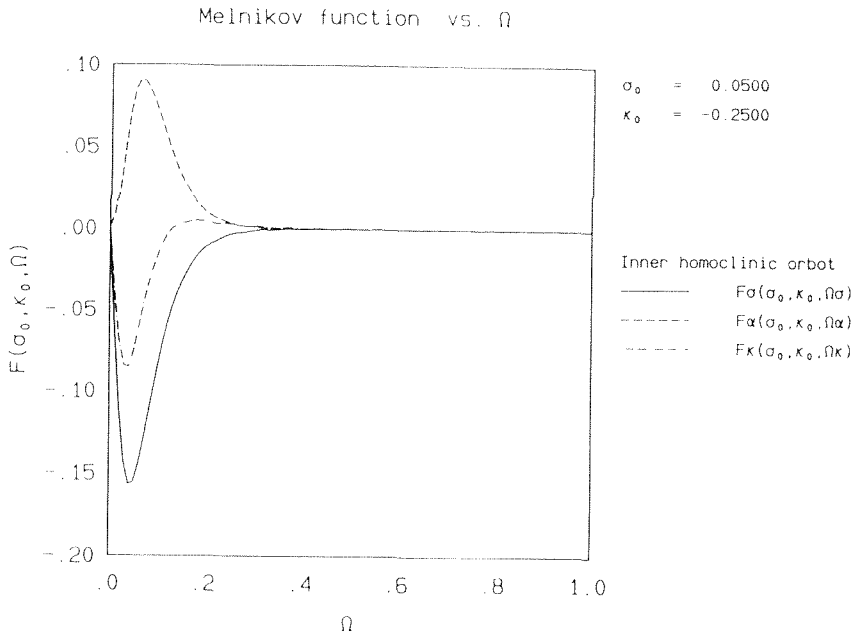


Figure 4.14 Graph of $F(\sigma_0, \kappa_0; \Omega)$ with respect to Ω



(κ_0, σ_0) in 13^+ on IHO and OHO



(κ_0, σ_0) in 15^+ on IHO and OHO

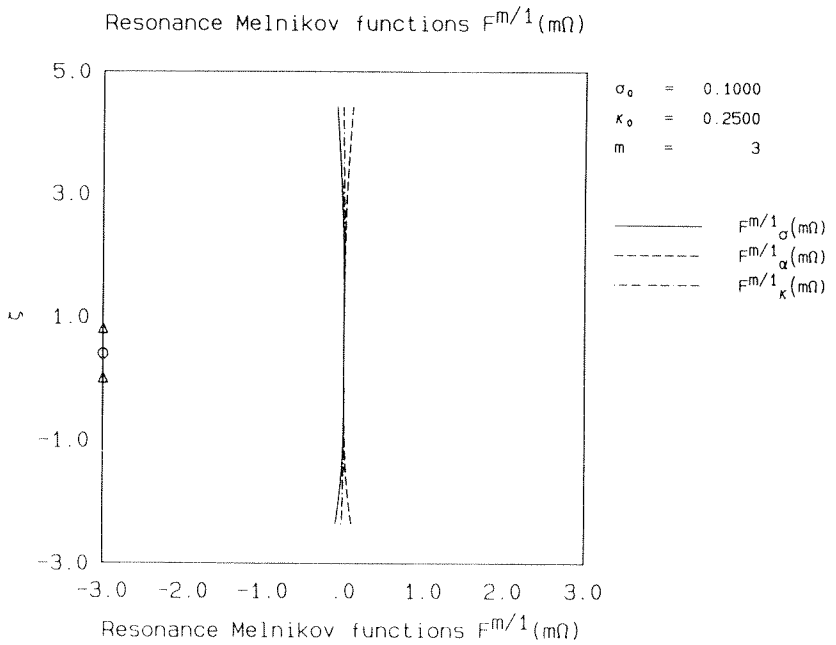
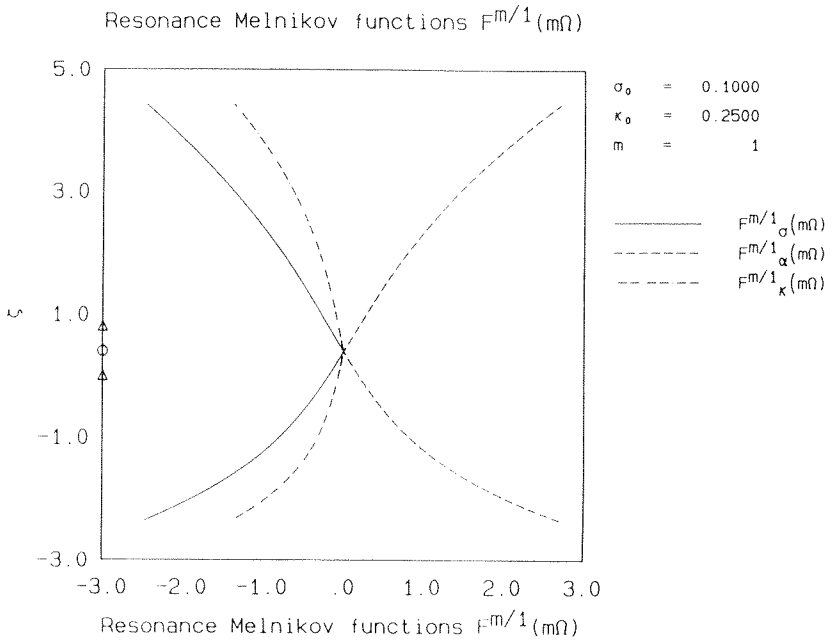
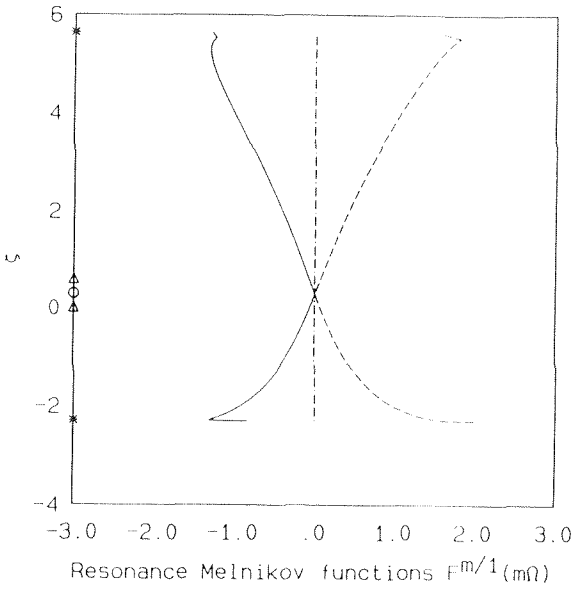


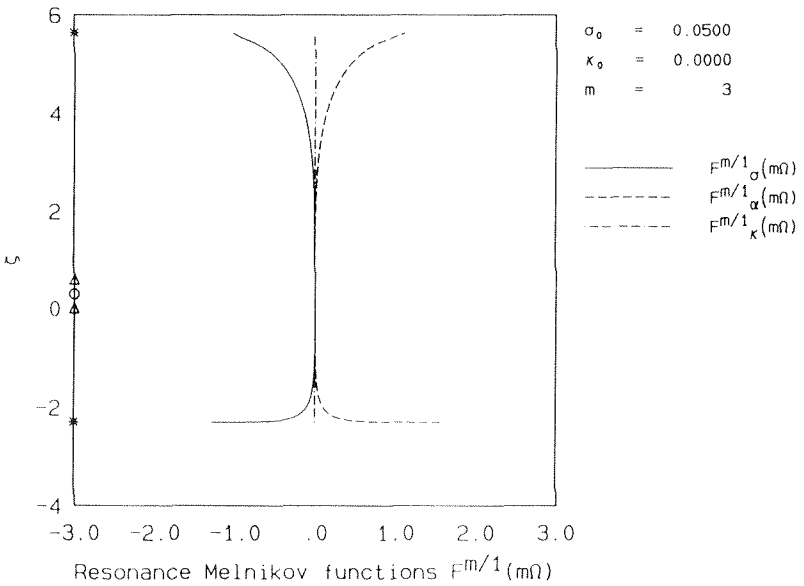
Figure 4.15 Width of RB $\frac{m}{1}$ and its position

(κ_0, σ_0) in 1^+ for $m = 1, 3$

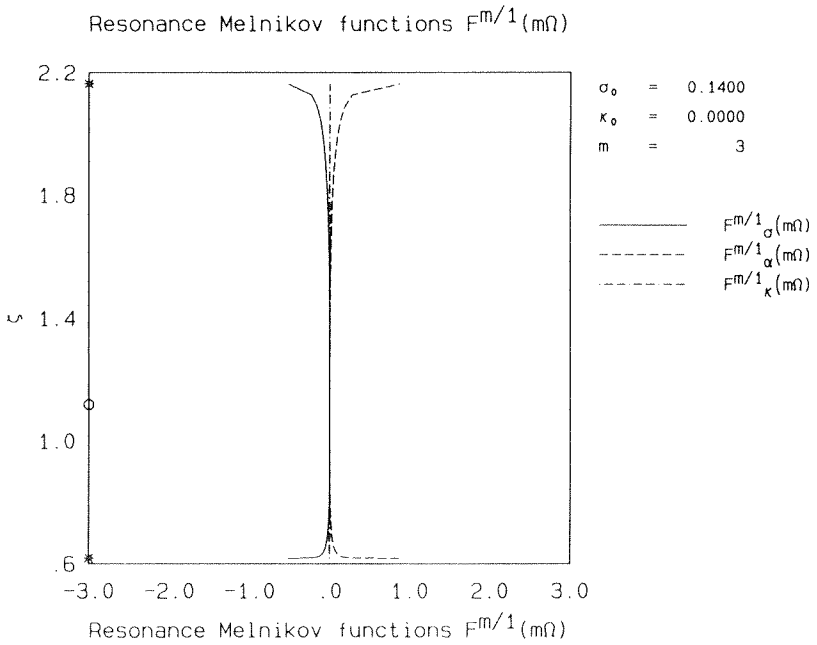
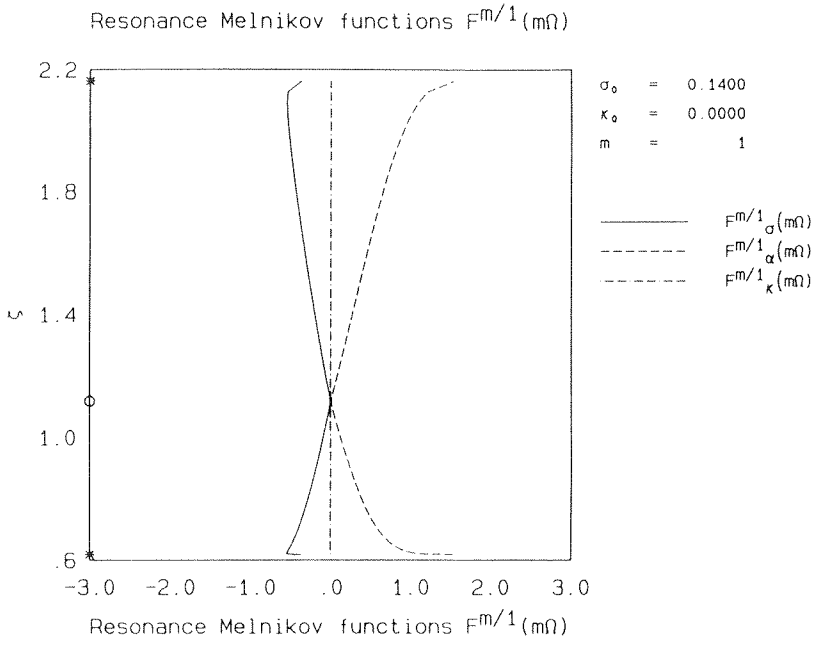
Resonance Melnikov functions $F^{m/1}(\eta\Omega)$



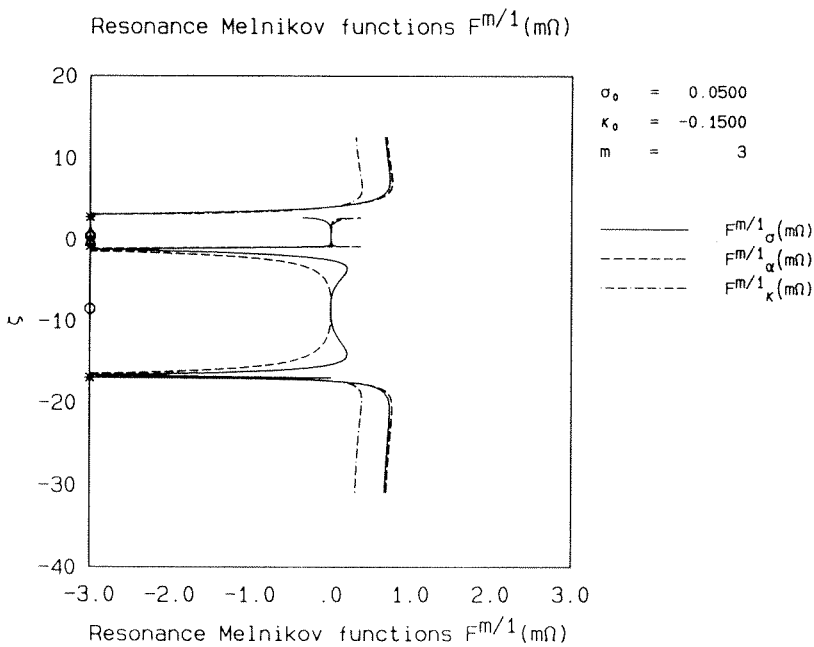
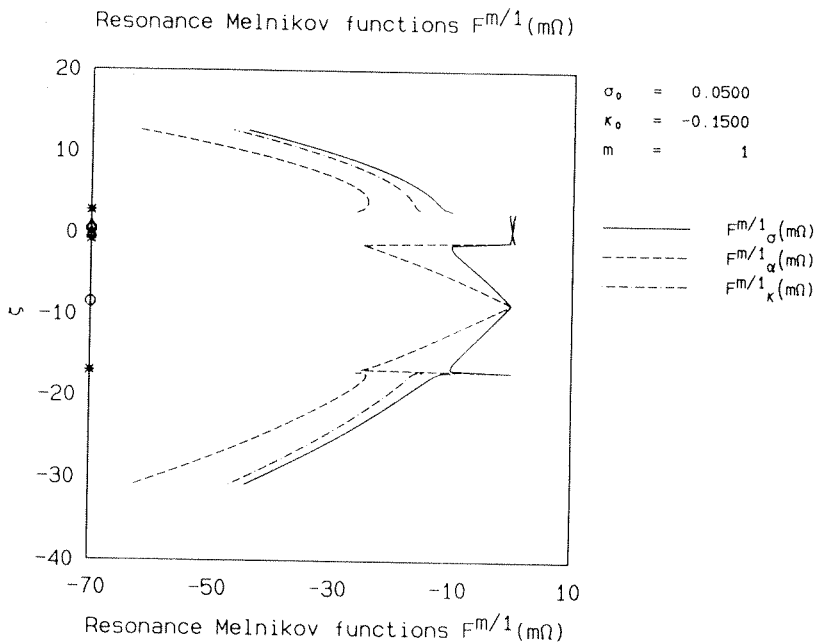
Resonance Melnikov functions $F^{m/1}(\eta\Omega)$



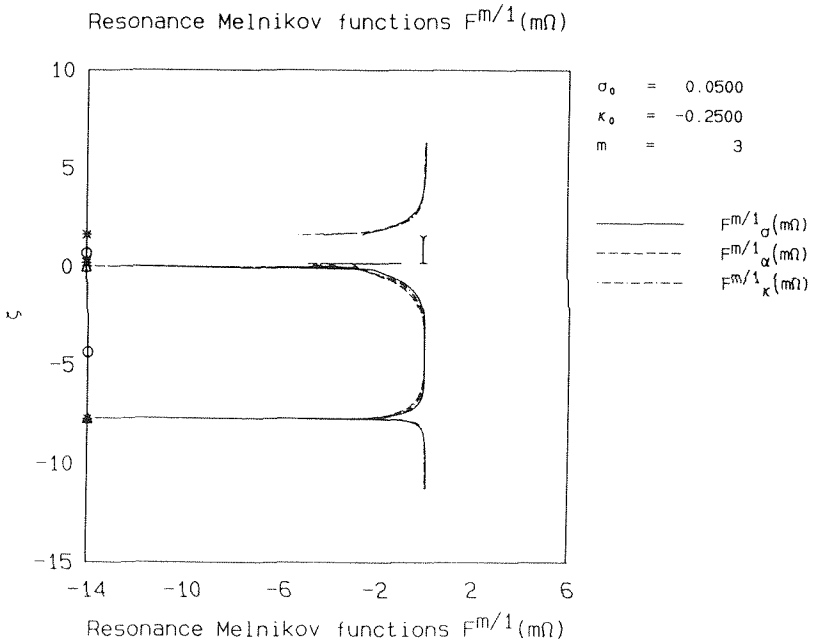
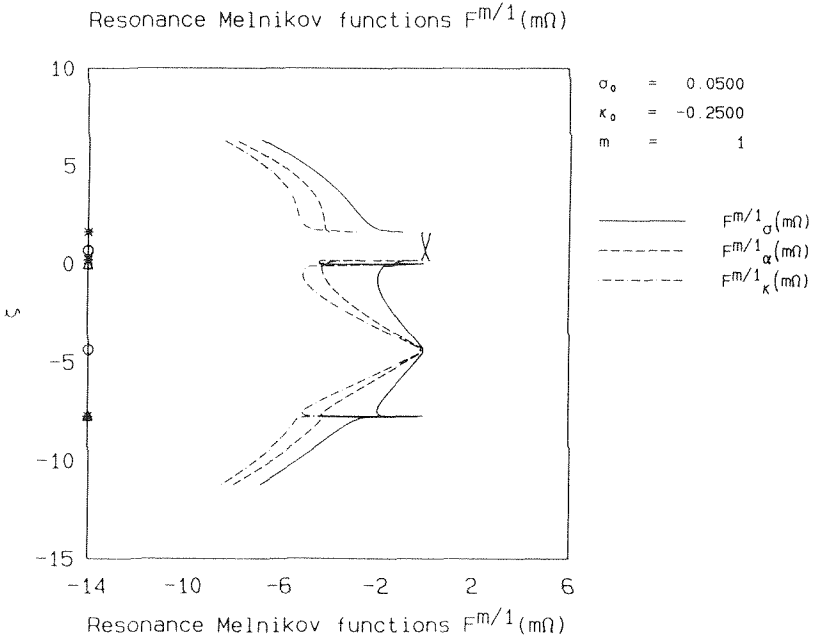
(κ_0, σ_0) in 3^+ for $m = 1, 3$



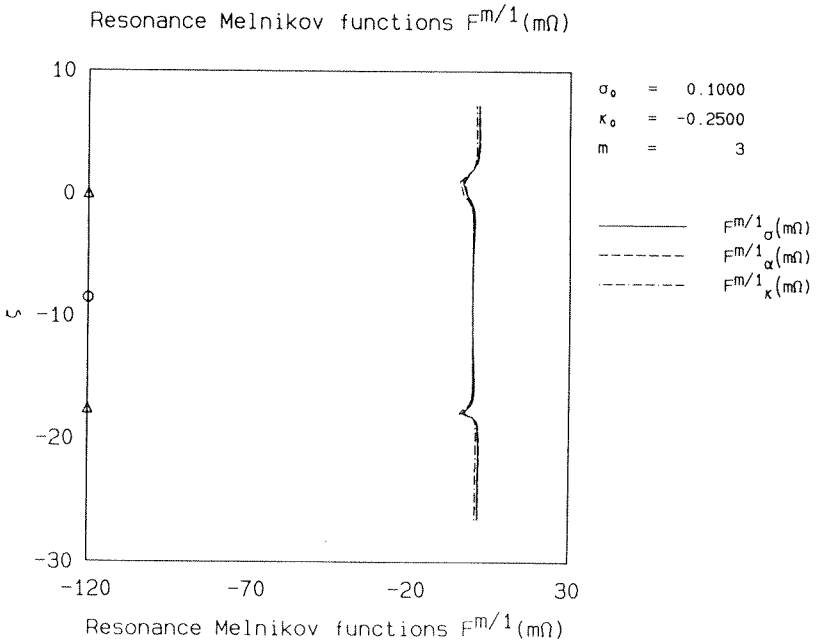
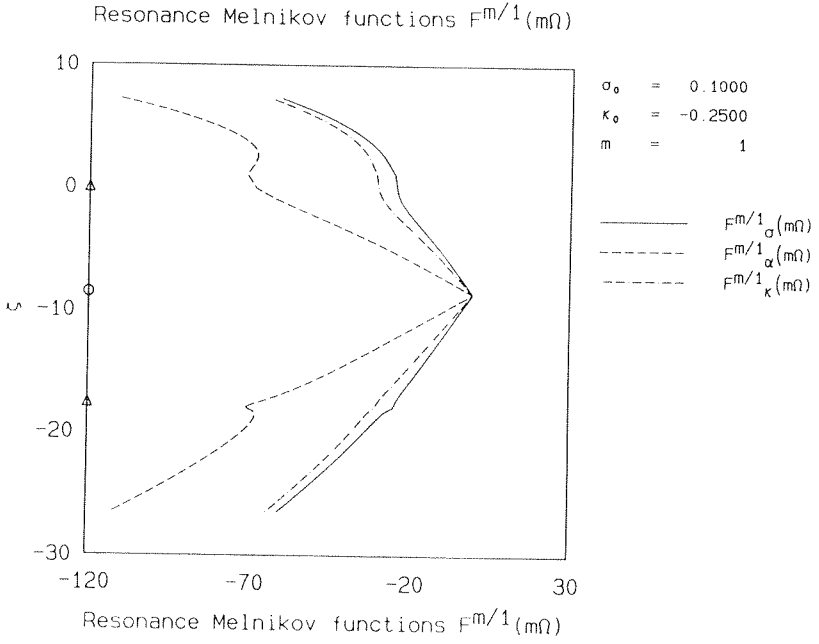
(κ_0, σ_0) in 5^+ for $m = 1, 3$



(κ_0, σ_0) in 13^+ for $m = 1, 3$



(κ_0, σ_0) in 15^+ for $m = 1, 3$



(κ_0, σ_0) in 17^+ for $m = 1, 3$

Region in (κ_0, σ_0)	Some typical UEV motion and mechanisms
1	<ul style="list-style-type: none"> • (C-C) osc on $RB \frac{m}{1}$, KAM, <i>can</i> • transition between (C-C) osc. and rot if $RB \frac{m}{1}$ includes the origin of (δ, ζ) • (C-C) osc on RB^m_T, KAM, <i>can</i>
3	<ul style="list-style-type: none"> • (C-C) osc on $RB \frac{m}{1}$, KAM, <i>can</i> • transition between (C-C) osc. and rot if $LRB \frac{m}{1}$ includes the origin of (δ, ζ) • (C-C) osc on $RB \frac{m}{1}$, KAM, <i>can</i> • transition between (C-C) rot. and irreversible elongation through homoclinic tangles • chaotic (C-C) rot. along horseshoe map
near 4	<ul style="list-style-type: none"> • (C-C) osc on $RB \frac{m}{1}$, KAM, <i>can</i> • transition between (C-C) osc. and irreversible elongation through homoclinic tangles • chaotic (C-C) osc and rot. along horseshoe map
5	<ul style="list-style-type: none"> • (C-C) osc on $RB \frac{m}{1}$, KAM, <i>can</i> • transition between (C-C) osc. and irreversible elongation through homoclinic tangles • chaotic (C-C) osc. along horseshoe map
13	<ul style="list-style-type: none"> • (C-C) osc on $RB \frac{m}{1}$, KAM, <i>can</i> • transition between (C-C) osc. and rot if $RB \frac{m}{1}$ includes the origin of (δ, ζ) • (C-C) osc on $RB \frac{m}{1}$, KAM, <i>can</i> • (C) osc on $RB \frac{m}{1}$, KAM, <i>can</i> • (C) rot on $RB \frac{m}{1}$, KAM, <i>can</i> • transition between (C-C) rot, (C) osc, and (C) rot. through inner and outer homoclinic tangles • chaotic (C-C) osc, (C) osc., and (C) rot along horseshoe map
14	<ul style="list-style-type: none"> • (C-C) osc on $RB \frac{m}{1}$, KAM, <i>can</i> • (C-C) osc on $RB \frac{m}{1}$, KAM, <i>can</i> • transition between (C-C) osc., (C) osc., and (C) rot. through inner and outer homoclinic tangles • chaotic (C-C) osc., (C) osc., and (C) rot. along horseshoe map
15	<ul style="list-style-type: none"> • (C-C) osc on $RB \frac{m}{1}$, KAM, <i>can</i> • (C) osc on $RB \frac{m}{1}$, KAM, <i>can</i> • transition between (C-C) osc. and (C) rot. if $RB \frac{m}{1}$ includes the origin of (δ, ζ) • (C) rot on $RB \frac{m}{1}$, KAM, <i>can</i> • transition between (C-C) osc. and (C) rot. through inner and outer homoclinic tangles • chaotic (C-C) osc. and (C) rot. along horseshoe map
17	<ul style="list-style-type: none"> • (C) osc. on $RB \frac{m}{1}$, KAM, <i>can</i> • transition between (C) rot. and (C) rot. if $RB \frac{m}{1}$ includes the origin of (δ, ζ) • (C) rot on RB^m_T, KAM, <i>can</i>

Table 4.1 Possible UEV motions in unsteady external flow field for (κ_0, σ_0) and thier mechanism

Chapter 5

PARTICLE MOTION

In this section we study the fluid particle motion in the velocity field induced by a UEV in a steady linear velocity field. We compare our results with a study of the fluid particle motions in the velocity field induced by a point vortex in both steady and time periodic velocity fields. This will give us an idea of the effect of the finite core size of a UEV on the mixing of fluid. In other words, a finite core size vortex works as a mixer in the flow field. In particular, we will study fluid particle motion in the following four velocity fields.

1. Flow field induced by a point vortex in a steady external linear velocity field (steady PV system).
2. Flow field induced by a stable steady UEV in a steady external linear velocity field (steady UEV system).
3. Flow field due to a point vortex in a time-periodic external linear velocity field (unsteady PV system).
4. Flow field due to a UEV undergoing periodic motion in a steady external linear velocity field (unsteady UEV system).

5.1 The equations of motion governing the flow field

The total velocity field, in complex variables, induced by point vortex or UEV in an external linear velocity field can be written as a superposition of each velocity field as shown in Chapter 2. First, we begin with an appropriate nondimensionalization of the system so as to facilitate comparisons. In order to nondimensionalize

the system, we use the following scaling of variables since a PV itself does not have any length scale.

$$(z, t) \longmapsto (\hat{z}, \hat{\tau}) = \left(z / \sqrt{\frac{\Gamma}{2\pi\gamma_0}}, \gamma_0 t \right), \quad (5.1)$$

where $\gamma_0 > 0$ is the strength of the basic external straining field and $\sqrt{\frac{\Gamma}{2\pi\gamma_0}}$ is the distance between a PV and one of the stagnation points in the flow with $\omega_R = 0$ as we will see later. Note that the transformation given by Eqn. (5.1) is singular at $\gamma_0 = 0$ due to the lack of any length scale in the system. The equations of fluid particle motion for a PV system shown in Chapter 2 are written in the normalized variables as follows (henceforth neglecting the ‘^’ on z and τ)

$$\begin{aligned} \frac{d}{d\tau} z^* &= \frac{1}{iz} + \bar{\gamma} e^{-2i\alpha} z + \frac{\bar{\beta}}{2i} z^* = h_{PV}(z, z^*; \bar{\gamma}, \alpha, \bar{\beta}) \\ &= \frac{\partial}{\partial z} f_{PV} = \frac{\partial}{\partial z} (\phi_{PV} + i\psi_{PV}), \end{aligned}$$

where

$$\begin{aligned} f_{PV} &= f_p + f_s + f_r \\ f_p &= 1/i \log z \\ f_s &= \frac{\bar{\gamma}}{2} e^{-2i\alpha} z^2 \\ f_r &= \frac{\bar{\beta}}{4i} z^* z \\ \bar{\gamma} &= \frac{\gamma}{\gamma_0} \\ \bar{\beta} &= \frac{\omega_R}{\gamma_0} = \frac{\kappa}{\sigma_0}, \end{aligned} \quad (5.2)$$

where the subscripts ‘PV’, ‘p’, ‘s’ and ‘r’ stand for ‘PV system’, ‘point vortex’, ‘straining effect’ and ‘background vorticity effect’ respectively. The f ’s are the normalized complex stream function $f = \phi + i\psi$, where ϕ and ψ are potential and stream functions, respectively, and $\bar{\gamma}$ and $\bar{\beta}$ are the normalized straining rate and background vorticity rate nondimensionalized by γ_0 , respectively.

Similarly, the equations of fluid particles for motion of a UEV system in the normalized variables are as follows.

$$\begin{aligned} \frac{d}{d\tau} z^* &= \frac{2}{i\bar{D}e^{2i\theta}} (z - \sqrt{z^2 - \bar{D}e^{2i\theta}}) + \bar{\gamma} e^{-2i\alpha} z + \frac{\bar{\beta}}{2i} z^* \\ &= h_{UEV}(z, z^*, \bar{\gamma}, \alpha, \bar{\beta}; \eta, \theta; \bar{\Lambda}) \\ &= \frac{\partial}{\partial z} f_{UEV} = \frac{\partial}{\partial z} (\phi_{UEV} + i\psi_{UEV}), \end{aligned}$$

where

$$\begin{aligned}
 f_{UEV} &= f_E + f_s + f_r \\
 f_E &= \frac{2}{i} \log(z + \sqrt{z^2 - \bar{D}e^{2i\theta}}) + \frac{2}{i\bar{D}e^{2i\theta}} \left\{ z^2 - z\sqrt{z^2 - \bar{D}e^{2i\theta}} - \frac{\bar{D}}{2}e^{2i\theta} \right\} \\
 \bar{D} &= \frac{\eta^2 - 1}{\eta} \bar{\Lambda}^2 \\
 \bar{\Lambda} &= \Lambda / \sqrt{\frac{\Gamma}{2\pi\gamma_0}},
 \end{aligned} \tag{5.3}$$

where the subscript ‘UEV’ stands for ‘UEV system’ and $\bar{\Lambda}$ is the normalized UEV core radius and $\eta(\tau)$, $\theta(\tau)$ are obtained from Eqn. (2.7). Recall that the basic external linear velocity field was described by two parameters (κ_0, σ_0) in Chapters 2, 3 and 4. Here, the basic external velocity field is described by an alternate set of parameters $(\bar{\beta}_0, \bar{\Lambda})$, where $\bar{\beta}_0 = \frac{\kappa_0}{\sigma_0}$ is the ratio of basic external background vorticity to straining rate. For a PV system, $\bar{\Lambda} = 0$ and hence $\bar{\beta}_0$ is the only parameter. Note that the two sets of parameters (σ_0, κ_0) and $(\bar{\beta}_0, \bar{\Lambda})$ can be related as follows.

$$\begin{aligned}
 \sigma_0 &= \gamma_0 / \frac{\Gamma}{\pi\Lambda^2} = 2\bar{\Lambda}^2 \\
 \kappa_0 &= \bar{\beta}_0\sigma_0 = 2\bar{\beta}_0\bar{\Lambda}^2.
 \end{aligned} \tag{5.4}$$

Notice that the straining rate is proportional to $\bar{\Lambda}^2$, i.e., the area of the UEV. Hence, the larger core size UEV receives stronger influence from the external linear flow field. We remark that for a given $(\bar{\beta}_0, \bar{\Lambda})$, the UEV dynamics is completely understood from Chapter 3 and, moreover, we can always find a stable, steady UEV configuration, (i.e., a fixed point of Eqn. (2.7)) provided the corresponding (σ_0, κ_0) does not belong to region 7⁺ of the bifurcation diagram in Fig. 3.5. Also, note from Eqns. (5.2) and (5.3) that the total velocity field is expressed as a sum of three parts, i.e., a part due to a PV or UEV, a part due to the external straining flow and a part due to the external rotational flow. The reader should note that this is similar to the composition of the ordinary differential equations governing the motion of the UEV derived in Chapter 2.

5.2 The Steady Flow Fields

We next describe the fluid particle motion in the steady external flow fields, First we consider a steady PV system. Eqn. (5.2) in the polar coordinate (r, χ) where $z = re^{i\chi}$, is written as follows.

$$\begin{aligned} \frac{d}{d\tau}r &= \bar{\gamma}_0 r \cos 2(\chi - \alpha_0) \\ \frac{d}{d\tau}\chi &= \frac{1}{r} - \bar{\gamma}_0 \sin 2(\chi - \alpha_0) + 2\bar{\beta} , \end{aligned}$$

where $\bar{\gamma}_0 = 1$ and $\alpha_0 = 0$ for a steady external flow field. Near the PV, the flow field is strongly governed by the PV, and hence the fluid particles rotate in a counterclockwise direction around the PV. In the far field (i.e., $r \rightarrow \infty$), the external flow field effect becomes dominant. For $\bar{\beta}_0 > \frac{1}{2}$ ($\bar{\beta}_0 < \frac{-1}{2}$ resp.), $\frac{d}{d\tau}\chi$ is positive (negative resp.) for any (r, χ) , meaning that a fluid particle in the far field undergoes counter-clockwise (clockwise resp.) periodic motion while the distance from the PV to the particle fluctuates due to the straining effect. For $|\bar{\beta}_0| < \frac{1}{2}$, the straining effect overcome the background vorticity effect and the fluid particles drift from infinity along the contraction axis χ_c and to infinity along the stretching axis χ_s ,

$$\begin{aligned} \chi_s &= \frac{1}{2} \sin^{-1} 2\bar{\beta}_0 \\ \chi_c &= \frac{\pi}{2} - \frac{1}{2} \sin^{-1} 2\bar{\beta}_0 . \end{aligned}$$

As a consequence, the far field is divided into four regions by dividing stream lines which correspond to the contraction and stretching axes. Recall that the motion of the UEV exhibits similar behaviors, i.e., the UEV undergoes periodic motion (irreversible elongation resp.) when the background vorticity effect (the straining effect resp.) governs the external linear flow field.

Since this is a steady two-dimensional incompressible flow, the fluid particles follow the level sets of the stream function ψ . By solving Eqn. (5.2), we obtain three geometrically distinct flow field structures depending on $\bar{\beta}_0$ as follows (See Fig. 5.1).

$\bar{\beta}_0 > 1/2$ ($\sigma_0 > \kappa_0/2$): The counterclockwise background vorticity effect dominates the far field flow. All fluid particles rotate counterclockwise around the

PV. The period of the rotation along the inner closed streamlines is shorter than the period along the outer streamlines, see Fig. 5.1a.

$|\bar{\beta}_0| < 1/2$ ($|\sigma_0| > \kappa_0/2$): The straining effect dominates the flow in the far field. As a consequence, the flow domain is divided into five regions by some dividing streamlines. In the core region which is bounded by two dividing streamlines connecting two stagnation points at $(r, \chi) = \left(\sqrt{\frac{2\bar{\beta}_0}{2\bar{\beta}_0-1}}, \frac{\pi}{4}\right)$ and $\left(\sqrt{\frac{2\bar{\beta}_0}{2\bar{\beta}_0-1}}, \frac{5\pi}{4}\right)$ where (r, χ) is the polar coordinate (i.e., $z = re^{i\chi}$), a fluid particle undergoes counterclockwise periodic rotation around the PV. In the four regions outside of the core, fluid particles drift to infinity along the dividing streamlines $\chi_s = \frac{1}{2} \sin^{-1} 2\bar{\beta}_0$ ($r \rightarrow \infty$) due to the straining effect, see Fig. 5.1b.

$\bar{\beta}_0 < -1/2$ ($\sigma_0 < -\kappa_0/2$): In the far field, the clockwise background vorticity effect governs the flow and fluid particles undergo clockwise rotation. The flow domain is divided into four regions by four dividing stream lines as shown in Fig. 5.1c, i.e., the core, the far field and two intermediate regions. In each intermediate region, fluid particles undergo clockwise periodic rotation around a stagnation point at $(r, \chi) = \left(\sqrt{\left|\frac{\bar{\beta}_0}{2\bar{\beta}_0+1}\right|}, \frac{3\pi}{4}\right)$ or $\left(\sqrt{\left|\frac{\bar{\beta}_0}{2\bar{\beta}_0+1}\right|}, \frac{7\pi}{4}\right)$. Note that the boundaries of the four regions are defined by four heteroclinic orbits connecting two stagnation points at $(r, \chi) = \left(\sqrt{\frac{2\bar{\beta}_0}{2\bar{\beta}_0-1}}, \frac{\pi}{4}\right)$ and $\left(\sqrt{\frac{2\bar{\beta}_0}{2\bar{\beta}_0-1}}, \frac{5\pi}{4}\right)$, see Fig. 5.1c.

Next we consider a steady UEV system. The streamline structures are topologically similar to the structures for a steady PV system for various $\bar{\beta}_0$ values with $\bar{\Lambda}$ small enough. We say that the UEV core is small enough if the stagnation points exist exterior to the core. Notice that, for a given $\bar{\beta}_0$, the geometrical structure of the stream lines is topologically equivalent to that of a PV system. This is a direct result from Eqn.(5.3), however, it can also be justified from the following facts. As we have seen in Chapter 3, a steady UEV can only exist for $\theta = \frac{\pi}{4}$ or $\frac{3\pi}{4}$ depending on (σ_0, κ_0) , i.e., $(\bar{\beta}_0, \bar{\Lambda})$. The velocity field exterior to a UEV is very similar to that of a PV, i.e., it decays like $1/r$ as $r \rightarrow \infty$. Hence, the external flow field governs the far field flow structure as well as the steady PV system. Since two velocity fields induced by the PV and the UEV agree on the extended semi-major and semi-minor axes of the UEV which are either on $\chi = \frac{\pi}{4}, \frac{5\pi}{4}$ or $\frac{3\pi}{4}, \frac{7\pi}{4}$ for a steady UEV system,

the stagnation points in the flow on $\chi = \frac{\pi}{4}, \frac{5\pi}{4}, \frac{3\pi}{4}, \frac{7\pi}{4}$ exist at the same positions with the same stability type for both systems. This means that as long as the stagnation points exist exterior to the UEV core, the qualitative flow structures for a given $\bar{\beta}_0$ are topologically equivalent.

5.3 The Unsteady Flow Fields

When the total flow field is time periodic, the flow structure may exhibit new types of motion. In the PV system, the time periodic perturbation is due to the time periodic perturbation in the external linear flow field which may have arbitrary frequency. In a UEV system, the time periodic motion of the UEV in the steady external flow field induces a time periodic perturbation for a given external flow field $(\bar{\beta}_0, \bar{\Lambda})$ and UEV initial configuration $(\eta(\tau_0), \theta(\tau_0))$. In this case the perturbation frequency is uniquely determined, and, therefore, cannot be arbitrary. We use the same technique as in Chapter 4 to study the unsteady flow dynamics, however the physical implications of those techniques are different.

5.3.1 Qualitative flow dynamics

The Poincaré map enables us to better understand the unsteady time periodic flow dynamics. We examine how the flow dynamics changes under the time periodic perturbation. Note that, qualitatively speaking, the PV system and the UEV system exhibit the same types of flow dynamics. Typically, the heteroclinic orbits which define the boundaries of unperturbed flow regions break up and result in a region of chaotic fluid particle motion. The mechanisms for these dynamics are as follows. In the mixing region, lobe dynamics, which we described earlier, can be used to describe the transport process and to compute residence time distributions, as we will demonstrate later. There also exists chaotic particle motion in the mixing region associated with horseshoe maps. In Fig. 5.2, the typical heteroclinic tangle structures for $|\bar{\beta}_0| < \frac{1}{2}$ and $\bar{\beta}_0 < \frac{-1}{2}$ are shown.

For fluid particles which undergo periodic rotation along the invariant circles in the steady flow, the rotation number $\rho = \frac{\Omega^H}{\Omega}$, where Ω is the perturbation frequency and Ω^H is the frequency of the unperturbed periodic orbit, governs the

perturbed dynamics. When ρ is rational, i.e., $\rho = \frac{m}{n}$ where m and n are relatively prime integers, the invariant circle breaks up and forms a resonance band consisting of $2m$ periodic fluid particle motions equally distributed around the circle which alternate in stability type between elliptic and hyperbolic. The resonance band, which possesses heteroclinic tangles due to the unstable and stable manifolds of the hyperbolic period m points, allows fluid passage through the resulting lobe dynamics. Moreover, there exists chaotic dynamics along the resonance band associated with horseshoe maps. On the other hand, the invariant circle may persist under the perturbation as a KAM torus when ρ is irrational. KAM tori are extremely important since they represent total barriers to fluid motion. When ρ is irrational and fails to satisfy the condition for KAM tori, then the invariant circle may partly break down and contain small gaps which permit very slow fluid passage. These motions are referred to as cantori.

5.3.2 The Melnikov technique on heteroclinic orbits

The Melnikov techniques for the heteroclinic tangle and the resonance band again provide insightful information regarding the fluid particle motion.

First we consider the unsteady PV system where the external flow parameters are perturbed sinusoidally.

$$\begin{aligned}\bar{\gamma}(\tau) &= 1 + \epsilon_\gamma \sin \Omega(\tau + \tau_\gamma) \\ \alpha(\tau) &= \epsilon_\alpha \sin \Omega(\tau + \tau_\alpha) \\ \bar{\beta}(\tau) &= \bar{\beta}_0(1 + \epsilon_\beta \sin \Omega(\tau + \tau_\beta)) ,\end{aligned}$$

where τ_γ, τ_α and τ_β describe phase shifts in each perturbation. The total Melnikov function is a composition of three effects, i.e.,

$$M(\tau_0) = \epsilon_\gamma M_{\epsilon_\gamma}(\tau_0) + \epsilon_\alpha M_{\epsilon_\alpha}(\tau_0) + \epsilon_\beta M_{\epsilon_\beta}(\tau_0) .$$

We now give the physical insight of the Melnikov function for each perturbation. First we consider the perturbations in $\bar{\gamma}(\tau)$ and $\bar{\beta}(\tau)$. Eqn. (5.2) can be written in

two real variables x and y associated with the stream function as follows.

$$\begin{aligned}\frac{d}{d\tau}x &= \frac{\partial}{\partial y}(\psi_p + \bar{\gamma}\bar{\psi}_s + \bar{\beta}\bar{\psi}_r) \\ \frac{d}{d\tau}y &= -\frac{\partial}{\partial x}(\psi_p + \bar{\gamma}\bar{\psi}_s + \bar{\beta}\bar{\psi}_r),\end{aligned}$$

where

$$\begin{aligned}\psi_s &= \bar{\gamma}\bar{\psi}_s \\ \psi_r &= \bar{\beta}\bar{\psi}_r.\end{aligned}$$

Notice that the perturbations in $\bar{\gamma}$ and $\bar{\beta}$ have the form of Hamiltonian perturbations of Type 1 which we discussed in Chapter 4. Hence, the Melnikov functions $M_\gamma(\tau_0)$ and $M_\beta(\tau_0)$ for the both perturbation types are written as follows.

$$\begin{aligned}M_\gamma(\tau_0) &= \int_{-\infty}^{\infty} \frac{d}{d\tau}\bar{\psi}_s \sin \Omega(\tau + \tau_\gamma + \tau_0) d\tau \\ &= F_\gamma \cos \Omega(\tau_0 + \tau_\gamma) \\ M_\beta(\tau_0) &= \bar{\beta}_0 \int_{-\infty}^{\infty} \frac{d}{d\tau}\bar{\psi}_R \sin \Omega(\tau + \tau_\beta + \tau_0) d\tau \\ &= F_\beta \cos \Omega(\tau_0 + \tau_\beta),\end{aligned}\tag{5.5}$$

where

$$\begin{aligned}F_\gamma &= \int_{-\infty}^{\infty} \left(\frac{d}{d\tau}\bar{\psi}_s\right) \sin \Omega\tau d\tau \\ F_\beta &= \bar{\beta}_0 \int_{-\infty}^{\infty} \left(\frac{d}{d\tau}\bar{\psi}_r\right) \sin \Omega\tau d\tau.\end{aligned}$$

From Eqn. (5.5), $M_\gamma(\tau_0)$ and $M_\beta(\tau_0)$ relate to the Fourier transform of the rate of change in the corresponding stream functions along the unperturbed heteroclinic orbit. Note that F_γ and F_β are linear in the basic flow parameter $\bar{\beta}_0$, and $\bar{\psi}_s$ and $\bar{\psi}_R$ are independent of $\bar{\beta}_0$. Hence the behaviors of F_γ and F_β with respect to the perturbation frequency are strongly governed by the geometrical structure of the unperturbed heteroclinic orbit in relation to $\bar{\phi}_s$ and $\bar{\phi}_r$. Physically it means that the flow dynamics in the mixing region are determined by how much influence a fluid particle receives from the steady part of the perturbed external flow field as the fluid particle drifts on the dividing stream line of the steady flow field. For example, consider the rate of change of the external straining stream function on the heteroclinic orbit for $0 < \bar{\beta}_0 < \frac{1}{2}$ which connects two stagnation points on

$\chi = \frac{\pi}{4}$ and $\frac{5\pi}{4}$. On the orbit, $\frac{d}{d\tau}\psi_s < 0$ for $\chi < \frac{3\pi}{4}$ (i.e., $\tau < 0$ by taking $\tau = 0$ on $\chi = \frac{3\pi}{4}$), $\frac{d}{d\tau}\psi_s > 0$ for $\chi > \frac{3\pi}{4}$ (i.e., $\tau > 0$), and $|\frac{d}{d\tau}\psi_s|$ decays exponentially as the orbit approaches stagnation points (i.e., $\tau \rightarrow \pm\infty$.) Similarly, the rate of change of the external background vorticity stream function on the heteroclinic orbit is such that $\frac{d}{d\tau}\psi_R < 0$ for $\chi < \frac{3\pi}{4}$ (i.e., $\tau < 0$), and $\frac{d}{d\tau}\psi_R > 0$ for $\chi > \frac{3\pi}{4}$ (i.e., $\tau > 0$) and $|\frac{d}{d\tau}\psi_R|$ decays exponentially as the orbit approaches stagnation points (i.e., $\tau \rightarrow \pm\infty$.) Hence we can infer that the graphs of F_γ and F_β versus the perturbation frequency Ω show the typical behavior, i.e., $|F_\gamma|$ and $|F_\beta|$ have the global maximal at their first local maximum and decay exponentially as Ω goes to infinity.

For understanding the physical implication of $M_\alpha(\tau_0)$, we use the following canonical transformation of variables which we used in Chapter 2 for the UEV motion.

$$(x, y) \rightarrow (R, \chi) ,$$

where

$$R = \frac{r}{2} = \frac{x^2 + y^2}{2}$$

Then the equations of motion given by Eqn. (5.2) are written in another Hamiltonian formulation.

$$\begin{aligned} \frac{d}{d\tau}R &= -\frac{\partial}{\partial\chi}(\psi_p + \psi_s + \psi_r) \\ &= \bar{\gamma}\sqrt{2R}\cos 2(\chi - \alpha) \\ \frac{d}{d\tau}\chi &= \frac{\partial}{\partial R}(\psi_p + \psi_s + \psi_r) \\ &= \frac{1}{\sqrt{2R}} - \bar{\gamma}\sin 2(\chi - \alpha) + 2\bar{\beta} , \end{aligned}$$

where

$$\begin{aligned} \psi_p &= \sqrt{2R} \\ \psi_s &= -\bar{\gamma}\sin 2(\chi - \alpha) \\ \psi_r &= 2\bar{\beta}R . \end{aligned}$$

The reader should notice that the perturbation in $\alpha(\tau)$ is a Hamiltonian perturbation of Type 2 which we discussed in Chapter 4. Therefore, the Melnikov function is written

$$\begin{aligned} M_\alpha(\tau_0) &= \int_{-\infty}^{\infty} \left(\frac{d^2}{d\tau^2}R\right) \sin \Omega(\tau + \tau_\alpha + \tau_0) d\tau \\ &= F_\alpha \sin \Omega(\tau_0 + \tau_\alpha) , \end{aligned} \tag{5.6}$$

where

$$F_\alpha = \int_{-\infty}^{\infty} \left(\frac{d^2}{d\tau^2} R \right) \cos \Omega \tau d\tau .$$

From Eqn. (5.6), $M_\alpha(\tau_0)$ relates to the Fourier transform of the second derivative of $R = \frac{r}{2}$ with respect to time where r is the distance from the PV. Furthermore, one can show following relation between F_α and F_β ,

$$\bar{\beta}_0 F_\alpha = \Omega F_\beta ,$$

i.e., the ratio of F_α and F_β is proportional to perturbation frequency Ω and inversely proportional to the basic external flow parameter $\bar{\beta}_0$. Notice that $\alpha(\tau)$ is the inclination angle of the straining axis, and $\bar{\beta}(\tau)$ is the background vorticity rate normalized by the straining effect, and hence both $\alpha(\tau)$ and $\beta(\tau)$ are related to the angular velocity component of the fluid particle. The behavior of the graph of F_α can be inferred from the relation to F_β or the geometrical structure of the unperturbed orbit.

Finally, the total Melnikov function is a superposition of three effects.

$$\epsilon M(\tau; \beta_0; \Omega) = F_{tot}(\beta_0; \Omega) \sin \Omega(\tau_0 + \tau_{tot}) ,$$

where

$$\begin{aligned} F_{tot} &= \{(c_\gamma + c_\alpha + c_\beta)^2 + (s_\gamma + s_\alpha + s_\beta)^2\}^{\frac{1}{2}} \\ \tau_{tot} &= \frac{1}{\Omega} \tan^{-1} \frac{s_\gamma + s_\alpha + s_\beta}{c_\gamma + c_\alpha + c_\beta} . \end{aligned} \tag{5.7}$$

with

$$\begin{aligned} s_i &= |\epsilon_i F_i(\beta_0; \Omega)| \sin \Omega(\tau_0 + \tau_i) \\ c_i &= |\epsilon_i F_i(\beta_0; \Omega)| \cos \Omega(\tau_0 + \tau_i) \\ i &= \gamma, \alpha, \beta. \end{aligned}$$

When the external linear flow is excited in more than one parameter, they may excite or cancel each other. The phase shift parameters have an important influence on the total flow dynamics because with proper phase shift, F_{tot} can be identically zero from Eqn. (5.7).

In Fig. 5.3, the graphs of F_γ and F_α are plotted versus perturbation frequency Ω for $\beta_0 = 0$ (i.e., $\kappa_0 = 0$). The effects of the perturbation frequency Ω on the

graphs of F_γ and F_β are as follows. F_γ increases in proportion to Ω for Ω small, attains the first local and global maximum at the extremum frequency $\Omega_\gamma^e \simeq 3$, and decays exponentially as Ω goes to infinity. F_α increases in proportion to Ω^2 for Ω small, attains the first local and global maximum at the extremum frequency $\Omega_\alpha^e \simeq 2$, and decays exponentially as Ω goes to infinity. The area of a lobe is plotted in Fig. 5.4 with $\epsilon_\gamma = \epsilon_\beta = 0.1$.

Next we consider the unsteady UEV system. However, in order to apply the Melnikov technique for the unsteady UEV system, we need to introduce the modified Melnikov function which has a slightly different form from the regular Melnikov function. One of the main reasons for using the modified Melnikov function is that the equations of motion for the unsteady UEV can not easily be written as a system of two real variables. The regular Melnikov function can be computed using the averaging method (Holmes and Holmes [1978]), however, the modified Melnikov function gives more simpler and insightful form of the function. See Appendix 7 for detailed proof.

We define the modified Melnikov function $M_\epsilon(\tau_0)$ on the heteroclinic orbit as follows.

$$M_\epsilon(\tau_0) = -Im \int_{-\infty}^{\infty} \frac{d}{d\tau} z_0^* \frac{d}{d\tau} z(z_h(\tau), \tau + \tau_0) d\tau , \quad (5.8)$$

where τ_0 is the parametrization variable on the unperturbed heteroclinic orbit $z_h(\tau)$ as we defined before, $\frac{d}{d\tau} z_0^*$ describes the conjugate of the unperturbed velocity as a complex variable, $\frac{d}{d\tau} z$ describes the perturbed velocity and the integrand is evaluated on the unperturbed heteroclinic orbit. Then $M_\epsilon(\tau_0)$ is $O(\epsilon)$, where ϵ is the order of the perturbation, and it is the first order term of the signed distance $d(\tau_0, \epsilon)$ between unstable and stable manifolds which form the heteroclinic tangle, up to a known normalization factor, i.e.,

$$d(\tau_0, \epsilon) = \frac{M_\epsilon(\tau_0)}{\left\| \frac{d}{d\tau} z_0^*(z_h(-\tau_0)) \right\|} + O(\epsilon^2) .$$

For a system which can be written in a form so as to compute the regular Melnikov function, $M(\tau_0)$, $M_\epsilon(\tau_0)$ has the following relation to $M(\tau_0)$

$$M_\epsilon(\tau_0) = \epsilon M(\tau_0) + O(\epsilon^2) .$$

It follows from the Melnikov theorem that the simple zeroes of $M_\epsilon(\tau_0)$ (i.e., $M_\epsilon(\tau_0) = 0$ and $\frac{\partial}{\partial \tau_0} M_\epsilon(\tau_0) \neq 0$) imply the transverse intersection of two manifolds. As a consequence, the modified Melnikov function $M_\epsilon(\tau_0)$ gives the number of transverse intersections per perturbation cycle.

Now let us examine Eqn. (5.8) for the physical implication of the modified Melnikov function. The integrand $Im \left\{ \frac{d}{d\tau} z_0^* \frac{d}{d\tau} z \right\}$ corresponds to the out-of-phase component of the perturbed velocity projected down to the unperturbed velocity. Again, the perturbation frequency is an important factor of the modified Melnikov function as well as the amplitude of the perturbation. It is clear that if no perturbation is imposed, i.e., $\frac{d}{d\tau} z = \frac{d}{d\tau} z_0$, then $Im \left\{ \frac{d}{d\tau} z_0^* \frac{d}{d\tau} z \right\} = 0$, meaning that $M_\epsilon(\tau_0) = 0$.

Using the modified Melnikov function, we can compute the area of each lobe A_ϵ up to the first order in ϵ as well as the regular Melnikov function.

$$A_\epsilon = \left| \int_{\tau_1}^{\tau_2} M_\epsilon(\tau_0) d\tau_0 \right| + O(\epsilon^2), \quad (5.9)$$

where τ_1 and τ_2 are the parametrization variables corresponding to two adjacent pip.

Now let us apply the modified Melnikov function on the heteroclinic orbit to examine how the finite core size UEV contributes to the chaotic mixing in the flow field in comparison to the unsteady PV system. For a given $(\bar{\beta}_0, \bar{\Lambda}) = \left(\frac{\kappa_0}{\sigma_0}, \sqrt{\frac{\sigma_0}{2}} \right)$, the period of the motion is uniquely determined by the UEV configuration. Here we choose $\bar{\beta}_0 = 0$ and describe how the chaotic transport is influenced by the finite core effect and initial UEV configuration using the modified Melnikov function and the area of a lobe. The area of a lobe defines the size of the mixing region and it shows how much fluid is transported across the boundary between two or more distinct flow regions. The modified Melnikov function is given as follows.

$$M_\epsilon(\tau_0) = -Im \int_{-\infty}^{\infty} \frac{d}{d\tau} z_0^* \frac{d}{d\tau} z(z_h(\tau), \tau + \tau_0) d\tau,$$

where

$$\begin{aligned} \frac{d}{d\tau} z_0^* &= \frac{2}{i\bar{D}_0 e^{2i\theta_0}} (z - \sqrt{z^2 - \bar{D}_0 e^{2i\theta_0}}) + z + \frac{\bar{\beta}_0}{2i} z^* \\ \frac{d}{d\tau} z &= \frac{2}{i\bar{D} e^{2i\theta}} (z - \sqrt{z^2 - \bar{D} e^{2i\theta}}) + z + \frac{\bar{\beta}_0}{2i} z^*. \end{aligned}$$

The subscript ‘ $_0$ ’ for \bar{D} and θ denotes the stable steady UEV configuration. Since the perturbation is given by $(\eta(\tau), \theta(\tau))$, and hence the time dependence of the perturbation does not appear explicitly. The result is that $M_\epsilon(\tau_0)$ is implicit in τ_0 . However, the area of each lobe does not depend on τ_0 by definition from Eqn. (5.9). In order to examine the finite core effects of the UEV, we compare the area of a lobe for the unsteady PV system and the unsteady UEV system. A_ϵ are computed for $\beta_0 = 0$ and several $\bar{\Lambda}$ values, i.e., $(\bar{\beta}, \bar{\Lambda}) = (0, 0.245), (0, 0.316)$ and $(0, 0.374)$ which correspond to $(\sigma_0, \kappa_0) = (0.03, 0), (0.05, 0)$ and $(0, 0.07)$ respectively. Furthermore, for each core radius $\bar{\Lambda}$, five initial UEV configurations, which correspond to periodic oscillation of UEV are chosen to examine the perturbation amplitude effects.

$$(\eta_i, \theta_i) = (1 + c(\eta_0 - 1), \frac{\pi}{4})$$

$$c \in (0, 1] ,$$

where (η_i, θ_i) is the initial UEV configuration, η_0 is the aspect ratio for the stable steady UEV, c is a parameter which controls the perturbation amplitude. $c = 0$ corresponds to a steady stable UEV (i.e., the steady UEV system) and $c = 1$ corresponds to a UEV undergoing critical boundary motion between oscillation and rotation as we discussed in Chapter 3. Here, we chose $c = 0.1, 0.3, 0.5, 0.7, 0.9$. The result is shown in Fig. 5.5 in comparison to the result from the unsteady PV system. Notice that for a given core size $\bar{\Lambda}$, the period of the oscillation is insensitive to the initial UEV configuration. Hence, we first discuss the effect of the perturbation amplitude for a given core radius $\bar{\Lambda}$. If the UEV undergoes oscillation with larger amplitude perturbation (i.e., c larger), then the area of a lobe is larger meaning that the size of the mixing region is bigger. The period of the UEV motion strongly depends on $\bar{\Lambda}$. The larger core UEV undergoes periodic motion with lower frequency, and as the core radius approaches zero (i.e., the PV), the perturbation frequency goes to infinity. Fig. 5.6 shows that the larger core radius UEV with bigger perturbation from the steady configuration generates a larger mixing region. The regular motion of a finite core UEV in a steady external linear flow field creates a chaotic mixing region, i.e., a UEV works as a mixer in the flow field. The initial configuration and core size have a significant effect in the flow field.

5.4 Figures for Chapter 5

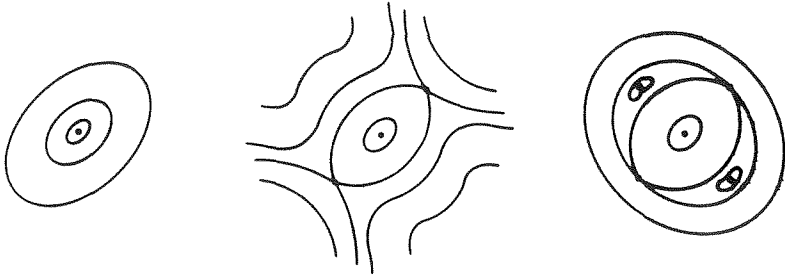


Figure 5.1 Stream line structures for a steady PV system
(a) $\beta_0 > 1/2$ (b) $|\beta_0| < 1/2$ (c) $\beta_0 < -1/2$

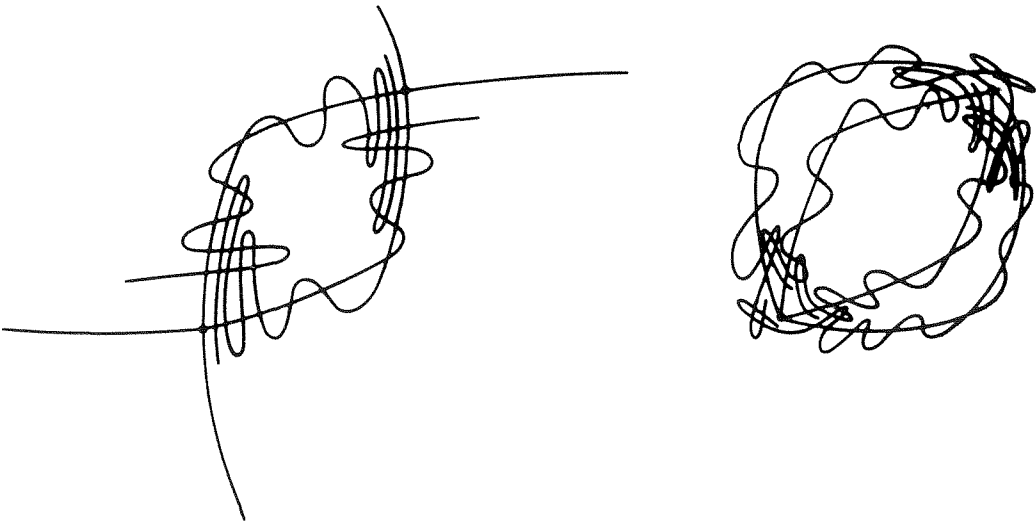


Figure 5.2 heteroclinic tangles
(a) $|\beta_0| < 1/2$ (b) $\beta_0 < -1/2$

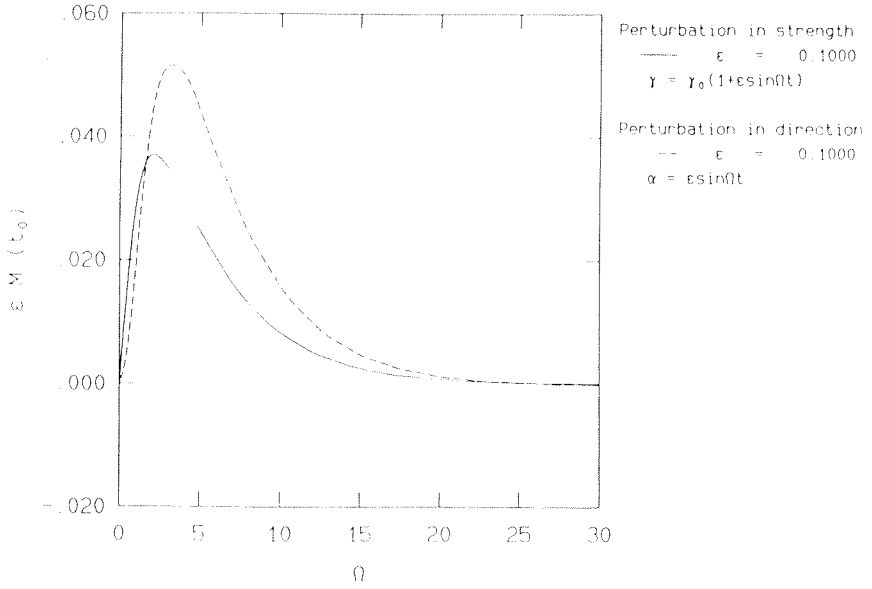


Figure 5.3 Graphs of F_γ, F_β with respect to Ω for unsteady PV systems

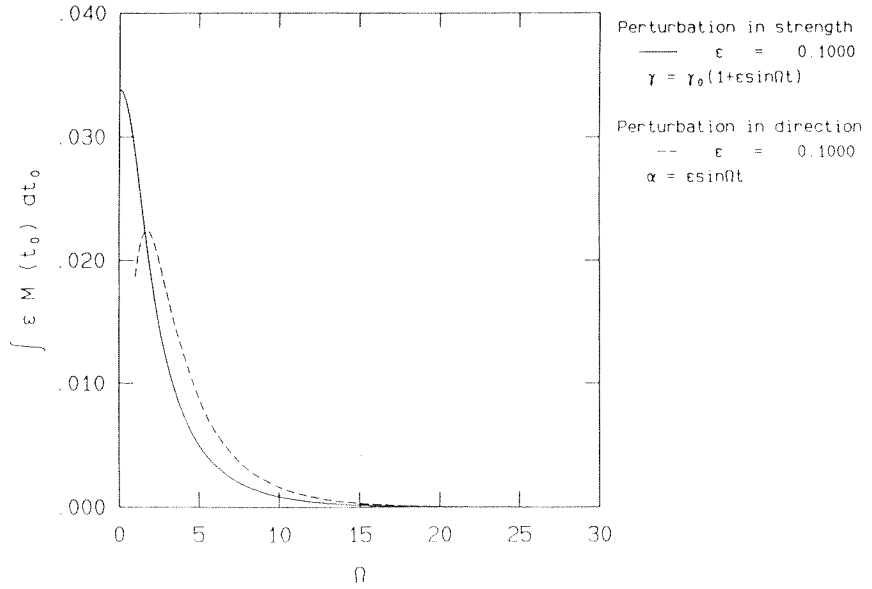


Figure 5.4 Graphs of area of a lobe corresponding to Fig. 5.3

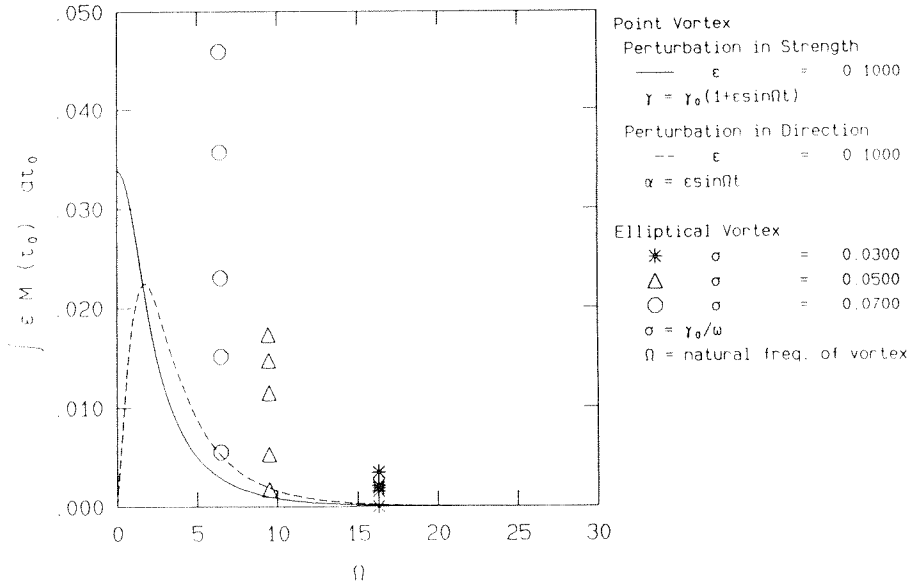


Figure 5.5 Graphs of area of a lobe for unsteady UEV systems in comparison to unsteady PV systems

Appendix 1

THE INDUCED VELOCITY FIELD BY A ELLIPTICAL VORTEX

We consider an elliptical vortex (EV) of arbitrary vorticity distribution and compute the velocity field around its centroid and the local straining effects in the induced flow field. By presenting these results, we not only give the exact solutions of the Euler equations corresponding to EV's but also hope to give some assistance to improve the computational elements of the vortex methods which may be used to simulate two-dimensional incompressible flows. For this purpose, we take the following steps; 1) define an EV, compute the induced velocity field around its centroid, 2) compute a local straining effect around a point in a general irrotational flow, and 3) apply the formulae to compute the induced velocity fields and the local straining effects in flow fields for a UEV and a gaussian elliptical vortex (GEV).

A1.1 Definition of a EV and induced velocity field around its centroid

We mean by an EV a region of vorticity in which each vorticity contour has an elliptical shape. The semi-major axis, a , and the semi-minor axis, b , of each ellipse has the same aspect ratio $\eta = \frac{a}{b}$. Those axes are properly aligned as shown in Fig. A1.1 and define an EV fixed coordinate system (X, Y) with $Z = X + iY$. The angle θ in Fig. A1.2 is called the inclination angle of the EV and measures the tilting of the vortex from the standard coordinate system (x, y) with $z = x + iy$. In a EV fixed coordinate system, it is convenient to use the elliptic coordinates (R, φ) which are defined as follows.

$$(X, Y) = (\sqrt{R\eta} \cos \varphi, \sqrt{R/\eta} \sin \varphi)$$

i.e.,

$$R = \sqrt{\left(\frac{X}{\sqrt{\eta}}\right)^2 + (Y\sqrt{\eta})^2} \quad (A1.1)$$

$$\varphi = \tan^{-1}\left(\frac{\eta Y}{X}\right)$$

By definition of the EV, the vorticity distribution in (X, Y) coordinate system is written using the elliptic coordinate variables.

$$\omega_E(X, Y) = \frac{\Gamma}{\pi} f\left(\frac{R}{\Lambda}\right) \quad (A1.2)$$

where

$$\int_0^{2\pi} \int_0^\infty \left\{f\left(\frac{R}{\Lambda}\right)\right\} \left\{\frac{R}{\Lambda}\right\} d\left(\frac{R}{\Lambda}\right) d\varphi = \pi$$

Λ is a mean core radius of the EV and $f\left(\frac{R}{\Lambda}\right)$ is a normalized vorticity distribution.

The two-dimensional Biot-Savart law for an arbitrary vorticity distribution $\omega(X, Y)$ may be written in a complex form

$$\dot{Z}^* = \frac{1}{i2\pi} \int \int \frac{\omega(\hat{X}, \hat{Y})}{Z - (\hat{X} + i\hat{Y})} d\hat{X} d\hat{Y} \quad (A1.3)$$

where \dot{Z}^* is the velocity conjugate at $Z = X + iY$. We now evaluate this integral in the elliptic coordinates. Substituting Eqn. (A1.2) into Eqn. (A1.3) yields

$$\dot{Z}^* = \frac{\Gamma}{i2\pi} \int_0^\infty \left\{f\left(\frac{\hat{R}}{\Lambda}\right)\right\} \left\{\frac{\hat{R}}{\Lambda}\right\} \left\{H\left(\frac{Z}{\Lambda}, \frac{\hat{R}}{\Lambda}; \eta\right)\right\} d\left(\frac{\hat{R}}{\Lambda}\right)$$

where

$$H\left(\frac{Z}{\Lambda}, \frac{\hat{R}}{\Lambda}, \eta\right) = \int_0^{2\pi} \frac{d\hat{\varphi}}{\left(\frac{Z}{\Lambda}\right) - \left(\frac{\hat{R}}{\Lambda}\right) \frac{1}{\sqrt{\eta}} (\cos \hat{\varphi} + i \sin \hat{\varphi})}$$

$H\left(\frac{Z}{\Lambda}, \frac{\hat{R}}{\Lambda}, \eta\right)$ can be computed by the residue theorem

$$H\left(\frac{Z}{\Lambda}, \frac{\hat{R}}{\Lambda}, \eta\right) = \begin{cases} \frac{1}{\pi} \frac{1}{\sqrt{\left(\frac{Z}{\Lambda}\right)^2 - \left(\frac{\eta^2 - 1}{\eta}\right) \left(\frac{\hat{R}}{\Lambda}\right)^2}} & \text{for } 0 \leq \hat{R} \leq R \\ 0 & \text{for } \hat{R} \geq R \end{cases}$$

Consequently, the velocity conjugate \dot{Z}^* at Z is written

$$\begin{aligned}\dot{Z}^* &= \dot{Z}^*(Z; \Gamma, \Lambda; \eta) \\ &= \frac{\Gamma}{i2\pi} \int_0^{(\frac{R}{\Lambda})} \left\{ f \left(\frac{\hat{R}}{\Lambda} \right) \right\} \left\{ \frac{\hat{R}}{\Lambda} \right\} \left\{ H \left(\frac{Z}{\Lambda}, \frac{\hat{R}}{\Lambda}, \eta \right) \right\} d \left(\frac{\hat{R}}{\Lambda} \right)\end{aligned}\quad (A1.4)$$

In a standard coordinate system (x, y) , the velocity conjugate z^* at $z = x + iy$ is

$$z^* = e^{-i\theta} \dot{Z}^*(ze^{-i\theta}; \Gamma, \Lambda; \eta) \quad (A1.5)$$

From Eqns. (A1.4) and (A1.5), it is clear that the contribution to the self-induced velocity at z comes only from the vortices interior to the ellipse of (η, θ) which goes through z .

A1.2 Local straining effect in an irrotational flow

In general, the irrotational velocity field at z is written using the complex potential function $F(z) = \phi(z) + i\psi(z)$ where $\phi(z) = \text{Real } F(z)$ is a potential function and $\psi(z) = \text{Im } F(z)$ is a stream function.

$$\begin{aligned}\dot{z}^* &= \frac{\partial}{\partial z} F(z) \\ &= \frac{\partial}{\partial z} (\phi(z) + i\psi(z))\end{aligned}$$

If the flow field is induced by some vorticity distribution ω , then $F(z)$ is given as follows.

$$F(z) = \frac{\Gamma}{i2\pi} \int \int \omega(\hat{x}, \hat{y}) \log\{z - (\hat{x} + i\hat{y})\} d\hat{x}d\hat{y}$$

Note that $F(z)$ is analytic in z because the flow is irrotational.

The local straining effects at $z_0 = x_0 + iy_0$ is computed as follows. The local velocity field around $z_0 = x_0 + iy_0$ can be expressed as a Taylor series in $(z - z_0)$ because the flow is irrotational.

$$\dot{z}^* = \dot{z}^*(z_0) + \gamma e^{-2\alpha i} (z - z_0) + O((z - z_0)^2)$$

The first order term in $z - z_0$ represent the local straining effect at $z = z_0$, i.e.,

$$\begin{aligned}\gamma e^{-2\alpha i} &= \frac{\partial}{\partial z} \dot{z}^* \Big|_{z=z_0} \\ &= \frac{\partial^2}{\partial z^2} F(z) \Big|_{z=z_0}\end{aligned}\tag{A1.6}$$

γ is the strength of the local straining effect and α is the inclination angle of the local straining axis form the standard coordinate system. Using Eqn. (A1.6), we obtain the straining effect at $z_0 = x_0 + iy_0$ for a known vorticity distribution $\omega(\hat{x}, \hat{y})$,

$$\gamma e^{-2\alpha i} = \frac{-1}{i2\pi} \int \int \frac{\omega(\hat{x}, \hat{y})}{\{z - (\hat{x} + i\hat{y})\}^2} d\hat{x} d\hat{y} \Big|_{z=z_0}\tag{A1.7}$$

Applying Eqn. (A1.7) for an EV, we obtain the local straining effect at $z = z_0$ induced by an EV.

$$\gamma e^{-2\alpha i} = \frac{\Gamma e^{-\theta i}}{i2\pi} \int^{(\frac{\hat{R}}{\Lambda})} \left\{ f\left(\frac{\hat{R}}{\Lambda}\right) \right\} \left\{ \frac{\hat{R}}{\Lambda} \right\} \left\{ H\left(\frac{Z}{\Lambda}, \frac{\hat{R}}{\Lambda}, \eta\right) \right\} d\left(\frac{\hat{R}}{\Lambda}\right) \Big|_{Z=z_0 e^{-\theta i}}\tag{A1.8}$$

where

$$\bar{H}\left(\frac{Z}{\Lambda}, \frac{\hat{R}}{\Lambda}, \eta\right) = \frac{-\frac{Z}{\Lambda}}{\pi \sqrt{\left(\frac{Z}{\Lambda}\right)^2 - \left(\frac{\eta^2 - 1}{\eta}\right)\left(\frac{\hat{R}}{\Lambda}\right)^2}}$$

A1.3 Applications to a UEV and GEV

We now apply Eqns. (A1.5) and (A1.8) for a UEV and a GEV (gaussian elliptical vortex).

A UEV

The vorticity distribution function for a UEV is as follows.

$$f\left(\frac{R}{\Lambda}\right) = \begin{cases} 1 & \text{for } R < \Lambda \\ 0 & \text{for } R > \Lambda \end{cases}$$

Hence the induced velocity field and the local straining effect at $z = z_0$ are

$$\begin{aligned}\dot{z}^* &= \frac{\Gamma}{i\pi D e^{2\theta i}} (z - \sqrt{z^2 - D e^{2\theta i}}) \\ \gamma e^{-2\alpha i} &= \frac{\Gamma}{i\pi D e^{2\theta i}} \left\{ 1 - \frac{1}{\sqrt{z^2 - D e^{-2\theta i}}} \right\} \Big|_{z=z_0}\end{aligned}$$

A GEV

We show another application using a Gaussian elliptical vortex (GEV). For a GEV, the normalized vorticity distribution function is

$$f\left(\frac{R}{\Lambda}\right) = \exp\left\{-\left(\frac{R}{\Lambda}\right)^2\right\} \quad (A1.11)$$

Substituting Eqn. (A1.11) into Eqns. (A1.5) and (A1.8), we obtain the induced velocity field for a GEV

$$\dot{z}^* = \frac{\Gamma}{2\Lambda e^{\theta i}} \sqrt{\frac{\eta}{\eta^2 - 1}} \left\{ e^{-\left(\frac{R}{\Lambda}\right)^2} \operatorname{cerf}\left(\frac{1}{\sqrt{\eta^2 - 1}} \frac{\zeta}{\Lambda}\right) - \operatorname{cerf}\left(\sqrt{\frac{\eta}{\eta^2 - 1}} \frac{Z}{\Lambda}\right) \right\} \Big|_{Z=ze^{-\theta i}}$$

where

$$\begin{aligned} \operatorname{cerf}(z) &= \text{complex error function} \\ &= e^{-z^2} \left\{ 1 + \frac{2i}{\sqrt{\pi}} \int_0^z e^{t^2} dt \right\} \\ \zeta &= \frac{1}{\sqrt{\eta}}(X + i\eta Y) \end{aligned}$$

and the local straining effect at z

$$\gamma e^{-2\alpha i} = e^{-2\theta i} \frac{\Gamma}{2\Lambda^2} \frac{\eta}{\eta^2 - 1} \left\{ e^{-\left(\frac{R}{\Lambda}\right)^2} \frac{1}{2\eta} \overline{\operatorname{cerf}}\left(\frac{1}{\sqrt{\eta^2 - 1}} \frac{\zeta}{\Lambda}\right) - \overline{\operatorname{cerf}}\left(\sqrt{\frac{\eta}{\eta^2 - 1}} \frac{Z}{\Lambda}\right) \right\} \Big|_{Z=ze^{-\theta i}}$$

where

$$\overline{\operatorname{cerf}}(z) = \frac{d}{dz} \{\operatorname{cerf}(z)\}$$

A1.4 Figures for Appendix 1

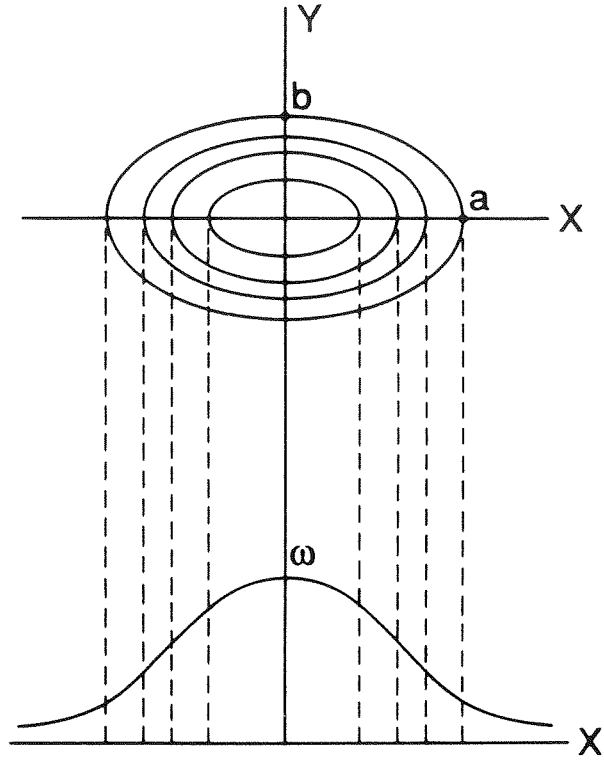


Figure A1.1 Vorticity distribution of a EV

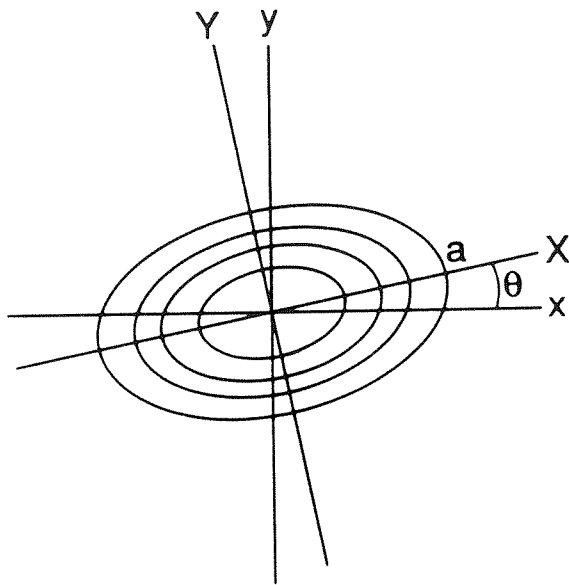


Figure A1.2 Coordinate system for a EV

Appendix 2

BIFURCATIONS

A2.1 Bifurcations on $\varphi = \frac{\pi}{2}$ (or positive ζ axis)

On $\varphi = \frac{\pi}{2}$, from Eqn. (2.9),

$$\begin{pmatrix} \frac{dI}{d\tau} \\ \frac{d\varphi}{d\tau} \end{pmatrix} = \begin{pmatrix} 1 \\ \frac{I+2}{\sqrt{I^2+4I}} - \frac{\kappa_0}{2} \end{pmatrix} - \sigma_0 \begin{pmatrix} 0 \\ \frac{I+2}{\sqrt{I^2+4I}} \end{pmatrix}$$

Hence, fixed points exist when $\frac{d\varphi}{d\tau} = 0$, i.e.,

$$\kappa_0 = 2\left(\sigma_0 \frac{I+2}{\sqrt{I^2+4I}} - \frac{1}{I+4}\right) \equiv K_+(I; \sigma_0)$$

Fig. A2.1 shows the graph of $I = K_+^{-1}(I; \sigma_0)$ with respect to K_+ for any $\sigma_0 > 0$. Recall that $(\sqrt{2I}, \varphi)$ are the polar coordinates for $\delta - \zeta$ phase space, hence the vertical axis of Fig. A2.1 is related to the positive ζ axis. The intersections of $I = K_+^{-1}(I; \sigma_0)$ and a vertical line $K_+ = \kappa_0$ in Fig. A2.1 correspond to the fixed points. Clearly, there exist 0 fixed point for $\kappa_0 < K_1(\sigma_0)$, 1 fixed point for $\kappa_0 = K_1(\sigma_0)$, 2 fixed points for $K_1(\sigma_0) < \kappa_0 < K_2(\sigma_0)$, and 1 fixed point for $\kappa_0 > K_2(\sigma_0)$ where

$$\begin{aligned} K_1(\sigma_0) &= \{K_+(I; \sigma_0) \mid \frac{\partial}{\partial I} K_+(I; \sigma_0) = 0\} \\ &= \{K_+(I; \sigma_0) \mid I^3 = (4\sigma_0)^2(I+4)\} \\ K_2(\sigma_0) &= \{K_+(I; \sigma_0) \mid \lim_{I \rightarrow \infty} K_+(I; \sigma_0)\} \\ &= \{K_+(I; \sigma_0) \mid K_+(I; \sigma_0) = 2\sigma_0\} \end{aligned}$$

The Jacobian of Eqn. (2.9) shows that for $K_1(\sigma_0) < \kappa_0 < K_2(\sigma_0)$, a fixed point with the larger I is of hyperbolic type and a fixed point with the smaller I is of elliptic type. The followings are two bifurcations regarding the $\varphi = \frac{\pi}{2}$ axis.

S^+ : saddle-node bifurcation

A pair of hyperbolic and elliptic fixed points are born on S^+ .

$$S^+ = \{(\kappa_0, \sigma_0) \mid \kappa_0 = 2(\sigma_0 \frac{I+2}{\sqrt{I^2+4I}} - \frac{1}{I+4}), I^3 = (4\sigma_0)^2(I+4)\}$$

I_1^+ : bifurcation at $I = \infty$ on $\varphi = \frac{\pi}{2}$

A hyperbolic fixed point disappears to infinity.

$$I_1^+ = \{(\kappa_0, \sigma_0) \mid \kappa_0 = 2\sigma_0\}$$

A2.2 Bifurcations on $\varphi = \frac{3\pi}{2}$ (or negative ζ axis)

On $\varphi = \frac{3\pi}{2}$, from Eqn. (2.9),

$$\begin{pmatrix} \frac{dI}{d\tau} \\ \frac{d\varphi}{d\tau} \end{pmatrix} = \begin{pmatrix} 0 \\ \frac{1}{I+4} + \sigma_0 \frac{I+2}{\sqrt{I^2+4I}} - \frac{\kappa_0}{2} \end{pmatrix}$$

A fixed point exists when $\frac{d\varphi}{d\tau} = 0$, i.e.,

$$\kappa_0 = -2(\sigma_0 \frac{I+2}{\sqrt{I^2+4I}} + \frac{1}{I+4}) \equiv K_-(I; \sigma_0)$$

Fig. A2.2 shows that the graph of $I = K_-^{-1}(I; \sigma_0)$ with respect to K_- for any $\sigma_0 > 0$. The vertical axis of Fig. A2.2 is related to the negative ζ axis. The intersections of $I = K_-^{-1}(I; \sigma_0)$ and a vertical line $K_- = \kappa_0$ in Fig. A2.2 correspond to the fixed point on $\varphi = \frac{3\pi}{2}$. There exist, 1 fixed point for $\kappa_0 < K_3(\sigma_0)$, and 0 fixed point for $\kappa_0 \geq K_3(\sigma_0)$, where

$$\begin{aligned} K_3(\sigma_0) &= \{K_-(I; \sigma_0) \mid \lim_{I \rightarrow \infty} K_-(I; \sigma_0)\} \\ &= \{K_-(I; \sigma_0) \mid K_-(I; \sigma_0) = -2\sigma_0\} \end{aligned}$$

The Jacobian of Eqn. (2.9) shows that the fixed point is of elliptic type. The corresponding bifurcation on $\varphi = \frac{3\pi}{2}$ is as follows.

I_2^+ : bifurcation at $I = \infty$ on $\varphi = \frac{3\pi}{2}$

A elliptic fixed point disappears to infinity.

$$I_2^+ = \{(\kappa_0, \sigma_0) \mid \kappa_0 = -2\sigma_0\}$$

A2.3 Bifurcations to periodic motion as $I \rightarrow \infty$

As $I \rightarrow \infty$, Eqn. (2.9) becomes,

$$\begin{pmatrix} \frac{dI}{d\tau} \\ \frac{d\varphi}{d\tau} \end{pmatrix} \simeq \begin{pmatrix} \sigma_0 \cos \varphi \\ -\sigma_0 \sin \varphi + \frac{\kappa_0}{2} \end{pmatrix}$$

From $\frac{d\varphi}{d\tau}$ equation, $\frac{d\varphi}{d\tau} > 0$ if $\sigma_0 < \frac{\kappa_0}{2}$ for any φ , which corresponds to counterclockwise periodic motion. Similarly, $\frac{d\varphi}{d\tau} < 0$ if $\sigma_0 < -\frac{\kappa_0}{2}$ for any φ , which correspond to and clockwise periodic motion. For $-\frac{\kappa_0}{2} < \sigma_0 < \frac{\kappa_0}{2}$, the motion for $I \gg 1$ is not periodic. The corresponding bifurcations are as follows.

I_1^+ : bifurcation to counterclockwise periodic motion for $I \gg 1$

$$I_1^+ = \{(\kappa_0, \sigma_0) \mid \kappa_0 = 2\sigma_0\}$$

I_2^+ : bifurcation to clockwise periodic motion for $I \gg 1$

$$I_2^+ = \{(\kappa_0, \sigma_0) \mid \kappa_0 = -2\sigma_0\}$$

Notice that these two bifurcations are associated with the bifurcations of the fixed points which we described in A2.1 and A2.2.

A2.4 Global bifurcation

The global bifurcation occurs when the origin of $\delta - \zeta$ phase space (i.e., a point at $I = 0$) lies in the homoclinic orbit. The condition for the global bifurcation is that two Hamiltonians evaluated at the hyperbolic fixed point (H_h) and at the origin (H_0) are the same.

$$H_h = H_0$$

where

$$H_h = \log(I + 4) - \sigma_0 \sqrt{I^2 + 4I} + \frac{\kappa_0}{2} I$$

$$H_0 = \log 4$$

$$\begin{aligned} I &= \{I(\kappa_0, \sigma_0) \mid \frac{d\varphi}{d\tau}|_{\varphi=\frac{\pi}{2}} = 0\} \\ &= \{I(\kappa_0, \sigma_0) \mid \frac{1}{I+4} - \sigma_0 \frac{I+2}{\sqrt{I^2+4I}} - \frac{\kappa_0}{2}\} \end{aligned}$$

The corresponding bifurcation curve G^+ is.

G^+ : global bifurcation

$$\begin{aligned} G^+ &= \{(\kappa_0, \sigma_0) \mid \frac{1}{I+4} - \sigma_0 \frac{I+2}{\sqrt{I^2+4I}} - \frac{\kappa_0}{2} = 0, \\ &\quad \log \frac{I+4}{4} - \sigma_0 \sqrt{I^2+4I} - \frac{\kappa_0}{2} I = 0\} \end{aligned}$$

A2.5 Bifurcations on $\sigma_0 = 0$

For $\sigma_0 = 0$, Eqn. (2.9) becomes

$$\begin{pmatrix} \frac{dI}{d\tau} \\ \frac{d\varphi}{d\tau} \end{pmatrix} = \begin{pmatrix} 0 \\ \frac{1}{I+4} - \frac{\kappa_0}{2} \end{pmatrix}$$

First let us consider $-\frac{1}{2} < \kappa_0 < 0$ with $\sigma_0 = 0$. There exist I_0 such that $\frac{d\varphi}{d\tau} = 0$ where $I_0 = -(\frac{2}{\kappa_0} + 4)$. This corresponds to a ring of fixed points at $I_0 = -(\frac{2}{\kappa_0} + 4)$. If we move from $\sigma_0 = 0$ to $\sigma_0 > 0$, then the ring of fixed points breaks up and leave a hyperbolic fixed point on $\varphi = \frac{\pi}{2}$. This generically results in the birth of two homoclinic orbits with one encircling the other interior to itself. Similarly, if we move from $\sigma_0 = 0$ to $\sigma_0 < 0$, then the ring of fixed points breaks up and leave a hyperbolic fixed point on $\varphi = \frac{3\pi}{2}$. Again, this generically results in the birth of two homoclinic orbits with one encircling the other interior to itself. We call this bifurcation the ring bifurcation and denote the corresponding bifurcation curve as R .

R : ring bifurcation

$$R = \{(\kappa_0, \sigma_0) \mid -\frac{1}{2} < \kappa_0 < 0, \sigma_0 = 0\}$$

For $\kappa_0 > 0$, the bifurcation regarding to the UEV motion (not a bifurcation in a strict sense) on $\sigma_0 = 0$ is as follows. The elliptic fixed point on the positive ζ axis for $\sigma_0 < 0$ moves to the negative ζ axis as we cross $\sigma_0 = 0$. Similarly for $\kappa_0 < 0$, the elliptic fixed point on the negative ζ axis for $\sigma_0 < 0$ moves to positive ζ axis as we cross $\sigma_0 = 0$. We define bifurcation curves U_1 and U_2 regarding these bifurcations.

U_1 : bifurcation at the origin

$$U_1 = \{(\kappa_0, \sigma_0) \mid \kappa_0 < 0, \sigma_0 = 0\}$$

U_2 : bifurcation at the origin

$$U_2 = \{(\kappa_0, \sigma_0) \mid \kappa_0 < -\frac{1}{2}, \sigma_0 = 0\}$$

A2.6 Bifurcation curves

We give a list of the bifurcation curves.

$$S^+ = \{(\kappa_0, \sigma_0) \mid \kappa_0 = 2(\sigma_0 \frac{I+2}{\sqrt{I^2+4I}} - \frac{1}{I+4}), I^3 = (4\sigma_0)^2(I+4)\}$$

$$G^+ = \{(\kappa_0, \sigma_0) \mid \frac{1}{I+4} - \sigma_0 \frac{I+2}{\sqrt{I^2+4I}} - \frac{\kappa_0}{2} = 0, \\ \log \frac{I+4}{4} - \sigma_0 \sqrt{I^2+4I} - \frac{\kappa_0}{2} I = 0\}$$

$$I_1^+ = \{(\kappa_0, \sigma_0) \mid \sigma_0 = \frac{\kappa_0}{2}\}$$

$$I_2^+ = \{(\kappa_0, \sigma_0) \mid \sigma_0 = -\frac{\kappa_0}{2}\}$$

$$U_1 = \{(\kappa_0, \sigma_0) \mid \kappa_0 > 0, \sigma_0 = 0\}$$

$$R = \{(\kappa_0, \sigma_0) \mid -\frac{1}{2} < \kappa_0 < 0, \sigma_0 = 0\}$$

$$U_2 = \{(\kappa_0, \sigma_0) \mid \kappa_0 < -\frac{1}{2}, \sigma_0 = 0\}$$

A2.7 Figures for Appendix 2

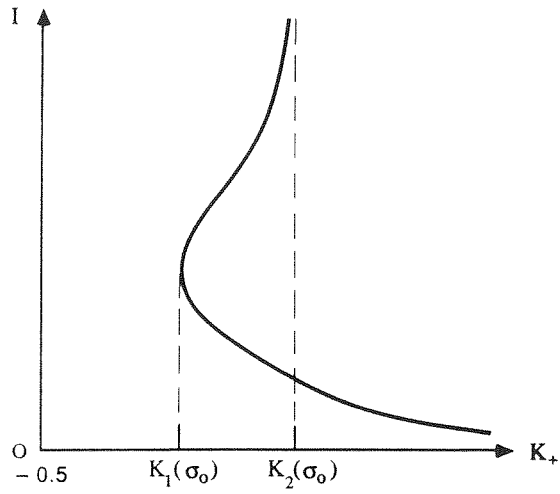


Figure A2.1 Graph of $I = K_+^{-1}(I; \sigma_0)$

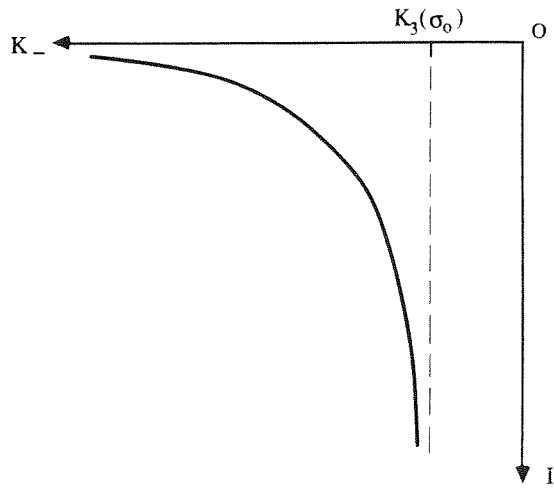


Figure A2.2 Graph of $I = K_-^{-1}(I; \sigma_0)$

Appendix 3

THE MELNIKOV FUNCTION $M^{\frac{m}{n}}(\tau_0)$ ON THE RESONANCE BAND OF ORDER $\frac{m}{n}$ WITH GEOMETRICAL SYMMETRY

Let us consider the following system.

$$\begin{pmatrix} \frac{d\delta}{d\tau} \\ \frac{d\zeta}{d\tau} \end{pmatrix} = \begin{pmatrix} f_1(q) + \epsilon g_1(q, \tau) + O(\epsilon^2) \\ f_2(q) + \epsilon g_2(q, \tau) + O(\epsilon^2) \end{pmatrix}$$

where

$$\begin{aligned} q(\tau) &= (\delta(\tau), \zeta(\tau)) \\ \begin{pmatrix} f_1(q) \\ f_2(q) \end{pmatrix} &= \begin{pmatrix} \frac{\partial}{\partial \zeta} H(q) \\ -\frac{\partial}{\partial \delta} H(q) \end{pmatrix} \\ \begin{pmatrix} g_1(q, \tau) \\ g_2(q, \tau) \end{pmatrix} &= \begin{pmatrix} \bar{g}_1(q) \sin \Omega \tau \\ \bar{g}_2(q) \sin \Omega \tau \end{pmatrix} \\ &O(\epsilon^2); \text{ time periodic with period } T = \frac{2\pi}{\Omega} \end{aligned}$$

The purpose of this appendix is to show the properties of the Melnikov function on resonance band of order $\frac{m}{n}$ for this system when the unperturbed phase space has some geometrical symmetry as shown in Figs. 4.13a and 4.13b.

Case 1

Let us consider a system whose unperturbed phase space has a geometrical symmetry as shown in Fig. 4.13a. If we choose $\tau = 0$ on the ζ -axis, then the unperturbed periodic orbit $q^H(\tau) = (\delta^H(\tau), \zeta^H(\tau))$ satisfies the following condition due to the symmetry, where a superscript ' H ' denotes the level of the Hamiltonian function.

$$(\delta^H(\tau), \zeta^H(\tau)) = (-\delta^H(-\tau), \zeta^H(-\tau))$$

The orbit $q^H(\tau)$ can be written as a Fourier series as follows.

$$(\delta^H(\tau), \zeta^H(\tau)) = \left(\sum_{\ell=0}^{\infty} D_{\ell}^H \sin \Omega^H \ell \tau, \sum_{\ell=0}^{\infty} Z_{\ell}^H \cos \Omega^H \ell \tau \right) \quad (\text{A3.1})$$

where Ω^H is the natural frequency of the orbit, and D_ℓ^H and Z_ℓ^H are Fourier coefficients.

Now we want to compute the Melnikov function on RB $\frac{m}{n}$.

$$\begin{aligned} M^{\frac{m}{n}}(\tau_0) &= \int_{-\frac{mT}{2}}^{\frac{mT}{2}} \{f \wedge g\}(q^H(\tau), \tau + \tau_0) d\tau \\ &= \int_{-\frac{mT}{2}}^{\frac{mT}{2}} \{f \wedge \bar{g}\} \sin \Omega \tau (q^H(\tau), \tau + \tau_0) d\tau \end{aligned} \quad (\text{A3.2})$$

We define $h(q^H(\tau))$ as follows.

$$h(q^H(\tau)) = \{f \wedge \bar{g}\}(q^H(\tau)) \quad (\text{A3.3})$$

To compute $M^{\frac{m}{n}}(\tau)$, we examine the form of $h(q^H(\tau))$ using Eqn. (A3.1). Since f and \bar{g} are both functions of $q^H(\tau) = (\delta(\tau), \zeta(\tau))$ and $\delta(\tau)$ is odd and ζ is even in time by definition, each term in $h(q^H(\tau))$ is either odd or even in time. In other words, each term in $h(q^H(\tau))$ can be written as either a sine Fourier series or a cosine Fourier series.

$$h(q^H(\tau)) = h_O(q^H(\tau)) + h_E(q^H(\tau)) \quad (\text{A3.4})$$

$$\begin{aligned} h_O(q^H(\tau)) &= \sum_{\ell=1}^{\infty} O_\ell^H \sin \Omega^H \ell \tau \\ h_E(q^H(\tau)) &= \sum_{\ell=1}^{\infty} E_\ell^H \cos \Omega^H \ell \tau \end{aligned} \quad (\text{A3.5})$$

$h_O(q^H(\tau))$ and $h_E(q^H(\tau))$ describe odd and even terms respectively. By substituting Eqn. (A3.4) into Eqn. (A3.2),

$$M^{\frac{m}{n}}(\tau_0) = M_O^{\frac{m}{n}}(\tau_0) + M_E^{\frac{m}{n}}(\tau_0)$$

Further substitution of Eqn. (A3.5) gives

$$\begin{aligned} M_O^{\frac{m}{n}}(\tau_0) &= \int_{-\frac{mT}{2}}^{\frac{mT}{2}} h_O(q^H(\tau)) \sin \Omega(\tau + \tau_0) d\tau \\ M_E^{\frac{m}{n}}(\tau_0) &= \int_{-\frac{mT}{2}}^{\frac{mT}{2}} h_E(q^H(\tau)) \sin \Omega(\tau + \tau_0) d\tau \end{aligned}$$

where

$$M_O^{\frac{m}{n}}(\tau_0) = \begin{cases} \frac{m\pi O_m}{\Omega} \cos \Omega \tau_0 & \text{for } n = 1 \\ 0 & \text{for } n \neq 1 \end{cases}$$

$$M_E^{\frac{m}{n}}(\tau_0) = \begin{cases} \frac{m\pi E_m}{\Omega} \sin \Omega \tau_0 & \text{for } n = 1 \\ 0 & \text{for } n \neq 1 \end{cases}$$

It follows that $M^{\frac{m}{n}}(\tau_0)$ for the ultraharmonic resonance band (i.e. $n \neq 1$) is identically zero if the symmetry shown in Fig. (4.13(a)) exists. In other words, ultraharmonics are at least $O(\epsilon^2)$.

Case2

Now we consider the system with symmetry show in Fig. 4.13b. We follow the same procedure as in Case 1 to compute $M^{\frac{m}{n}}(\tau_0)$. If we choose $\tau = 0$ on the ζ - axis, then the unperturbed periodic orbit $q^H(\tau) = (\delta^H(\tau), \zeta^H(\tau))$ satisfies the following condition due to the symmetry.

$$(\delta^H(\tau), \zeta^H(\tau)) = (-\delta^H(-\tau), \zeta^H(-\tau))$$

$$(\delta^H(\frac{T^H}{2} - \tau), -\zeta^H(\frac{T^H}{2} - \tau)) = (-\delta^H(\frac{T^H}{2} + \tau), -\zeta^H(\frac{T^H}{2} + \tau)) \quad (\text{A3.6})$$

where T^H denotes the period of the orbit. The orbit $q^H(\tau)$ is then written in a Fourier series to satisfy Eqn.(A3.6).

$$(\delta^H(\tau), \zeta^H(\tau)) = \left(\sum_{\ell=0}^{\infty} D_{2\ell+1}^H \sin \Omega^H(2\ell+1)\tau, \sum_{\ell=0}^{\infty} Z_{2\ell+1}^H \cos \Omega^H(2\ell+1)\tau \right) \quad (\text{A3.7})$$

Note that the even order Fourier coefficients of both $\delta(\tau)$ and $\zeta(\tau)$ are identically zero. Again, the Melnikov function has the following form.

$$M^{\frac{m}{n}}(\tau_0) = \int_{-\frac{mT}{2}}^{\frac{mT}{2}} \{h(q^H(\tau))\} \sin \Omega \tau (q^H(\tau), \tau + \tau_0) d\tau \quad (\text{A3.8})$$

where $h(q^H(\tau))$ is defined in Eqn. (A3.3). To compute $M^{\frac{m}{n}}(\tau)$, we examine the form of $h(q^H(\tau))$ in Eqn. (A3.3) using Eqn. (A3.7). Notice that f and \bar{g} are both functions of $q^H(\tau) = (\delta(\tau), \zeta(\tau))$, and $\delta(\tau)$ is odd and ζ is even in time with all even order Fourier coefficients identically zero as shown in Eqn. (3.7). It can be

shown that each term in $h(q^H(\tau))$ has either one of following four forms, $h_{OO}(q^H(\tau))$, $h_{OE}(q^H(\tau))$, $h_{EO}(q^H(\tau))$ or $h_{EE}(q^H(\tau))$.

$$h(q^H(\tau)) = h_{OO}(q^H(\tau)) + h_{OE}(q^H(\tau)) + h_{EO}(q^H(\tau)) + h_{EE}(q^H(\tau)) \quad (\text{A3.9})$$

$$\begin{aligned} h_{OO}(q^H(\tau)) &= \sum_{\ell=1}^{\infty} O_{\ell}^O \sin \Omega^H(2\ell + 1)\tau \\ h_{OE}(q^H(\tau)) &= \sum_{\ell=1}^{\infty} O_{\ell}^E \sin \Omega^H 2\ell\tau \\ h_{EO}(q^H(\tau)) &= \sum_{\ell=1}^{\infty} E_{\ell}^O \cos \Omega^H(2\ell + 1)\tau \\ h_{EE}(q^H(\tau)) &= \sum_{\ell=1}^{\infty} E_{\ell}^E \cos \Omega^H 2\ell\tau \end{aligned} \quad (\text{A3.10})$$

where the coefficients, O_{ℓ}^O , O_{ℓ}^E , E_{ℓ}^O , E_{ℓ}^E , are uniquely determined by the form of $h(q^H(\tau))$ and Eqn. (A3.7). By substituting Eqn. (A3.9) into Eqn. (A3.8), we obtain

$$M^{\frac{m}{n}}(\tau_0) = M_{OO}^{\frac{m}{n}}(\tau_0) + M_{OE}^{\frac{m}{n}}(\tau_0) + M_{EO}^{\frac{m}{n}}(\tau_0) + M_{EE}^{\frac{m}{n}}(\tau_0)$$

where

$$\begin{aligned} M_{OO}^{\frac{m}{n}}(\tau_0) &= \int_{-\frac{mT}{2}}^{\frac{mT}{2}} h_{OO}(q^H(\tau)) \sin \Omega(\tau + \tau_0) d\tau \\ M_{OE}^{\frac{m}{n}}(\tau_0) &= \int_{-\frac{mT}{2}}^{\frac{mT}{2}} h_{OE}(q^H(\tau)) \sin \Omega(\tau + \tau_0) d\tau \\ M_{EO}^{\frac{m}{n}}(\tau_0) &= \int_{-\frac{mT}{2}}^{\frac{mT}{2}} h_{EO}(q^H(\tau)) \sin \Omega(\tau + \tau_0) d\tau \\ M_{EE}^{\frac{m}{n}}(\tau_0) &= \int_{-\frac{mT}{2}}^{\frac{mT}{2}} h_{EE}(q^H(\tau)) \sin \Omega(\tau + \tau_0) d\tau \end{aligned}$$

Furthermore, substituting Eqn. (A3.9), we obtain

$$\begin{aligned} M_{OO}^{\frac{m}{n}}(\tau_0) &= \begin{cases} \frac{m\pi O_m^O}{\Omega} \cos \Omega\tau_0 & \text{for } n = 1 \text{ and } m = \text{ odd} \\ 0 & \text{otherwise} \end{cases} \\ M_{OE}^{\frac{m}{n}}(\tau_0) &= \begin{cases} \frac{m\pi O_m^E}{\Omega} \cos \Omega\tau_0 & \text{for } n = 1 \text{ and } m = \text{ even} \\ 0 & \text{otherwise} \end{cases} \\ M_{EO}^{\frac{m}{n}}(\tau_0) &= \begin{cases} \frac{m\pi E_m^O}{\Omega} \sin \Omega\tau_0 & \text{for } n = 1 \text{ and } m = \text{ odd} \\ 0 & \text{otherwise} \end{cases} \end{aligned}$$

$$M_{EE}^{\frac{m}{n}}(\tau_0) = \begin{cases} \frac{m\pi E^E}{\Omega^m} \sin \Omega\tau_0 & \text{for } n = 1 \text{ and } m = \text{even} \\ 0 & \text{otherwise} \end{cases}$$

It follows that $M_{EE}^{\frac{m}{n}}(\tau_0)$ for the ultraharmonic resonance band (i.e. $n \neq 1$) is identically zero if the symmetry shown in Fig. (4.13(a)) exists. In other words, ultraharmonics are at least $O(\epsilon^2)$. Moreover, there may exist only odd order subharmonics or even order subharmonics resonance band of order $\frac{m}{1}$ depending on how the perturbation is imposed (i.e., the form of $h(q^H(\tau))$).

Appendix 4

PERTURBATION FREQUENCY RANGE TRANSITION BETWEEN OSCILLATION AND ROTATION (Proof for Equation (4.3))

Proof

For the proof, we take the following steps;

- 1) compute the width of RB $\frac{m}{n}$ up to the first order in ϵ , denoted by $d_0^H(\tau_0)$, corresponding to the unperturbed orbit, denoted by $q_0^H(\tau)$, going through the origin of the coordinate system $(\delta, \zeta) = (0, 0)$ with natural frequency Ω_0^H . (i.e., resonance relation $m\Omega_0^H = n\Omega_0$ where Ω_0 is the corresponding perturbation frequency).
- 2) compute the point on the ζ -axis $(\delta, \zeta) = (0, \zeta_*)$ at which a stable invariant manifold of period m point of RB $\frac{m}{n}$ intersects the ζ -axis, up to the first order in ϵ , using $d_0^H(\tau_0)$.
- 3) compute the natural frequency, denoted by Ω_*^H , of the unperturbed periodic orbit going through $(\delta, \zeta) = (0, \zeta_*)$ up to the first order in ϵ from ζ_* .
- 4) compute the width of RB $\frac{m}{n}$ up to the first order in ϵ , denoted by $d_*^H(\tau_0)$, corresponding to the unperturbed periodic orbit going through $(\delta, \zeta) = (0, \zeta_*)$, denoted by $q_*^H(\tau)$, with natural frequency Ω_*^H (i.e., resonance relation $m\Omega_*^H = n\Omega_*$ where Ω_* is the corresponding perturbation frequency), and argue that $d_*^H(\tau_0) = d_0^H(\tau_0) + O(\epsilon^2)$.

5) obtain $\Delta\Omega^{\frac{m}{n}}$ from Ω_0 and Ω_* .

1) By definition, the width of the corresponding RB $\frac{m}{n}$, $d^{\frac{m}{n}}(\tau_0; \epsilon)$, and its first order term, $d_0^H(\tau_0)$, are as follows.

$$d^{\frac{m}{n}}(\tau_0; \epsilon) = d_0^H(\tau_0) + O(\epsilon^2)$$

where

$$d_0^H(\tau_0) = \epsilon \frac{M_0^{\frac{m}{n}}(\tau_0)}{\|f(q_0^H(-\tau_0))\|}$$

and

$$M_0^{\frac{m}{n}}(\tau_0) = M^{\frac{m}{n}}(\tau_0)|_{\Omega^H = \Omega_0^H}$$

Furthermore, from the resonance relation we obtain

$$\Omega_0 = \frac{m}{n} \Omega_0^H \tag{A4.1}$$

2) Since the width of RB $\frac{m}{n}$ describes the signed distance from the unstable invariant manifolds to stable invariant manifolds perpendicular to the corresponding unperturbed periodic orbit, ζ_* is given as follows.

$$\zeta_* = \frac{1}{2} d_*^H(\tau_0) |_{\tau_0 = \tau_0^*}$$

where τ_0^* is the value of the parametrization variable on the ζ -axis.

3) The natural frequency on the periodic orbit going through $(\delta, \zeta) = (0, \zeta_*)$ up to the first order in ϵ , denoted by Ω_*^H , is obtained by Taylor expansion of Ω^H around Ω_0^H .

$$\Omega_*^H = \Omega_0^H + \frac{\partial \Omega^H}{\partial \zeta} |_{(\delta, \zeta) = (0, 0)} \zeta_* + O(\epsilon^2) \tag{A4.2}$$

4) We first want to obtain $d_*^H(\tau_0)$ in relation to $d_0^H(\tau_0)$

$$d_*^H(\tau_0) = \epsilon \frac{M^{\frac{m}{n}}(\tau_0)|_{\Omega^H = \Omega_*^H}}{\|f(q_*^H(-\tau_0))\|}$$

In doing so, we take Taylor expansion in $M^{\frac{m}{n}}(\tau_0)$ around $\Omega^H = \Omega_0^H$.

$$M^{\frac{m}{n}}(\tau_0)|_{\Omega^H = \Omega_*^H} = M^{\frac{m}{n}}(\tau_0)|_{\Omega^H = \Omega_0^H} + O(\epsilon)$$

Furthermore, we take Taylor expansion in $\|f(q^H(-\tau_0))\|$ around $\Omega^H = \Omega_0^H$.

$$\|f(q_*^H(-\tau_0))\| = \|f(q_0^H(-\tau_0))\| + O(\epsilon)$$

Hence

$$\begin{aligned} d_*^H(\tau_0) &= \epsilon \frac{M_*^{\frac{m}{n}}(\tau_0)|_{\Omega^H=\Omega_*^H}}{\|f(q_*^H(-\tau_0))\|} \\ &= \epsilon \frac{M_0^{\frac{m}{n}}(\tau_0)|_{\Omega^H=\Omega_0^H} + O(\epsilon)}{\|f(q_0^H(-\tau_0))\| + O(\epsilon)} \\ &= d_0^H(\tau_0) + O(\epsilon^2) \end{aligned}$$

Moreover, from the resonance relation we obtain

$$\Omega_* = \frac{m}{n} \Omega_*^H \tag{A4.3}$$

5) It follows from 4) that, under the perturbation with perturbation frequency $\Omega_* = \frac{m}{n} \Omega_*^H$, the origin of the coordinate is contained in the RB $\frac{m}{n}$. Hence, we obtain from Eqns. (A4.1),(A4.2) and (A4.3)

$$\begin{aligned} \Delta \Omega^{\frac{m}{n}} &= |\Omega_0 - \Omega_*| \\ &= \left| \frac{m}{n} (\Omega_0^H - \Omega_*^H) \right| \\ &= \left| \frac{1}{2} \frac{m}{n} \frac{\partial \Omega^H}{\partial \zeta} \Big|_{(\delta, \zeta)=(0,0)} d_0^H(\tau_0) \Big|_{\tau_0=\bar{\tau}_0} \right| \end{aligned}$$

where

$$d_0^H(\tau_0) = \epsilon \frac{M_0^{\frac{m}{n}}(\tau_0)}{\|f(q_0^H(-\tau_0))\|}$$

Appendix 5

PROOF FOR REMARK 3,4 AND 5 FOR CASE 2

Proof for Remark 3

We want to show that for any m , the condition for RB $\frac{m}{1}$ given Eqn. (4.3) can not be satisfied, i.e.,

$$\Omega \notin (\Omega_1^m, \Omega_2^m)$$

For any $m \geq k + 1$,

$$\Omega < \Omega_1^{k+1} \leq \Omega_1^m < \Omega_2^m$$

From Remark 1, there exists no unperturbed periodic orbit which satisfies the resonance relation $m\Omega^H = \Omega$ for any $m \geq k + 1$.

For any $m \leq k$,

$$\Omega > \Omega_2^k \geq \Omega_2^m > \Omega_1^m$$

From Remark 1, there exists no unperturbed periodic orbit which satisfies the resonance relation $m\Omega^H = \Omega$ for any $m \leq k$. Consequently, there exists no unperturbed periodic orbit which satisfies the resonance relation $m\Omega^H = \Omega$ for any m .

Proof for Remark 4

If we show for any $k^* < k$

$$\Omega_2^{k^*} < \Omega_1^{k^*+1}$$

then it follows from Eqn. (4.3) that there exists frequency gap of order k^* . Using the definition of $\Omega_1^{k^*}$ and $\Omega_1^{k^*+1}$, and the condition for the frequency gap of order

k ,

$$\begin{aligned}
 \Omega_1^{k^*+1} - \Omega_2^{k^*} &= (k^* + 1)\Omega_{\min}^H - k^*\Omega_{\max}^H \\
 &= (k^* + 1)\Omega_{\min}^H - k^*\Omega_{\max}^H + (k - k^*)\Omega_{\min}^H - (k - k^*)\Omega_{\min}^H \\
 &> (k^* + 1)\Omega_{\min}^H - k^*\Omega_{\max}^H + (k - k^*)\Omega_{\min}^H - (k - k^*)\Omega_{\max}^H \\
 &= (k + 1)\Omega_{\min}^H - k\Omega_{\max}^H \\
 &> 0
 \end{aligned}$$

i.e.,

$$\Omega_2^{k^*} < \Omega_1^{k^*+1}$$

Proof for Remark 5

The conditions for N_g is are as follows.

$$\begin{aligned}
 \Omega_2^{N_g} &< \Omega_1^{N_g+1} \\
 \Omega_2^{N_g+1} &> \Omega_1^{N_g+2}
 \end{aligned}$$

From first inequality, we obtain using Eqn. (4.3)

$$N_g > \frac{\Omega_{\min}^H}{\Omega_{\max}^H - \Omega_{\min}^H}$$

From second inequality, we obtain using Eqn. (4.3)

$$N_g < \frac{\Omega_{\min}^H}{\Omega_{\max}^H - \Omega_{\min}^H}$$

As a result, we obtain

$$N_g = \left[\frac{\Omega_{\min}^H}{\Omega_{\max}^H - \Omega_{\min}^H} + 1 \right]$$

Appendix 6

THE MELNIKOV FUNCTIONS FOR THE HAMILTONIAN PERTURBATIONS

We consider the following two types of the Hamiltonian perturbation which are described in Chapter 4. First we consider the Melnikov function on the homoclinic orbit.

Type 1 : external excitation

Suppose that a part of the Hamiltonian is sinusoidally excited in time.

$$\begin{aligned} \begin{pmatrix} \frac{dI}{d\tau} \\ \frac{d\varphi}{d\tau} \end{pmatrix} &= \begin{pmatrix} -\frac{\partial}{\partial\varphi}\{H(I, \varphi; \tau)\} \\ \frac{\partial}{\partial I}\{H(I, \varphi; \tau)\} \end{pmatrix} \\ &= \begin{pmatrix} -\frac{\partial}{\partial\varphi}\{\bar{H}(I, \varphi) + (1 + \epsilon \sin \Omega\tau)\hat{H}(I, \varphi)\} \\ \frac{\partial}{\partial I}\{\bar{H}(I, \varphi) + (1 + \epsilon \sin \Omega\tau)\hat{H}(I, \varphi)\} \end{pmatrix} \end{aligned} \quad (A6.1)$$

where

$$H(I, \varphi; \tau) = \bar{H}(I, \varphi) + (1 + \epsilon \sin \Omega\tau)\hat{H}(I, \varphi)$$

where $\hat{H}(I, \varphi)$ is the excited Hamiltonian, and $\epsilon = 0$ corresponds to the unperturbed system.

By the definition of the Melnikov function on the homoclinic orbit $q_h(\tau) = (I_h(\tau), \varphi_h(\tau))$,

$$M(\tau_0) = \int_{-\infty}^{\infty} \left\{ \left(-\frac{\partial H}{\partial\varphi} \Big|_{\epsilon=0} \right) \left(\frac{\partial \bar{H}}{\partial I} \right) - \left(\frac{\partial H}{\partial I} \Big|_{\epsilon=0} \right) \left(-\frac{\partial \bar{H}}{\partial\varphi} \right) \right\} \sin \Omega\tau (q_h(\tau); \tau + \tau_0) d\tau$$

where the integral is evaluated on the unperturbed homoclinic orbit $q_h(\tau)$. Notice that on $q_h(\tau)$,

$$\begin{pmatrix} \frac{\partial H}{\partial\varphi} \Big|_{\epsilon=0} \\ \frac{\partial H}{\partial I} \Big|_{\epsilon=0} \end{pmatrix} = \begin{pmatrix} -\frac{dI}{d\tau} \\ \frac{d\varphi}{d\tau} \end{pmatrix}$$

and hence

$$\begin{aligned} M(\tau_0) &= \int_{-\infty}^{\infty} \left(-\frac{dI}{d\tau} \right) \left(\frac{\partial \bar{H}}{\partial I} \right) + \left(-\frac{d\varphi}{d\tau} \right) \left(\frac{\partial \bar{H}}{\partial \varphi} \right) \sin \Omega \tau (q_h(\tau); \tau + \tau_0) d\tau \\ &= - \int_{-\infty}^{\infty} \left\{ \frac{d\bar{H}}{d\tau} \right\} \sin \Omega \tau (q_h(\tau); \tau + \tau_0) d\tau \end{aligned} \quad (\text{A6.2})$$

From Eqn. (A6.2), the Melnikov function is related to the Fourier transform of the rate of the change in the unperturbed part of the excited Hamiltonian evaluated on the unperturbed homoclinic orbit.

Type 2 : internal excitation

Suppose that one of the canonical variables φ is perturbed sinusoidally in time around some value φ_0

$$\begin{pmatrix} \frac{dI}{d\tau} \\ \frac{d\varphi}{d\tau} \end{pmatrix} = \begin{pmatrix} -\frac{\partial}{\partial \varphi} \{H(I, \varphi - (\varphi_0 + \epsilon \sin \Omega \tau))\} \\ \frac{\partial}{\partial I} \{H(I, \varphi - (\varphi_0 + \epsilon \sin \Omega \tau))\} \end{pmatrix} \quad (\text{A6.3})$$

where $\epsilon = 0$ corresponds to the unperturbed system.

Since $\epsilon \sin \Omega \tau$ is $O(\epsilon)$, we expand Eqn. (A6.3) with respect to $\epsilon \sin \Omega \tau$

$$\begin{pmatrix} \frac{dI}{d\tau} \\ \frac{d\varphi}{d\tau} \end{pmatrix} = \begin{pmatrix} -\frac{\partial}{\partial \varphi} H(I, \varphi - \varphi_0) + \epsilon \sin \Omega \tau \frac{\partial^2}{\partial \varphi^2} H(I, \varphi - \varphi_0) + O(\epsilon^2) \\ \frac{\partial}{\partial I} H(I, \varphi - \varphi_0) - \epsilon \sin \Omega \tau \frac{\partial^2}{\partial \varphi \partial I} H(I, \varphi - \varphi_0) + O(\epsilon^2) \end{pmatrix}$$

where $O(\epsilon^2)$ terms are also periodic in time with period $T = \frac{2\pi}{\Omega}$. By definition of the Melnikov function on the homoclinic orbit $q_h(\tau) = (I_h(\tau), \varphi_h(\tau))$

$$\begin{aligned} M(\tau_0) &= \\ &\int_{-\infty}^{\infty} \left\{ \left(-\frac{\partial H}{\partial \varphi} \Big|_{\epsilon=0} \right) \left(-\frac{\partial^2 H}{\partial \varphi \partial I} \Big|_{\epsilon=0} \right) - \left(\frac{\partial H}{\partial I} \Big|_{\epsilon=0} \right) \left(\frac{\partial^2 H}{\partial \varphi^2} \Big|_{\epsilon=0} \right) \right\} \sin \Omega \tau (q_h(\tau); \tau + \tau_0) d\tau \end{aligned}$$

where the integral is evaluated on the unperturbed homoclinic orbit. Notice that the $O(\epsilon)$ terms evaluated on the unperturbed homoclinic orbit can be rewritten as follows.

$$\begin{pmatrix} \frac{\partial^2}{\partial \varphi^2} H(I, \varphi - \varphi_0) \\ \frac{\partial^2}{\partial I \partial \varphi} H(I, \varphi - \varphi_0) \end{pmatrix} = \begin{pmatrix} -\frac{\partial}{\partial \varphi} \left\{ \frac{dI}{d\tau} \right\} \Big|_{\epsilon=0} \\ \frac{\partial}{\partial I} \left\{ \frac{d\varphi}{d\tau} \right\} \Big|_{\epsilon=0} \end{pmatrix}$$

and hence the Melnikov function is

$$\begin{aligned} M(\tau_0) &= \int_{-\infty}^{\infty} \left[\left(\frac{dI}{d\tau} \right) \left\{ -\frac{\partial}{\partial I} \left(\frac{dI}{d\tau} \right) \right\} - \left(\frac{d\varphi}{d\tau} \right) \left\{ \frac{\partial}{\partial \varphi} \left(\frac{dI}{d\tau} \right) \right\} \right] \sin \Omega \tau (q_h(\tau); \tau + \tau_0) d\tau \\ &= \int_{-\infty}^{\infty} \left\{ \frac{d^2 I}{d\tau^2} \right\} \sin \Omega \tau (q_h(\tau); \tau + \tau_0) d\tau \end{aligned} \quad (A6.4)$$

From Eqn. (A6.4), the Melnikov function is related to the Fourier transform of the second derivative of the unperturbed canonical variable with respect to time evaluated on the unperturbed homoclinic orbit.

Following the same procedure, the Melnikov functions on RB $\frac{m}{n}$ can be written as follows.

Type 1 : external excitation

$$M^{\frac{m}{n}}(\tau_0) = \int_{-\frac{mT}{2}}^{\frac{mT}{2}} \left\{ \frac{d}{d\tau} \overline{H}(I, \varphi) \right\} \sin \Omega \tau (q^H(\tau); \tau + \tau_0) d\tau \quad (A6.5)$$

where the integral is evaluated on the corresponding unperturbed periodic orbit $q^H(\tau)$ with resonance relation $m\Omega^H = n\Omega$, where Ω^H is the natural frequency of the orbit. From Eqn. (A6.5), the Melnikov function is related to the Fourier coefficient of the unperturbed part of the excited Hamiltonian evaluated on the unperturbed invariant circle.

Type 2 : internal excitation

$$M^{\frac{m}{n}}(\tau_0) = \int_{-\frac{mT}{2}}^{\frac{mT}{2}} \left\{ \frac{d^2 I}{d\tau^2} \right\} \sin \Omega \tau (q^H(\tau); \tau + \tau_0) d\tau \quad (A6.6)$$

where the integral is evaluated on the unperturbed invariant circle with resonance relation $m\Omega^H = n\Omega$ where Ω^H is the natural frequency of the unperturbed orbit. From Eqn. (A6.6), the Melnikov function is related to the Fourier coefficient of the second derivative of the unperturbed canonical variable with respect to time evaluated on the unperturbed invariant circle.

Appendix 7

THE MODIFIED MELNIKOV FUNCTIONS

The purpose of this Appendix is to define and examine the dynamical consequences of the modified Melnikov functions on the homoclinic orbit and resonance band of order $\frac{m}{n}$ for a Hamiltonian system with time periodic perturbation whose equations of motion are written in complex form.

A7.1 Equations of motion

The system we study is written in a complex form as follows

$$\frac{dz^*}{d\tau} = h(z, z^*; c) = \frac{1}{2i} \frac{\partial}{\partial z} H(z, z^*; c) \quad (\text{A7.1})$$

where $z = x + iy, c \in \mathbb{R}^p$ ($p \geq 1$) is a parameter and $H(z, z^*; c)$ is the Hamiltonian function. We assume that $c \in \mathbb{R}^p$ has a small time periodic perturbation of $O(\epsilon)$ around c_0 with period $T = \frac{2\pi}{\Omega}$, i.e.,

$$\begin{aligned} c(\tau) &= c_0 + \epsilon c_1(\tau) \\ c_1(\tau) &= c_1\left(\tau + \frac{2\pi}{\Omega}\right) \end{aligned} \quad (\text{A7.2})$$

We can rewrite Eqn. (A7.1) in real variables $(\frac{dx}{d\tau}, \frac{dy}{d\tau})$ as follows

$$\begin{aligned} \frac{dx}{d\tau} &= h_1(x, y; c) = \text{Real } h(z, z^*; c) = \frac{\partial}{\partial y} H(z, z^*; c) \\ \frac{dy}{d\tau} &= h_2(x, y; c) = -\text{Im } h(z, z^*; c) = -\frac{\partial}{\partial x} H(z, z^*; c) \end{aligned}$$

Taylor expansion in c around c_0 yields

$$\begin{aligned} \frac{dx}{d\tau} &= f_1(x, y) + \epsilon g_1(x, y; \tau) + O(\epsilon^2) = h_1(x, y; c) \\ \frac{dy}{d\tau} &= f_2(x, y) + \epsilon g_2(x, y; \tau) + O(\epsilon^2) = h_2(x, y; c) \end{aligned} \quad (\text{A7.3})$$

where

$$\begin{aligned} \begin{pmatrix} f_1 \\ f_2 \end{pmatrix} &= \begin{pmatrix} h_1(x, y; c_0) \\ h_2(x, y; c_0) \end{pmatrix} \\ \begin{pmatrix} g_1 \\ g_2 \end{pmatrix} &= \begin{pmatrix} \frac{\partial}{\partial c} h_1(x, y; c) \cdot c_1(\tau)|_{c=c_0} \\ \frac{\partial}{\partial c} h_2(x, y; c) \cdot c_1(\tau)|_{c=c_0} \end{pmatrix} \end{aligned} \quad (A7.4)$$

Note that g_1 , g_2 and $O(\epsilon^2)$ terms are periodic with $T = \frac{2\pi}{\Omega}$.

A7.2 Modified Melnikov function $M_\epsilon(\tau_0)$ on the homoclinic orbit

We define a modified Melnikov function $M_\epsilon(\tau_0)$ as follows

$$M_\epsilon(\tau_0) = -\text{Im} \int_{-\infty}^{\infty} \left\{ \frac{dz_0^*}{d\tau} \right\} \left\{ \frac{dz}{d\tau} \right\} (z_h(\tau); \tau + \tau_0) d\tau \quad (A7.5)$$

where $\frac{dz_0^*}{d\tau} = f_1 - if_2$ is the unperturbed velocity in complex conjugate form, $\frac{dz}{d\tau} = h_1 + ih_2$ is the perturbed velocity, and the integral is evaluated on the unperturbed homoclinic orbit $z_h(\tau) = x_h(\tau) + iy_h(\tau)$. By substituting Eqn. (A7.3) into Eqn. (A7.5), we obtain

$$\begin{aligned} M_\epsilon(\tau_0) &= -\text{Im} \int_{-\infty}^{\infty} \{f_1 - if_2\} \{(f_1 + \epsilon g_1 + O(\epsilon^2)) + i(f_2 + \epsilon g_2 + O(\epsilon^2))\} \\ &\quad (x_h(\tau), y_h(\tau); \tau + \tau_0) d\tau \\ &= \epsilon \int_{-\infty}^{\infty} \{f_1 g_2 - f_2 g_1\} (x_h(\tau), y_h(\tau); \tau + \tau_0) d\tau + O(\epsilon^2) \\ &= \epsilon \int_{-\infty}^{\infty} \{f \wedge g\} (x_h(\tau), y_h(\tau); \tau + \tau_0) d\tau + O(\epsilon^2) \end{aligned}$$

Notice that the first term of the right hand side of the equation is related to the regular Melnikov function. Hence, the modified Melnikov function $M_\epsilon(\tau_0)$ and the regular Melnikov function $M(\tau_0)$ have the following relation.

$$M_\epsilon(\tau_0) = \epsilon M(\tau_0) + O(\epsilon^2) \quad (A7.6)$$

Note that the order of $M_\epsilon(\tau_0)$ is ϵ .

Now let us consider some dynamical consequences of the modified Melnikov function $M_\epsilon(\tau_0)$. Recall that the regular Melnikov function $M(\tau_0)$ is related to the signed distance $d(\tau_0, \epsilon)$ between unstable and stable invariant manifolds as follows.

$$d(\tau_0, \epsilon) = \frac{\epsilon M(\tau_0)}{\left\| \frac{d}{d\tau} z_0^*(z_h(-\tau_0)) \right\|} + O(\epsilon^2) \quad (\text{A7.7})$$

where $\|\cdot\|$ denotes the usual norm. From Eqns. (A7.6) and (A7.7), we obtain the relation of the modified Melnikov function $M_\epsilon(\tau_0)$ to the signed distance $d(\tau_0, \epsilon)$

$$d(\tau_0, \epsilon) = \frac{M_\epsilon(\tau_0)}{\left\| \frac{d}{d\tau} z_0^*(z_h(-\tau_0)) \right\|} + O(\epsilon^2) \quad (\text{A7.8})$$

It follows, by the Melnikov theorem, that simple zeroes of $M_\epsilon(\tau_0)$ (i.e., $M_\epsilon(\tau_0) = 0$, $\frac{\partial}{\partial \tau_0} M_\epsilon(\tau_0) \neq 0$) imply simple zeroes of $d(\tau_0, \epsilon)$, i.e., the transverse intersection of unstable and stable invariant manifolds (or existence of the homoclinic tangle structure).

Moreover, $M_\epsilon(\tau_0)$ is related to the area of a lobe (L) (see Chapter 3 for the definition). Recall that the area $\mu(L)$ is computed by the regular Melnikov function.

$$\mu(L) = \int_{\tau_1}^{\tau_2} \epsilon M(\tau_0) d\tau_0 + O(\epsilon^2)$$

where τ_1 and τ_2 are values of parametrization parameter τ_0 on the homoclinic orbit at two adjacent pip's corresponding to the lobe L . Substituting Eqn. (A7.8), we obtain $\mu(L)$ using the modified Melnikov function.

$$\mu(L) = \int_{\tau_1}^{\tau_2} M_\epsilon(\tau_0) d\tau_0 + O(\epsilon^2)$$

A7.3 Modified Melnikov function $M_{\epsilon^{\frac{m}{n}}}(\tau_0)$ on resonance band of order $\frac{m}{n}$

We define a modified Melnikov function $M_{\epsilon^{\frac{m}{n}}}(\tau_0)$ on resonance band of order $\frac{m}{n}$ as follows.

$$M_{\epsilon^{\frac{m}{n}}}(\tau_0) = -\text{Im} \int_{-\frac{mT}{2}}^{\frac{mT}{2}} \left\{ \frac{dz_0^*}{d\tau} \right\} \left\{ \frac{dz}{d\tau} \right\} (z^H(\tau); \tau + \tau_0) d\tau \quad (\text{A7.9})$$

where the integral is evaluated on the unperturbed periodic orbit, $z^H(\tau) = x^H(\tau) + iy^H(\tau)$, of natural frequency Ω^H with the resonance relation $m\Omega^H = n\Omega$. Following the same procedure as in the previous section, we can show that the modified Melnikov function $M_{\epsilon}^{\frac{m}{n}}(\tau_0)$ on resonance band of order $\frac{m}{n}$ is related to the regular Melnikov function $M^{\frac{m}{n}}(\tau_0)$ on resonance band of order $\frac{m}{n}$.

$$M_{\epsilon}^{\frac{m}{n}}(\tau_0) = \epsilon M^{\frac{m}{n}}(\tau_0) + O(\epsilon^2) \quad (A7.9)$$

where

$$M^{\frac{m}{n}}(\tau_0) = \int_{-\frac{mT}{2}}^{\frac{mT}{2}} \{f \wedge g\} (z^H(\tau); \tau + \tau_0) d\tau$$

It follows from Eqn. (A7.9) that simple zeroes of $M_{\epsilon}^{\frac{m}{n}}(\tau_0)$ (i.e., $M_{\epsilon}^{\frac{m}{n}}(\tau_0) = 0, \frac{\partial}{\partial \tau_0} M_{\epsilon}^{\frac{m}{n}}(\tau_0) \neq 0$) imply the existence of period m points of the resonance band of order $\frac{m}{n}$ by the Melnikov theorem.

REFERENCES

- Aref, H., "Integrable, Chaotic and Turbulent Vortex Motion in Two-dimensional Flows," *Ann. Rev. Fluid Mech.*, **15**, 1983, pp.345-389.
- Arnold, V.I. and Avez, A., **Ergodic Problems of Classical Mechanics**, 1968, W.A. Benjamin, New York.
- Batchelor, G.K., **An Introduction to Fluid Dynamics**, Cambridge University Press.
- Chow, and Hale, "Methods of Bifurcation theory," Springer: New York.
- Constantin, P. and Titi, E.S., "On the Revolution of Nearly Circular Vortex Patches," *Commun. Math. Phys.*, **119**, 1988, pp.177-198.
- Devaney, R. "An Introduction to Chaotic Dynamical Systems," Benjamin.
- Dritschel D., "Nonlinear Stability Bounds for Inviscid, Two-dimensional, parallel or Circular Flows with Monotonic Vorticity, and the Analogous Three-dimensional Quasi-geostrophic Flows," *J. Fluid Mech.*, Vol.191, 1988, pp.575-581.
- Dritschel D., "The Repeated Filamentation of Two-Dimensional Vorticity Interfaces," *J. Fluid Mech.*, Vol.194, 1988, pp.511-547.
- Fenichel, N., "persistence and smoothness of invariant manifolds for flows," *Ind. Univ. Math. J.*, 1971, 193-225
- Golubitsky, M. and Stewart, I., "Generic Bifurcation of Hamiltonian Systems with Symmetry," *Physica 24D*, 1987, pp.391-405.
- Greenspan, B.D. and Holmes, P.J., "Homoclinic Orbits, Subharmonics and Global Bifurcations in Forced Oscillations," in **Nonlinear Dynamics and Turbulence**, Pitman, pp.172-213.
- Greenspan, B.D. and Holmes, P.J., "Repeated Resonance and Homoclinic Bifurcation in a Periodically Forced Family of Oscillators," *SIAM Math. Anal.*, Vol.15, No.1, 1984, pp.69-97.
- Guckenheimer, J. and Holmes, P.J., **Nonlinear Oscillations, Dynamical Systems, and Bifurcations of Vector Fields**, Springer: New York.

Holmes, C. and Holmes, P.J., "Second Order Averaging and Bifurcations to Subharmonics in Duffing's Equation," *Journal of Sound and Vibration*, 78(2), pp.161-174.

Holmes, P.J. "The Dynamics of Repeated Impacts with a Sinusoidally Vibrating Table," *Journal of Sound and Vibration*, 1982, 84(2), pp.173-189.

Holmes, P.J. and Marseden, J.E., "Horseshoes in Perturbations of Hamiltonian Systems with Two degree of freedom," *Comm. Math. Phys.*, 1982, 82, pp.523-544.

Holmes, P.J., Marseden, J.E. and Scheurle, J., "Exponentially Small splitting of Separatrices," Preprint.

Jimenez, J., "On the Linear Stability of the Inviscid Kármán Vortex Sheet," *J. Fluid Mech.*, Vol.178, 1987, pp.177-194.

Kamm, J.R., "Shape and Stability of Two-Dimensional Uniform Vorticity Regions," 1987, Thesis, Caltech.

Keith, W.L. and Rand R.H., "Dynamics of a System Exhibiting the Global Bifurcation of a Limit Cycle at Infinity," *Int. J. Non-linear Mechanics*, 1985, Vol.20, No.4, pp.325-338.

Kirchoff, "Mechanik," 1876, Leipzig.

Kida, S., "Motion of an Elliptical Vortex in a Uniform Shear Flow," *Journal of the Physical Society of Japan*, Vol.50, No.10., 1981, pp.3517-3520.

Lamb, S.H., **Hydrodynamics**, Dover.

Lichtenberg and Liebermann, "Regular and Stochastic Motion," Springer, New York.

Liepmann, H.W. and Roshko, A., **Elements of Gas Dynamics**, Wiley.

McWilliams, J.C., "The Emergence of Isolated Coherent Vortices in Turbulent Flow," *J. Fluid Mech.*, Vol.140, 1984, pp.21-43

Melander, M.V., Overman E.A. II and Zabusky, N.J., "Computational Vortex Dynamics in Two and Three Dimensions," *Technical Report ICMA-86-93*, 1985.

Melander, M.V., Zabusky, N.J. and McWilliams, J.C., "Symmetric Vortex Merger in Two Dimensions: Causes and Conditions," *J. Fluid Mech.*, Vol.195, 1988, pp.303-340.

Melander, M.V., Zabusky, N.J. and McWilliams, J.C., "Axysymmetric Vortex Merger in Two-dimensions: Which Vortex is Victorious?," *Phys. Fluids*, **30**(9), 1987, pp.2610-2612.

Melander, M.V., McWilliams, J.C. and Zabusky, N.J., "Axysymmetrization and Vorticity-gradient Intensification of an Isolated Two-dimensional Vortex through Filamentation," *J. Fluid Mech.*, Vol.178, 1987, pp.137-159.

Melander, M.V., Zabusky, N.J. and Styczek, S., "A Moment Model for Vortex Interactions of the Two-Dimensional Euler Equations: Part I. Computation of a Hamiltonian elliptical Representation," 1987, Vol.167, pp.95-115.

Meyer, K. "Generic Bifurcation in Hamiltonian Systems," **Dynamical Systems: Warwick 1974A**, *Lecture Notes Math.*, vol. 468, Springer, pp.62-70.

Moore, D.W. and Saffman, P.G., "Structure of a Line Vortex in an Imposed Strain," in **Aircraft Wake Turbulence and Its Detection**, Plenum Press: New York, 1981, pp.339-354.

Moore, D.W. and Saffman, P.G., "The Density of Organized Vortices in a Turbulent Mixing Layer," *J. Fluid Mech.*, 1975, Vol.69, pp.465-473.

Moore, D.W. and Saffman, P.G., "The Instability of a Straight Vortex Filament in a Strain Field," *Proc. R. Soc. Lond.*, **346**, 1975, pp.413-425.

Neu, J.C., "The Dynamics of a Columnar Vortex in an Imposed Strain," *Phys. Fluids*, **27**(10), 1984, pp.2397-2402.

Polvani, L.M., Flierl, G.R. and Zabusky, N.J., "Filamentation of Unstable Vortex Structures Via Separatrix Crossing: A Quantitative Estimate Of Onset Time," to appear *Phys. Fluids Letters*

Rom-Kedar, V. and Wiggins, S.R., "Transport in Two Dimensional Maps,"

Rom-Kedar, V., Leonard A. and Wiggins, S.R., "An Analytical Study of Transport, Mixing and Chaos in an unsteady Vortical Flow," *J. Fluid Mech.*, Vol.000, 1989

Roshko, A., "Structure of Turbulent Shear Flows: A New Look," *AIAA Journal*, Vol.14. No.10, 1976, pp.1849-1857.

Saffman, P.G. and Schatzman, J.C., "Stability of a Vortex Street of Finite Vortices," *J. Fluid Mech.*, 1982, Vol.117, pp.171-185.

Saffman, P.G. and Baker, G.R., "Vortex Interactions," *Ann. Rev. Fluid Mech.*, 1979, 11: pp.85-112.

Saffman, P.G. and Szeto, R. "Structure of a Linear Array of Uniform Vortices," in *Studies in Applied Mathematics*, **65**, 1981, pp.223-248.

Shaw, S.W. and Wiggins, S.R., "Chaotic Dynamics of a Whirling Pendulum," *Physica D*, **31**, 1988, pp.190-211. "Transport in Two Dimensional Maps,"

Szeto, R. and Saffman, P.G., "Equilibrium Shapes of a Pair of a Uniform Vortices," *Phys. Fluids* **23**(12), 1980, pp.2339-2342.

Van Der Weele, J.P. Valkering, T.P., Capel, H.W. and Post, T., "The Birth of Twin Poincaré-Birkhoff Chains Near 1:3 Resonance," *Physica A*, 1988, **153**, pp.283-294.

Wan, Y.H. and Pulvirenti, M., "Nonlinear Stability of Circular Vortex Patches," *Comm. Math. Phys*, Vol.99, 1985, pp.435-450.

Wiggins, S.R., "Global Bifurcations and Chaos," 1988, Springer: New York.